

# **MULTIPASS OPTICAL CAVITY BASED TECHNIQUE FOR TRACE LEVEL DETECTION OF HEAVY WATER**

*By*  
**ANITA GUPTA**  
**ENGG01201504003**

**Bhabha Atomic Research Centre, Mumbai**

*A thesis submitted to the  
Board of Studies in Engineering Sciences*

*In partial fulfillment of requirements  
for the Degree of*

**DOCTOR OF PHILOSOPHY**

*of*

**HOMI BHABHA NATIONAL INSTITUTE**



**December, 2019**

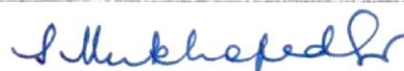


# Homi Bhabha National Institute

## Recommendations of the Viva Voce Committee

As members of the Viva Voce Committee, we certify that we have read the dissertation prepared by Anita Gupta entitled "Multipass optical cavity based technique for trace detection of heavy water" and recommend that it may be accepted as fulfilling the thesis requirement for the award of Degree of Doctor of Philosophy.

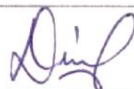
Chairman - Prof. Siddhartha Mukhopadhyay



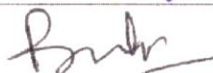
Guide / Convener - Prof. Anita Topkar



Co-guide - Prof. D. V. Udupa



Examiner - Prof. B. D. Gupta



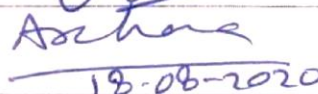
Member 1- Prof. S. R. Shimjith



Member 2- Prof. Namita Maiti



Member 3- Prof. Archana Sharma

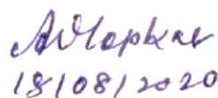


18-08-2020

Final approval and acceptance of this thesis is contingent upon the candidate's submission of the final copies of the thesis to HBNI.

I/We hereby certify that I/we have read this thesis prepared under my/our direction and recommend that it may be accepted as fulfilling the thesis requirement.

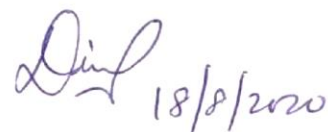
Date: 18/08/2020



18/08/2020

Place: Mumbai

Prof. Anita Topkar



18/8/2020

Prof. D. V. Udupa



## **STATEMENT BY AUTHOR**

This dissertation has been submitted in partial fulfilment of requirements for an advanced degree at Homi Bhabha National Institute (HBNI) and is deposited in the Library to be made available to borrowers under rules of the HBNI.

Brief quotations from this dissertation are allowable without special permission, provided that accurate acknowledgement of source is made. Requests for permission for extended quotation from or reproduction of this manuscript in whole or in part may be granted by the Competent Authority of HBNI when in his or her judgment the proposed use of the material is in the interests of scholarship. In all other instances, however, permission must be obtained from the author.

  
ANITA GUPTA



## DECLARATION

I, hereby declare that the investigation presented in the thesis has been carried out by me. The work is original and has not been submitted earlier as a whole or in part for a degree / diploma at this or any other Institution / University.



ANITA GUPTA



## List of Publications arising from the thesis

### Journal

#### Published

1. *"Laser based technique for monitoring heavy water leaks in nuclear reactors: performance validation with conventional techniques."* **A. Gupta**, S. Prasad, S. A. Prabhu, S. P. Somkuwar, K. P. Younus, S. Raghunathan, D. V. Udupa, M. N. Deo, and A. Topkar, Journal of Instrumentation 15, no. 03, **2020**, P03018; <https://doi.org/10.1088%2F1748-0221%2F15%2F03%2Fp03018>
2. *"Instrumentation and signal processing for the detection of heavy water using off axis–integrated cavity output spectroscopy technique"*. **A. Gupta**, P. J. Singh, D. Y. Gaikwad, D. V. Udupa, A. Topkar and N. K. Sahoo, Review of Scientific Instruments Vol. 89, **2018**, pp. 023110; <https://doi.org/10.1063/1.5019892>.
3. *"Astigmatic multipass cell with cylindrical lens"*; **A. Gupta**, D. V. Udupa, A. Topkar, N. K. Sahoo; Journal of Optics (Springer) Vol. 46, **2017**, No 3, pp. 324-330; <https://doi.org/10.1007/s12596-016-0376-8>

## Conferences

1. *Heavy water concentration measurement in air*"; **A. Gupta**, D. V. Udupa, A. Topkar and A. K. Mohanty; in Proc. of Advanced Sensors and Modelling Techniques for Nuclear Reactor Safety, Indian Institute of Technology (IIT) Bombay, Mumbai, 15-19 Dec, **2018**.
2. *Temperature sensitivity of D/H ratio determination using laser absorption spectroscopy*"; **A. Gupta**, D. V. Uduapa, A. Topkar and A. K. Mohanty; in Proc. of 7<sup>th</sup> International Conference on Perspectives in Vibrational Spectroscopy (ICOPVS-2018), at BARC, Mumbai, 25 -29 Nov, **2018**.
3. *Development of trace heavy water detector in water samples*"; **A. Gupta**, D. V. Udupa, A. Topkar and N. K. Sahoo; in Proc. of National Conference on "Optics, Photonics and Synchrotron Radiation for Technological Application (OPSR-2018)" at Raja Ramanna Centre for Advanced Technology, Indore, 29 Apr-2 May, **2018**.
4. *Experimental setup for off axis integrated cavity output spectroscopy*"; **A. Gupta**, P. J. Singh, D. V. Udupa, A. Topkar and N. K. Sahoo; in Proc. of 21<sup>st</sup> National Conference on Atomic & Molecular Physics, at Physical Research Laboratory, Ahmadabad, 3-6 Jan, **2017**.
5. *A modified Herriott multipass cell design with dense beam pass pattern for laser spectroscopy*"; **A. Gupta**, T. Jayasekharan, D. V. Udupa and N. K. Sahoo; in Proc. of National Laser Symposium-22, Manipal University, Manipal, 8-11 Jan, **2014**.



ANITA GUPTA

*Dedicated to My Mother*



## ACKNOWLEDGEMENTS

The work presented in this thesis would not have been possible without my close association with many people. I take this opportunity to extend my sincere gratitude and appreciation to all those who made this Ph.D. thesis possible. First and foremost, I would like to extend my sincere gratitude to my guide Dr. Anita Topkar for her dedicated help, advice, inspiration, encouragement and continuous support, throughout my Ph.D. My special words of thanks should also go to my co-guide Dr. Dinesh V. Udupa for his continuous support, guidance, cooperation, encouragement and for facilitating all the requirements, going out of his way. I would like to thank Dr. M. N. Deo, Head A&MPD for his guidance and encouragement. I would like to express my gratitude to Dr. B. N. Jagatap, former Head A&MPD, for his guidance and support. I would like to thank my doctoral committee for their valuable suggestions and inputs.

I am grateful to Mr. P. Sumanth (RRMD), Mr. Ranjit Sharma (HPD), Dr. Sushama Mishra, Mr. Gaikwad and Mr. Suresh Parbhu (HWD) with whom I have had the pleasure to work during this thesis. My heartfelt thanks to my senior colleagues, Dr. Pushpa M. Rao, Dr. Sunanda K., Dr. Susy Thomas, Dr. Aparna Shastri, Mr. Sampathkumar R. and Dr. P. S. Gill for their fruitful discussions' guidance and moral support. My special thanks Sanjay and Yogesh for their technical support. My appreciation is due to our divisional workshop K. Thnakarajan, V. A. Mhatre, R. S. Saroj, H. S. Koli, S. K. Kawade for their valuable support.

Nobody has been more important to me in the pursuit of this the sis than the members of my family. I would like to thank my parents; whose love and guidance are with me in whatever I pursue.



# CONTENTS

SUMMARY .....	xxi
LIST OF FIGURES .....	xxiii
LIST OF TABLES .....	xxxix
LIST OF ABBREVIATIONS .....	xxxiii
LIST OF SYMBOLS .....	xxxv
<b>CHAPTER 1 Introduction .....</b>	<b>1</b>
<b>CHAPTER 2 Literature Review and Introduction to Laser Absorption Spectroscopy for Trace Gas Detection .....</b>	<b>9</b>
2.1. Trace Gas Detection Techniques .....	9
2.2. LAS for Gas Detection.....	12
2.2.1. Energy Levels of Molecules.....	13
2.2.2. The LAS System.....	25
2.2.3. Concentration Determination from Laser Absorption Spectra .....	26
2.2.4. Performance Characteristics of LAS Detection System .....	29
2.3. LAS Techniques for High Sensitivity .....	32
2.3.1. Optical Multipass Cell .....	32

2.3.2.	Modulation Spectroscopy.....	34
2.3.3.	Cavity Enhanced Absorption Spectroscopy (CEAS) Techniques .....	35
2.4.	Introduction to High Sensitivity Techniques Using Optical Cavities .....	35
2.4.1.	Cavity Ring-Down Spectroscopy (CRDS) .....	35
2.4.2.	Cavity Attenuated Phase Shift (CAPS) Spectroscopy .....	36
2.4.3.	Integrated Cavity Output Spectroscopy (ICOS).....	37
2.4.4.	Other Cavity Enhanced Techniques.....	39
2.4.5.	Comparison of High Sensitivity LAS Techniques .....	39
2.5.	Summary.....	40
<b>CHAPTER 3 Novel Astigmatic Multipass Cell Design .....</b>		<b>43</b>
3.1.	Theoretical Description of Re-Entrant Condition .....	44
3.2.	Algorithm for Ray Tracing.....	46
3.3.	Simulation of Laser Beam Path in the Optical Cell.....	48
3.4.	Design Considerations .....	52
3.4.1.	Important Design Parameters: .....	52
3.4.2.	Case Studies .....	54
3.5.	Design of Optical Cavity for Trace HDO Detection System .....	56
3.6.	Summary.....	58

**CHAPTER 4 Design and Implementation of OA-ICOS System for Trace Heavy Water Detection 59**

4.1. Selection of Absorption Peaks..... 60

4.2. Laser System: Alignment of Laser and IR Source at 1390 nm..... 66

4.2.1. He-Ne Laser for Alignment..... 66

4.2.2. NIR Laser Source with Centre Wavelength at 1.39  $\mu\text{m}$  ( $7191\text{ cm}^{-1}$ )..... 66

4.3. Photodetectors for Sensing Cavity Output..... 69

4.4. Optical Cavity for OA-ICOS Experimental System..... 70

4.4.1. Specifications of High Reflectivity Mirrors for the Optical Cavity..... 70

4.4.2. Vacuum Cell Design for the Optical Cavity ..... 70

4.4.3. Alignment of the Optical Cavity..... 72

4.4.4. Piezoelectric Actuator for Cavity Length Dithering..... 75

4.5. Vacuum System..... 76

4.5.1. Introduction of Sample into the Vacuum Cell ..... 78

4.6. Temperature Sensor for Measuring the Temperature of the Sample ..... 79

4.7. Data Acquisition For OA-ICOS System..... 79

4.8. Summary..... 80

**CHAPTER 5 Signal Processing, Data Analysis, Characterization and Validation of the Developed System..... 83**

5.1.	OA-ICOS Signal: Theoretical Analysis.....	83
5.1.1.	Signal Enhancement by OA-ICOS Technique.....	83
5.1.2.	Limits on Sensitivity Enhancement by Optical Cavity.....	90
5.2.	Data Processing and Spectrum Fitting.....	93
5.3.	Factors Affecting Isotopic Ratio Measurement Using OA-ICOS Technique.....	97
5.3.1.	Effect of Isotopic Fractionation on Sampling.....	97
5.3.2.	Effect of Temperature on Estimated Concentration.....	100
5.3.3.	Measurement of Mirror Reflectivity.....	105
5.3.4.	Selection of Appropriate in Database.....	105
5.4.	Calibration with Standard Samples.....	108
5.5.	Sensitivity And Allan Variance of [HDO] Measurement.....	110
5.6.	Sensitivity Improvement by Wavelength Modulation.....	114
5.7.	Optimization of Fitting Process.....	115
5.8.	Performance Validation.....	120
5.8.1.	Correlation with Tritium Monitoring using LSC.....	121
5.8.2.	Correlation with IRMS.....	123
5.8.3.	Discussions.....	125
5.9.	Measurement Results of [HDO] in Air.....	126

5.9.1.	Measurements of HDO in Laboratory Air for Experimentally Simulated Leak Condition	129
5.10.	Summary.....	131
<b>CHAPTER 6</b>	<b>Conclusions and Future Scope.....</b>	<b>133</b>
APPENDIX I : AVAILABLE TECHNIQUES FOR HEAVY WATER LEAK MONITORING AND ISOTOPIC RATIO MEASUREMENTS..... 137		
I.1	Heavy Water Leak Monitoring.....	137
I.1.1	Dew Point Monitor.....	137
I.1.2	Beetle Detectors .....	138
I.1.3	Tritium Activity Monitors.....	138
I.1.4	O-19 Monitor .....	141
I.2	Isotope (D/H) Ratio Mass Spectrometry (IRMS) Technique .....	142
APPENDIX II: PROPERTIES OF OPTICAL CAVITY ..... 144		
II.1	Cavity Modes.....	144
II.1.1	Fundamental Mode.....	145
II.1.2	Higher Order Modes.....	147
II.2	Spectral Properties of a Cavity .....	148
II.3	Coupling Laser Beam to an Optical Cavity .....	151
II.3.2	Exciting Cavity Modes (Impedance Matching) .....	153

APPENDIX III: LEAST SQUARE CURVE FITTING .....	154
III.1 Linear Least Square Fitting .....	154
III.2 Non-Linear Least Square Fitting.....	155
III.2.1 Derivative Methods .....	155
III.2.2 Heuristic Methods.....	156
III.3 Software for Acquiring and Processing Data.....	157
APPENDIX IV: SPECTROSCOPIC DATA.....	159
IV.1 Spectroscopic Peak Parameters from HITRAN Database for the Peaks Considered in Fitting Algorithm [43, 44].....	159
IV.2 Spectroscopic Peak Parameters from GEISA-2015 Database for the Peaks Considered in Fitting Algorithm [46].....	160
References .....	161

## SUMMARY

Detection of heavy water leaks in PHWRs is of significant importance for economy and safety of the nuclear power plants & personnel. A continuous heavy water leak monitoring system is essential to avoid any major leak situation. Conventionally, the heavy water leak monitoring system is based on tritium activity measurement which suffers from interference by other radioactive species present in the reactor. Hence, there is a need for developing new techniques. The sensors based on optical method can meet the requirements of sensitivity, selectivity, compactness and real time monitoring at moderate costs. Among several optical techniques, laser absorption based Off-Axis Integrated Cavity Output Spectroscopy (OA-ICOS) technique is found to be the most suited for developing onsite compact portable equipment for monitoring heavy water leaks for PHWR. The thesis is focused on design, development, characterization & validation of the same.

In the present thesis, design of the heavy water monitoring system is based on HDO absorption line at  $7191.039\text{ cm}^{-1}$ . The system consists of diode laser, optical cavity, optical components, photodetector, oscilloscope and computer for data acquisition and signal processing. The system parameters are optimized to make it suitable for online measurement of [HDO] in air. A signal analysis technique has been developed to eliminate the effect of inherent gain non-linearity. Intricacies involved in the fitting of spectrum are presented. The effect of operating conditions such as temperature and pressure on the concentration measurement were studied and appropriate correction factors are incorporated in the signal analysis algorithm to improve the accuracy.

The characterization and validation of the developed system is performed by its calibration, stability and sensitivity analysis and comparison with the conventional techniques. Calibrated

value for mirror reflectivity was observed to be 99.92% by using standard samples. Calibration of detection system was performed using known [HDO] ranging from 20 to 2280 ppm (which covers the range of interest), while the analysis method was verified for linear calibration. An improvement in sensitivity from 10 ppm to 1.2 ppm for water samples was achieved by using cavity length dithering. Stability of the system was analysed by the method of Allan variance. The evaluated optimum integration time is 1280 sec for  $\pm 1.2$  ppm sensitivity and 160 sec for  $\pm 1.5$  ppm sensitivity. The long-term reproducibility of the system was evaluated to be  $\pm 3.2$  ppm ( $\pm 1$  %) in natural water sample.

The performance validation of the system was carried out using the samples collected from different locations in the DHRUVA reactor at BARC. These samples were also analysed by liquid scintillation counter (LSC) and Isotope Ratio Mass Spectrometer (IRMS) measurements. The measured [HDO] using the developed system shows an excellent correlation with the measurements obtained using these well-established techniques. The correlation coefficient of [HDO] measurement with tritium activity using LSC is 0.982 and that of D/H ratio measurement by IRMS is 0.971. The developed setup was also tested for detecting leakages of heavy water to the atmosphere by the measurement of [HDO] in air with an experimentally simulated leak condition in the laboratory. The minimum detectable [HDO] of 45 ppbv and the sensitivity of 113 ppbv of HDO fraction in air is achieved. Based on the above results, it can be concluded that the developed system is suitable for monitoring minor leakages of heavy water in PHWRs. The measurements performed by simulating a leak condition in the laboratory demonstrate the potential of the developed system for real time online monitoring of heavy water leak in PHWRs.

## LIST OF FIGURES

<b>Figure 2.1</b> Energy level diagram of a diatomic molecule along with the spectral ranges of molecular spectrum [38]. .....	15
<b>Figure 2.2</b> Structure of water molecule. ....	20
<b>Figure 2.3</b> Vibrational energy level diagram of water molecule (H <sub>2</sub> <sup>16</sup> O) [92], showing three vibrational modes and the transition wavelengths corresponding to fundamental and overtone transitions.....	21
<b>Figure 2.4</b> Stick plot of absorption peaks of water molecule and its isotopologues form IR to visible range [96].....	24
<b>Figure 2.5</b> The block digram showing the basic blocks of a LAS system. A basic LAS system consists of laser source with wavelength scanning, an absorption cell, detector and a signal processing system.....	25
<b>Figure 2.6</b> Top panel shows mode spectra with on-axis and off-axis alignment super-imposed with laser spectra and molecular transition. The lower panels illustrate the resultant signals from each alignment [73]. Reproduced from [73] with the permission of AIP Publishing. ....	38
<b>Figure 3.1</b> Optical layout of modified Herriott cell with cylindrical lens. M1, M2: High reflectivity spherical end mirrors; ‘d’: distance between M1 and M2; L: Cylindrical lens; ‘a’: distance between M2 and L. The laser beam enters through a hole in mirror M1, as shown in red. ....	43

**Figure 3.2** (a) Simulated 3D laser beam path for a spherical cell of length 10.9 cm with spherical mirrors of ROC =1 m along with focusing on photodiode (PD); (b) Laser beam spots on the front mirror (Red), rear mirror (Black) and on the photodetector (Green). ..... 49

**Figure 3.3** Plot of re-entrant number  $N_r$  and distance of exit point from hole centre verses position of lens. .... 50

**Figure 3.4** Overlap area versus  $N_r$  for: a) Centre input; b) Off-axis input..... 52

**Figure 3.5** Observed spot patterns of selected design examples with parameters as given in Table 3.2. (a)-(c) Shows the simulated spot pattern for centre input with  $N_r = 380, 380$  and  $470$  respectively; (d)-(f) Shows the simulated spot pattern for off-axis input with  $N_r = 380, 380$  and  $780$  respectively..... 57

**Figure 4.1** Photograph of the developed HDO detection system..... 60

**Figure 4.2** The block diagram and optical layout of the developed OA-ICOS system. The main of the system are OEM diode laser, optical cavity, optical componets, detectors, oscilloscope for data acquisition and computer for sihnal processing. .... 61

**Figure 4.3** Stick plot of  $\Psi$  band of water absorption peaks [96]..... 64

**Figure 4.4** Observed water spectrum around  $7183.97$  and  $7191.04 \text{ cm}^{-1}$  HDO absorption peaks with assigned wavenumbers for water sample..... 64

**Figure 4.5** Stick plot of absorption peaks used in the developed system [96]. .... 65

**Figure 4.6** Plot of laser output power with analog modulation voltage ( $V_{\text{analog}}$ ) for DM diode laser EP1390-5-DM-B01-FA. The zoomed region is shown in inset. .... 68

**Figure 4.7** The variation of laser wavelength for diode laser EP1390-5-DM-B01-FA with analog modulation voltage on laser current driver IP500. (a) Shows the spectrum recorded at two different pressures and the wavelengths (in nm) assigned to the absorptions peaks. (b) Plot of assigned wavelength versus the analog voltage with the linear and second order polynomial fit. 2<sup>nd</sup> polynomial shows better fit to assigned wavelength. .... 69

**Figure 4.8** 3D drawing of the designed assembly for the optical cavity. .... 71

**Figure 4.9** Steps to align the mirrors parallel. (a) Alignment of rear mirror, M2; (b) Alignment of front mirror, M1; and (c) Fine tuning of both mirrors and laser beam..... 73

**Figure 4.10** (a) Setup for the alignment of collimator to the axis of optical cavity, (b) Setup for coupling the IR laser to the optical cavity. .... 74

**Figure 4.11** (a) Optimization of coupling of laser power to the optical cavity; (b) The variation of transmitted intensity for two different alignments of input laser beam..... 75

**Figure 4.12** The observed transmission signal at different pressures of air containing moisture. 77

**Figure 4.13** Vacuum system used in development of OA-ICOS based trace heavy water detection system..... 78

**Figure 4.14** Screen shot of the typical display on the oscilloscope. The averaged waveforms for the cavity output, laser intensity and the laser scanning voltage are shown in yellow, green and magenta respectively. .... 80

**Figure 4.15** Screen-shot of the results displayed by the program used for signal processing. The acquired spectrum and its fitting results are shown on left side of the monitor. The measured

[HDO] along with the averaged time series plot of [HDO] are displayed on right side of the monitor. The averaged value of [HDO] and its standard deviation are displayed on top right.... 81

**Figure 5.1** Transmission signal for the optical cavity. The integrated cavity output is the sum of light intensity leaking on each reflection at rear mirror..... 84

**Figure 5.2** (a) Comparison of the cavity transmission signal with an imaginary cell with path length  $L_{\text{eff}}$  as function of normalised absorbance per pass. The dip in transmission intensity for an optical cavity is lower than that for an imaginary cell of length  $L_{\text{eff}}$ ; (b) This is also reflected in the normalised cavity gain function,  $G/G_0$ , as a function of normalized absorbance per pass. .... 87

**Figure 5.3** Plot showing the effect of cavity gain nonlinearity on the absorption signal. For low concentration, the cavity acts like a cell with effective path length  $L_{\text{eff}}$ . However, at higher concentrations, the absorption signal deviates from linear approximation. .... 89

**Figure 5.4** The plot of observed integrated absorbance (IA) for water absorption at  $7191.16 \text{ cm}^{-1}$  with pressure shows saturation effect due to cavity gain nonlinearity..... 89

**Figure 5.5** Figures show non-linear calibration curves for concentration measurement when the concentration is calculated using integrated absorbance as obtained by: (a) Welzel et al. [103]\*; (b) Yury et al. [104]†; (c) Maddaloni et al. [101]..... 90

**Figure 5.6** Plot of the typically recorded oscilloscope signals showing variation of recorded cavity output, laser intensity and laser scanning voltage ( $V_{\text{analog}}$ ) with time. Note: Time scale is reversed to show the spectrum from lower to higher wavenumber..... 94

**Figure 5.7** Typical observed absorption spectrum and curve fitting results (fitted Voigt profile for each peak, overall spectrum and the residual). The peak position and corresponding isotopologue

for each peak are indicated. The area under the HDO and H<sub>2</sub>O peak is shown by shaded region.  
 ..... 95

**Figure 5.8** Effect of isotopic fractionation on the observed value of [HDO] in the water sample, for successive injection of same sample after each cycle off evacuation and injection. .... 99

**Figure 5.9** Comparison of temperature dependent total internal partition function Q(T) values for (a) H<sub>2</sub><sup>16</sup>O and (b) HDO, obtained from HITRAN database and calculated values with coefficients given in Table 5.2..... 101

**Figure 5.10** Normalized variation of line-strengths for HDO peak at 7191.0139 cm<sup>-1</sup>, H<sub>2</sub>O peak at 7191.157 cm<sup>-1</sup>, and ratio of HDO to H<sub>2</sub>O line-strength, with temperature from 270 to 330 K (-3 to 57 °C). ..... 102

**Figure 5.11** Three sets of experimentally observed variation (with linear fit) in; (a) Area under H<sub>2</sub>O and HDO peaks shows the total water concentration inside the cell; (b) Ratio of area under the H<sub>2</sub>O and HDO peaks is in agreement with the change in line-strengths with temperature; and (c) [HDO] with temperature after correcting for temperature variation. AOTP: Area under the peak.  
 ..... 104

**Figure 5.12** Comparison of the [HDO] obtained using HITRAN and GEISA database. [HDO] is divide by 2 to get equivalent D/H. Since the slope of plot using HITRAN database is approximately 1, the HITRAN database was used in all subsequent measurements..... 107

**Figure 5.13** Correlation plot of concentration measurement, shows linearity in measurement for [HDO] ranging from 20 ppm to 2280 ppm. Twenty sets of measurements were taken for each

concentration. As individual measurement shows some deviations, averaging over these sets is required to obtain the accurate measured value. .... 109

**Figure 5.14** Time series plot of recorded [HDO]; (a) Without cavity length dithering; and (b) With cavity length dithering; (c) Allan variance plots for all three datasets..... 112

**Figure 5.15** Plot of standard deviation of measured [HDO] with integration time: with and without dithering. Plot shows considerable improvement in standard deviation when cavity length dithering is used, due to averaging out of cavity mode structure. .... 113

**Figure 5.16** The plot of [HDO], averaged for 64 consecutive measurements. The error bars show the standard deviation in measurements. (a) Data recorded without cavity length dithering; (b) Data recorded with cavity length dithering on six different days as shown in different colours. .... 113

**Figure 5.17** A comparison of OA-ICOS transmission signal and WM-OA-ICOS signal recorded using a lock-in-amplifier. The WM-OA-ICOS signal shows non- proportionality of positive excursion of the peaks to the absorption signal height and broadening of peaks..... 115

**Figure 5.18** Plot shows the acquired absorbance spectrum without any filtering and reduction of high frequency etalon fringes by using S-G filter. .... 117

**Figure 5.19** Comparison of three fitting methods. (a) FM2 with baseline correction shows better fit compared to FM1; The effect of FM2 w.r.t. FM1 can be seen in the region between the peaks as shown by ovals. (b) FM3 leads to reduction in standard deviation in residual; (c) FM3 shows higher standard deviation in estimated [HDO]. Hence it is concluded that FM2 is better curve fitting method..... 119

**Figure 5.20** A plot showing continuous measurement of [HDO] (100 samples) in samples labelled S1 to S7. The measured average value of [HDO] in ppm and standard deviation for each sample is shown in the figure..... 121

**Figure 5.21** Comparison of measured change in deuterium concentration  $\delta D$  using developed OA-ICOS system with normalised tritium concentration measured using LSC. .... 123

**Figure 5.22** Correlation between [HDO] by OA-ICOS and D/H ratio measurement by IRMS. 124

**Figure 5.23** Optimization of pressure for [HDO] measurement in air. Plot shows that maximum height to width ratio for air pressure around 110 mbar for HDO absorption peak. .... 126

**Figure 5.24** Measurement of [HDO] in laboratory air: (a) Observed spectrum without cavity length dithering shows significant noise due to fringes; (b) Shows reduction in fringes in the observed spectrum with cavity length dithering. .... 128

**Figure 5.25** Time series plot of (a) ratio [HDO]/[H<sub>2</sub>O] and [HDO] in air for determining their sensitivity in air. The standard deviation of plots shows the sensitivity of ratio [HDO]/[H<sub>2</sub>O] measurement is 6.17 ppm and that of [HDO] in air is 113 ppbv..... 128

**Figure 5.26** Measurement of [HDO] in artificially created leak like situation in the laboratory. (a) Variation of concentration of HDO and H<sub>2</sub>O in air; (b) Variation of HDO content with respect to water content..... 130

**Figure 5.27** The variation of [HDO] in air, for spillage of 50 to 600 micro litres of heavy water at distance of about 3 m from the absorption cell. .... 131

**Figure II.1** Plot of Laguerre-Gaussian modes of an optical cavity with spherical end mirrors having circular aperture [136]. .... 148

**Figure II.2** Transmission spectrum of optical cavity when a laser beam is coupled to its TEM<sub>00</sub> mode..... 150

**Figure II.3** Optical setup for mode matching..... 153

## LIST OF TABLES

<b>Table 2.1</b> Comparison of different types of gas detectors [2, 36, 37]. .....	11
<b>Table 2.2</b> Natural abundance of water isotopologues [43]. .....	23
<b>Table 2.3</b> List of absorption band of water spectrum and the vibrational transition involved. ...	24
<b>Table 2.4</b> Comparison of performance of various reported techniques for trace detection of water vapour. ....	40
<b>Table 3.1</b> ABCD matrix of common optical elements [88]. .....	47
<b>Table 3.2</b> Some of the design examples studied in this thesis. The spot patterns for selected designs marked by subscript a-f are shown in Figure 3.5 respectively. ....	55
<b>Table 4.1</b> Table showing HDO absorption peaks and their suitability for concentration determination. The peaks are listed in decreasing order of HDO line-strength. ....	65
<b>Table 4.2</b> The important specifications of DM diode laser, EP1390-5-DM-B01-FA (14 pin butterfly package). ....	67
<b>Table 4.3</b> Manufacturer's specification of high reflectivity mirrors used in the developed system. ....	71
<b>Table 5.1</b> D/H fractionation data values and equilibrium constant ratios between vapour and liquid phases in the temperature range from 0- 100°C in pure water system [116]. ....	98
<b>Table 5.2</b> The polynomial coefficients for equation (5.22) for a low temperature range of 70 to 500 K. ....	101

**Table 5.3** Effect of temperature on the measured parameters of absorption peaks..... 103

**Table 5.4** Comparison of line-strengths listed by HITRAN and GEISA databases..... 106

**Table 5.5** Comparison of standard deviation of residuals for all three fitting methods. .... 118

Table III.1 The incremental step for parameters optimization in the least square fitting algorithm.  
..... 156

## LIST OF ABBREVIATIONS

CW: Continuous Wave

CAPS: Cavity Attenuated Phase-shift Spectroscopy

CEAS: Cavity-Enhanced Absorption Spectroscopy

CRDS: Cavity Ring-Down Spectroscopy

FMS: Frequency Modulation Spectroscopy

FTIR: Fourier Transform InfraRed

GD: Gradient Descent method

GEISA: Gestion et Etude des Information Spectroscopiques Atmosphériques: Management and Study of Spectroscopic Information of the atmosphere

GN: Gauss-Newton Method

HITRAN: HIgh resolution TRANsmission

HWHM: Half Width at Half Maximum

IR: InfraRed

IRMS: Isotope Ratio Mass Spectrometry

LAS: Laser Absorption Spectroscopy

LIA: Lock-in-Amplifier

LMA: Levenberg–Marquardt algorithm

LSC: Liquid Scintillation Counter

MDA: Minimum Detectable Absorption

NEAS: Noise Equivalent Absorption Sensitivity

OGD: Optical Gas Detectors

OA-ICOS: Off-Axis Integrated Cavity Output Spectroscopy

PHWR: Pressurized Heavy Water Reactor

ppm: parts per million

ppb: parts per billion

ppt: parts per trillion

SNR: Signal to Noise ratio

TDLAS: Tunable Diode LAS

TEM: Transverse Electro-Magnetic mode

WMS: Wavelength Modulation Spectroscopy

## LIST OF SYMBOLS

Symbol	Meaning	Unit
A	Absorbance (for single pass)	-
$\alpha$	Absorption coefficient	$\text{cm}^{-1}$
$\alpha_{L-V}$	Fractionation ratio	-
c	Velocity of light (3e10)	cm/s
$\chi$	Anharmonicity constant	-
d	Cell length or optical path length	cm
E	Electric field of electromagnetic wave	V/m
$E_v$	Vibrational energy level	ev
$E_L$	Lower energy level of transition	ev
f	Focal length	cm
$f$	Beam intensity distribution function	-
F	Fineness of cavity	-
FSR	Free spectral range	Hz
$\phi$	Phase	rad
$\gamma_{L,G,V}$	Peak Shape function (Lorentzian, Gaussian, Voigt)	$1/\text{cm}^{-1}$
$\gamma_{\text{air}} (\gamma_{\text{self}})$	Half width air (self) broadening coefficient	$\text{cm}^{-1}$
$\Gamma_{L,G,V}$	Peakwidth (Lorentzian, Gaussian, Voigt)	Hz or $\text{cm}^{-1}$
h	Planks constant (6.626069e-27)	erg.s
IA	Integrated Absorbance	-
i,j,k	Indices or variables	-
I, $I_0$	Laser intensity	Watt/cm <sup>2</sup>
$JK_aK_c$	Rotational Quantum number of water molecule	-
$k_B$	Boltzmann constant (1.380649e-16)	erg·K <sup>-1</sup>
$\kappa$	Propagation constant	Rad/cm <sup>-1</sup>
$k$	Spring constant of oscillating molecule	

$L_{\text{eff}}$	Effective Optical path length	cm
$\lambda$	Wavelength	cm, nm
$M$	Molecular mass (1 amu = 1.660540e-24 g)	g
$\mu$	Reduced mass	g
$N_m$	Molecular density	Molecules/cm <sup>3</sup>
$N_r$	Number of passes for re-entrant condition	-
$N$	Number of atoms in molecule	-
$n$	Refractive index of material	-
$n$	Temperature coefficient for collisional broadening	-
$\nu$	Frequency	cm <sup>-1</sup> (spectroscopic representation) or Hz
$\Delta\nu$	Laser linewidth	cm <sup>-1</sup> or Hz
$\nu_c$	Centre wavenumber of transition	cm <sup>-1</sup> or Hz
$\Delta\nu_{\text{cavity}}$	FWHM of transmitted peak	cm <sup>-1</sup> or Hz
$\nu_{plq}$	Resonant frequencies of cavity modes	cm <sup>-1</sup> or Hz
$p, q, l, m, n$	Indices or variables	-
$P$	Pressure	mbar or Atm
$P_z$	Phase shift factor in Gaussian beam	rad
$q$	Volume mixing ratio	-
$q_z$	Gaussian beam parameter	-
$Q(T)$	Partition function	-
$\mathfrak{R}$	ROC of mirror	m
$\mathfrak{R}_z$	ROC of Gaussian beam as function of z	m
$R_m$	Mirror reflectivity	-
$S$	Line-strength	cm <sup>-1</sup> /(molecule.cm <sup>-2</sup> )
$\sigma_v$	Absorption cross section	cm <sup>2</sup>
$\sigma_{\text{Allen}}$	Allan variance	-
$\sigma_{\langle \text{variable} \rangle}$ $\sigma_{\langle \text{quantity} \rangle}$	Standard deviation	-

$t$	Time variable	s
$T, T_0$	Temperature (Reference temp)	K or °C
$T_m$	Mirror transmittance	-
$T_{cavity}$	Normalized cavity transmittance	-
$\tau_{RD}$	Cavity ring down time	s
$\tau_{int}$	Total integration time	s
$v = (v_1, v_2, v_3)$	Vibrational quantum number of water	-
$\omega$	Signal frequency	rad/s
$\bar{\omega}_{OSC}$	Oscillation frequency for molecule	cm <sup>-1</sup>
$\omega_z$	Gaussian beam radius at z	cm
$\omega_{z0}$	Gaussian beam waist at z=z <sub>0</sub>	cm
$\psi(x,y,z)$	Intensity distribution of laser beam	-
$r, x, y, z$	Dimensional co-ordinates	-



# CHAPTER 1

## INTRODUCTION

---

---

The presence of certain gases such as chlorine, hydrogen sulphide, hydrogen fluoride, nitrogen dioxide, sulphur dioxide, etc. in the environment is hazardous, even in trace amounts [1]. The detection of leaks of such hazardous gases is usually part of a safety system, and finds wide range of applications in areas like emission monitoring and control in industrial, agricultural, and animal facilities, environmental monitoring, biomedical and clinical diagnostics and several other applications. Gas sensors based on indirect method like electro-chemical process, semiconductors, thermal conductivity and catalytic reactions, etc., are of low cost and portable, but usually they suffer from low sensitivity, drift, and cross-sensitivity to other gases [2]. The instruments based on direct methods like gas chromatography [3] and mass spectrometry [4, 5] have high sensitivity (of order of ppm to ppt) and are highly selective, but are bulky and costly. They also require lengthy process of sample collection and preparation time. Hence, these methods are not suitable for real time portable applications having space constraint. The sensors based on optical method can provide sensitivity and selectivity comparable to direct method along with portability and real time monitoring at a moderate cost.

Trace gas detection plays an important role in process monitoring and the safeguarding of nuclear reactors; heavy water leak monitoring in Pressurised Heavy Water Reactors (PHWRs) is one of the concerns. In, PHWRs, the heavy water is used both as a neutron coolant and moderator. During

the normal operation, heavy water is contained in two separate closed loop systems, one for the moderator and other for the coolant [6]. Although nuclear reactors are designed and built with various safety features for containment, small amount of leakages of heavy water (coolant as well as moderator) still occur during normal reactor operation. These leakages are mainly through seals, valves, pipelines and steam generator, etc. Some heavy water leakages also occur during refuelling through feeders, end-fittings and the closure plug seals. This loss of heavy water due to leakages requires top-ups to compensate for the escapes. To minimise the loss of expensive heavy water from the reactor system, it is recovered, as much as economically feasible, by various processes. This recovered heavy water requires clean-up and up-grade to maintain its isotopic purity [7]; which adds to the cost of reactor operation [8].

In addition to the normal loss of heavy water, there could be some additional leakages because of degradation or malfunctioning of reactor system caused by corrosion or cracking in the reactor components. Such leak events may lead to reactor shutdown and/or release of the radioactivity to the environment. The radioactive materials are primarily produced due to the activation of the water molecules and dissolved gases by high neutron flux in the reactor. The induced activity in water generates the isotopes  $^{16}\text{N}$ ,  $^{17}\text{N}$ ,  $^{19}\text{O}$  and  $^3\text{H}$  [9]. The radio-nuclides,  $^{16}\text{N}$ ,  $^{17}\text{N}$  and  $^{19}\text{O}$  produce an intense gamma and beta radiation, limiting the access to the equipment in a running reactor. Due to short half-life, these three isotopes decay fast after a shutdown. However, the tritium isotope is a low energy  $\beta$  emitter with a half-life of 12.3 years. This long half-life leads to its concentration build-up in heavy water systems, which hardly decrease on shut down. Thus, a leak in heavy water system during normal operations and accidents can produce dangerous levels of tritium in the atmosphere. Although, the low energy beta particle from tritium is not an external radiation hazard,

it can cause internal damages if it enters the body through inhalation and skin [10]. Hence, the detection of heavy water leaks in PHWRs is of significant importance for the safety of people working there as well as for the power plant safety and economy. A continuous heavy water leak monitoring system is essential to avoid any major leak situation.

Traditionally, the heavy water leak monitoring system utilizes few types of sensors viz. beetle detectors, dew point sensors,  $^{19}\text{O}$  monitors, and tritium activity monitors [11-13] (Refer to Appendix I for more details). None of these methods meet all the requirements at the same time viz. high sensitivity, high selectivity, real time online measurement capability, portability, high reliability, and ease of use. For example, the beetle detectors detect the leaks due to shorting of electrodes as a result of accumulation of leaking coolant (or moderator) into the collection pots. However, they cannot detect minor leaks due to instantaneous evaporation of leaking coolant, on account of high temperature and pressure inside the pressure tubes. Use of dew point sensors is limited to monitoring of coolant leaking from the primary coolant channel to the annulus gas inside the reactor core. In addition, both these sensors cannot distinguish between  $\text{H}_2\text{O}$  and  $\text{D}_2\text{O}$  which may lead to triggering of false alarm [14]. Similarly, the online  $^{19}\text{O}$  monitors are used for detecting leakage of primary coolant to secondary coolant in heat exchangers by monitoring the 1.357 MeV  $\gamma$ -photons of  $^{19}\text{O}$  [15]. The sensitivity of these detectors is limited due to the interference caused by other radio nuclides such as  $^{41}\text{Ar}$ ,  $^{85}\text{Kr}$ ,  $^{222}\text{Rn}$  or  $^{133}\text{Xe}$  emitting  $\gamma$ -photons (energy ranging from 81 to 1294 keV) and  $\beta$ -particles (energy ranging from 346 to 1197 keV) in the reactor environment. Mostly, monitoring of heavy water leak to the atmosphere is done by tritium beta activity monitoring using a liquid scintillation counter (LSC) and ionization chambers [16]. For LSC the liquid samples are collected manually at various locations and their activity is measured off-line.

For the measurement of tritium in air, either bubblers or cold fingers are used to collect the moisture in the air. This involves a delay due to the time required for sample collection, preparation and counting. Thus, it is limited to measurements of only a few samples per day. The ionizations chambers are not sensitive enough to monitor minor leaks. In addition, tritium activity monitoring suffers from interference due to other radioactive nuclides present in nuclear reactor. Hence, there is a need for developing new techniques for the detection of heavy water leaks in PHWRs. It is desirable to a use technique which are based on entirely distinct processes.

The gas sensors, based on optical method can provide both sensitivity and selectivity, and could also meet the requirements of compactness and real time monitoring at moderate costs. The advent of compact tunable diode lasers in near IR range has revolutionised the development of portable gas detectors [17-20]. Hence, LAS technique for the detection HDO is selected in the present thesis. A major merit of LAS based system for coolant leak detection is the selectivity and negligible interference from the other radioactive species inherently present in the reactor environment. In addition, the laser-based technique is suitable for in situ online real time measurement of the HDO concentration without a need for any lengthy sample preparation. Among several LAS techniques, Off-Axis integrated cavity output spectroscopy (OA-ICOS) technique is found to be most suited for developing onsite compact portable equipment for trace level gas detection due to its high sensitivity and stability [21, 22].

The feasibility of applying OA-ICOS technique for heavy water leak monitoring was demonstrated internationally only by one research group [23, 24]. However, there were several inadequacies in their work. A major inadequacy in their technique was that, they have monitored the height of absorption signal as proportional to the HDO concentration while no attempt was made by them

for signal analysis and actual quantification of HDO concentration (denoted by [HDO]). The performance validation by comparison with respect to conventional techniques was not performed by them. Also, issues related to the variation of the sensitivity with parameters such as temperature, operating pressure etc., were not addressed. In this thesis, a methodology of signal processing is developed for quantification of [HDO] incorporating all the major factors affecting the absorption signal. These effects include presence of strong H<sub>2</sub>O absorption peak in the spectra, pressure and temperature of the sample inside the cavity, the cavity gain non-linearity and isotopic fractionation. The research involved in arriving at the correction factors for all these effects and corrections incorporated in a signal processing algorithm are part of this thesis work.

Although OA-ICOS based technique has potential for heavy water leak monitoring, use of this technique for heavy water leak detection is still not well established. Therefore, the thesis is focused to develop and validate a heavy water leak monitoring system for PHWR applications. The system described in this thesis overcomes shortcomings of methods described earlier. In this thesis, the heavy water leaks are monitored by measuring [HDO] in the liquid or air samples, since the leaked heavy water (D<sub>2</sub>O) is spontaneously converted to HDO due to the reaction with moisture (H<sub>2</sub>O) in the atmosphere. The objectives of this thesis are:

- (a) Design and demonstration of OA-ICOS based experimental setup for trace heavy water detection. This also includes design, simulation study, and characterization of the optical cavity.
- (b) Study of major factors affecting concentration measurement and designing a data processing and analysis algorithm incorporating appropriate correction factors.

- (c) Characterization and validation of the developed system by its calibration, stability and sensitivity analysis and comparison with the conventional techniques like LSC and Isotope Ratio Mass Spectrometer (IRMS).

The research carried out under the thesis is presented in six Chapters. The outline of the thesis is given below:

Chapter 2 presents a literature review based on about 85 references describing various trace gas detection techniques, laser absorption spectroscopy (LAS) and sensitivity improvements techniques in LAS. The potential of OA-ICOS technique for developing the required heavy water monitoring system is also discussed.

In Chapter 3, design and simulation study of a new type of astigmatic optical cell is presented. The cell consists of two spherical end mirrors with a cylindrical lens placed between them. This configuration allows control of astigmatism by varying the position of cylindrical lens, allowing a large number of alignment solutions. The simulation study performed and design solutions are presented in this chapter.

In Chapter 4, presents the design details of developed heavy water leak monitoring system based OA-ICOS technique. In this chapter, the criteria of selecting various components such as optical cavity and its mirrors, lasers, detectors, vacuum components, control and data acquisition system and their important characteristics are discussed.

In Chapter 5, the detailed theory of OA-ICOS system is initially presented followed by which the method of signal analysis and curve fitting are discussed. The factors affecting the concentration measurement, such as isotopic fractionation, temperature, mirror reflectivity and cavity gain

nonlinearity are and their correction factors are also discussed in this chapter. The characterization of the system, i.e., its calibration, sensitivity and stability are presented. The system validation results with LSC and IRMS are shown. The feasibility study of heavy water leak monitoring in air is also part of this chapter.

In Chapter 6, the conclusions obtained from the studies performed for the development of trace heavy water detection system under this thesis are summarized and future directions are mentioned.



## CHAPTER 2

# LITERATURE REVIEW AND INTRODUCTION TO LASER ABSORPTION SPECTROSCOPY FOR TRACE GAS DETECTION

---

Trace detection of hazardous gases is critical to ensure safety at the workplace, and for a healthy environment. There are several effective methods for detection of trace gases some of which are presented in this chapter. The LAS based detectors are extremely effective for *in-situ* real time monitoring of trace gases. Very high sensitivity (up to few ppb) is usually achievable using advanced LAS techniques, such as Cavity Enhanced Absorption Spectroscopy (CEAS). This chapter provides an introduction to various LAS techniques.

### 2.1. TRACE GAS DETECTION TECHNIQUES

The trace gas detection techniques can be divided in two broad classes: industrial gas detectors and high end analytical techniques. The industrial gas detectors include electrochemical sensors (based on electrical signal produced by chemical reaction with semiconductors, polymers or carbon nanotubes films), chemiluminescence sensor (based on light produced as a result of chemical reaction) and photo ionization detectors (based on ionization by UV light) [25, 26]. However, these detectors have relatively low sensitivity and selectivity for their usage in trace gas detection. The high-end analytical techniques which are suitable for trace gas detection include the following:

(a) Optical Gas Detectors (OGD):

The interaction of electromagnetic radiation with molecules has led to the development of many systems based on optical techniques for trace gas detection. The OGD's are based on absorption or emission spectrometry of molecules, particularly in infrared region and their main advantage is scalability, higher sensitivity and stability, high selectivity and fast response time. The OGDs are available with wide range of sensitivities ranging from few % to ppb level as required for low end industrial gas detectors to high end research work and environmental studies. The sensitivity of such detectors depends on the technique used and the complexities involved. Some of the available OGDs are photo spectrometers, Non-Dispersive IR spectrometer (NDIR) [27], laser absorption spectroscopy (LAS) [28], Differential Optical Absorption Spectroscopy (DOAS) [29], Raman Light Detection and Ranging (LIDAR) [30], Fourier Transform IR Spectroscopy (FTIR) [31], Laser Induced Fluorescence (LIF) and Laser Breakdown Spectroscopy (LIBS) [32, 33].

(b) Photoacoustic Spectroscopic (PAS) Gas Detectors:

PAS gas detectors are based on photo-acoustic effect, i.e., generation of pressure or sound wave due to thermal expansion caused by the absorption of light by the gases inside a photo-acoustic cell [34]. These detectors can achieve sensitivity up to ppb and ppt levels using advanced techniques.

(c) Mass Spectrometers (MS):

Mass spectrometers operates by ionizing the sample of interest and separating the resulting stream of ions according to their mass-to-charge ratio ( $m/z$ ) [5]. Commonly used mass spectrometers are magnetic sector type (Neir type), single quadrupoles, ion traps, and time-of-flight mass

spectrometers. Isotope Ratio Mass spectrometry (IRMS) is a specialized Neir type mass spectrometer optimized for precise measurement of isotope abundances in the sample [4].

**Table 2.1** Comparison of different types of gas detectors [2, 36, 37].

<b>Type</b>	<b>Advantages</b>	<b>Disadvantages</b>	<b>Sensitivity</b>
<b>Industrial Gas Detector (Electrochemical, chemi-luminescence and photo-ionization)</b>	Low cost, portable and easy to use.	Low sensitivity and selectivity and response dependent on environmental factors.	Few % to few ppm
<b>Optical Gas Detectors</b>	High sensitivity, high stability, high selectivity and fast response time. Can be designed for industrial as well as high end laboratory applications.	Medium cost, medium size.	Few % to ppb
<b>Photoacoustic Detectors</b>	High sensitivity, high linearity, non-destructive, noncontact, applicable to macro- and microsamples, insensitive to surface Morphology.	High cost, sensitive to ambient conditions.	Few ppm to few ppb
<b>Mass Spectrometers</b>	High sensitivity and selectivity.	High cost, bulky size, suitable only for laboratory application. Destructive technique.	Few ppm to ppt
<b>Gas Chromatographs</b>	Excellent separation, high sensitivity and selectivity.	High cost, bulky size, suitable only for laboratory application, can analyse compounds that can be vaporized without decomposition.	Few ppb to ppt

(d) Gas Chromatography (GC):

Gas chromatography is a highly accurate method of gas sensing [3]. The sample solution is injected into the GC inlet where it is vaporized and swept onto a chromatographic column by the carrier gas (usually helium). The compounds of interest in the sample flowing through the column are separated by virtue of their relative interaction with the coating of the column (stationary phase) and the carrier gas (mobile phase). GC/IRMS is a method where a sample mixture is first separated by gas chromatography before being characterized according to mass-to-charge ratio and relative abundance of isotopes [35]. It is a highly specialized instrumental technique used to ascertain the relative ratio of light stable isotopes of carbon ( $^{13}\text{C}/^{12}\text{C}$ ), hydrogen ( $^2\text{H}/^1\text{H}$ ), nitrogen ( $^{15}\text{N}/^{14}\text{N}$ ) or oxygen ( $^{18}\text{O}/^{16}\text{O}$ ) in individual compounds separated from complex mixtures of the components.

The comparison of different types of gas detectors is presented in Table 2.1. Based on the literature survey, the LAS based technique was further explored for the development of the required HDO detector for heavy water leak monitoring. The major attraction of LAS technique are high sensitivity, high stability, high selectivity and fast response time. The literature survey and brief introduction to LAS technique is presented in subsequent sections.

## 2.2. LAS FOR GAS DETECTION

The desired characteristics of an ideal gas sensor include high sensitivity, selectivity, multicomponent detection capability, room-temperature operation, large dynamic range, automatic operation, small size, high reliability, ease of use, and cost-effectiveness. With the recent technical advances in the field, the LAS techniques are not far from meeting these requirements. These advances include availability of tunable diode lasers, both near-infrared (NIR) and mid-

infrared (MIR); novel nonlinear materials for optical frequency conversion; optical fibre and semiconductor amplifiers; low-noise, room-temperature detectors; and advanced data acquisition and signal processing techniques. Many detectors based on tunable diode LAS (TDLAS) have been reported for environmental and industrial gas monitoring [20]. These detectors are capable of real time, ultra-sensitive detection of trace gas molecular species at concentrations varying from the few percent level down to parts per trillion (ppt). The principle of LAS is introduced as below. The absorption spectroscopy is based on absorption of electromagnetic (EM) radiation in the UV, visible, infrared regions by molecules interacting with such radiation. The absorption of radiation at a specific wavelength occurs when the molecules undergo transitions from lower to higher electronic, vibrational, and rotational energy levels which are described in next section.

### 2.2.1. Energy Levels of Molecules

The energy levels of a freely moving molecule are derived from the time dependent Schrödinger's equation; a fundamental equation in quantum mechanics [38]. In the simplest form the total energy of a molecule  $E_{\text{Total}}$  (in Joules), can be written as sum of three energies i.e. its electronic energy,  $E_e$ , vibrational energy of constituent atoms,  $E_{\text{vib}}$ , and energy of rotation about its principle axes,  $E_{\text{rot}}$ :

$$E_{\text{Total}} = E_e(\Lambda) + E_{\text{vib}}(\nu) + E_{\text{rot}}(J) \quad (2.1)$$

All three energies are quantized, and are identified by their respective quantum numbers  $\Lambda$ ,  $\nu$  and  $J$ . The absorption of a photon of frequency,  $\nu$ , by a molecule involves transition from one quantum state ( $\Lambda, \nu, J$ ) to another quantum state ( $\Lambda', \nu', J'$ ).

$$\nu = \frac{E_{\text{Total}}(\Lambda, \nu, J) - E_{\text{Total}}(\Lambda', \nu', J')}{h} \quad (2.2)$$

where  $h$  is the Planck's constant. During the transition, the change in quantum numbers is in accordance with the allowed quantum mechanical selection rules. Figure 2.1 shows a generalized energy level diagram of a diatomic molecule along with the various possible types of molecular transitions; that are rotational, vibrational and electronic transitions. Since each molecule is uniquely characterized by a set of energy levels, the transitions between these levels result in highly specific spectroscopic features.

#### 2.2.1.1. Vibrational Energy Levels

The vibrational transitions are most commonly utilized in trace gas detection and isotopic ratio measurements. A vibrational spectrum involves transitions between two vibrational states belonging to the same electronic level (i.e.,  $\Lambda = \Lambda'$ ). The number of vibrational modes of the molecule depends both on its shape and number of atoms,  $N$ , in the molecules. A linear molecule has  $3N - 5$  fundamental vibrations, while a nonlinear molecule has only  $3N - 6$  modes. For a diatomic molecule (as shown in Section 2.2.1), only single vibration mode is possible, that is stretching of the bond. The vibrations of a diatomic molecule are approximated by an anharmonic oscillator. The quantized energy levels,  $\epsilon_{\text{vib}} (\text{cm}^{-1})$ , of a diatomic vibrating molecule are given by following equation:

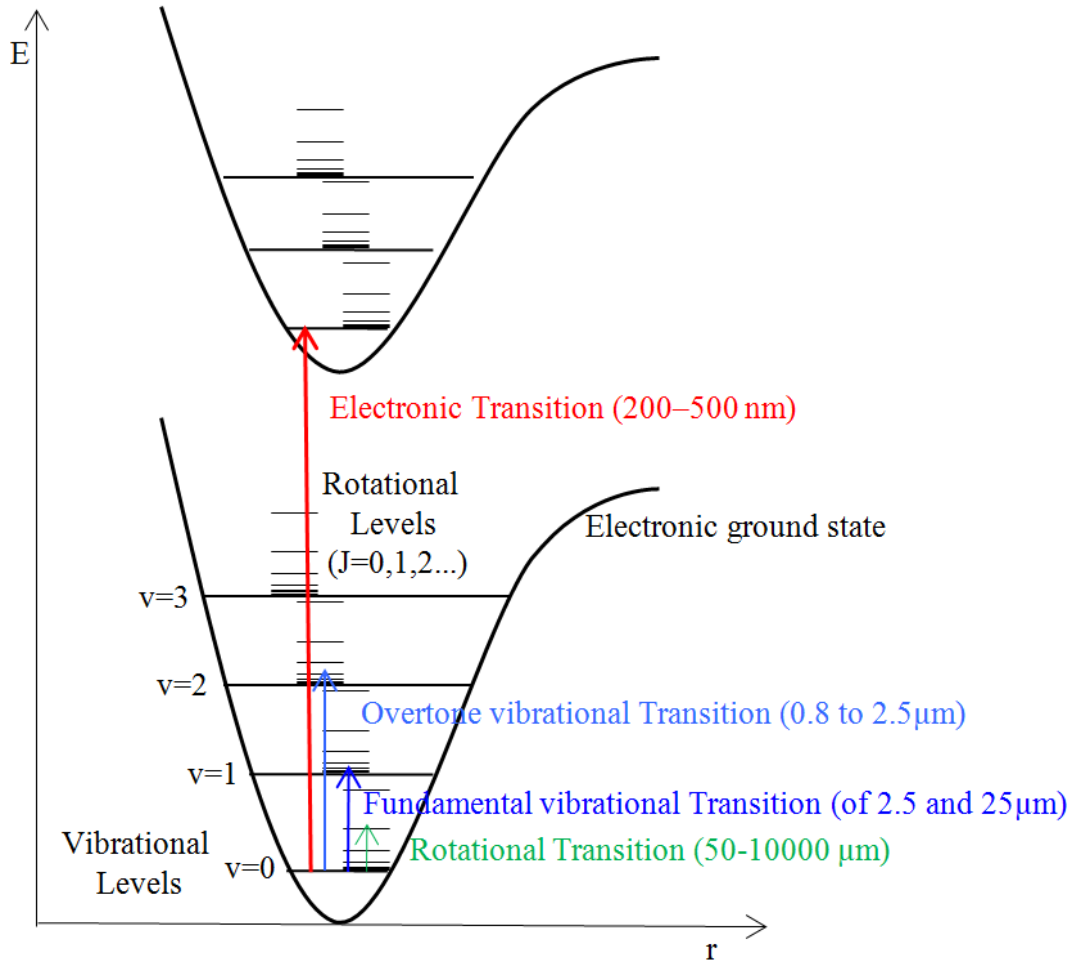


**Figure 2.1** Energy level diagram of a diatomic molecule along with the spectral ranges of molecular spectrum [38].

$$\begin{aligned} \epsilon_{\text{vib}} = \frac{E_{\text{vib}}}{hc} = \bar{\omega}_{\text{osc}} \left( v + \frac{1}{2} \right) - \chi_e \bar{\omega}_{\text{osc}} \left( v + \frac{1}{2} \right)^2 \\ + y_e \bar{\omega}_{\text{osc}} \left( v + \frac{1}{2} \right)^3 + \dots \end{aligned} \quad (2.3)$$

where  $v$  represents the vibrational quantum number ( $v=0, 1, 2, \dots$ ),  $\chi_e$  and  $y_e$  are the anharmonicity constants and  $\bar{\omega}_{\text{osc}}$  is the vibrational constant in  $\text{cm}^{-1}$ , which is defined as:

$$\bar{\omega}_{\text{osc}} = \frac{1}{2\pi c} \sqrt{\frac{k}{\mu}} \quad (2.4)$$

where  $k$  is the spring constant which depends on quantum mechanical properties of the molecule,  $\mu$  is the reduced mass and  $c$  is speed of light. Unlike the harmonic oscillator, the energy levels of an anharmonic oscillator are not equally spaced and their spacing decreases with increasing vibrational quantum number  $v$ . This shift depends on anharmonicity constants,  $\chi_e$ ,  $y_e$  etc. in accordance with second term in the equation (2.3)., the magnitude of these constants rapidly diminish with increasing order.

Vibrations of polyatomic molecules are described by normal modes, characterized by a different type of motions including asymmetric stretching, symmetric stretching, wagging, twisting, scissoring, and rocking. Under the harmonic approximation the total vibrational energy of the molecule is given by:

$$\epsilon_{\text{vib}} = \sum_{i=1}^{N_{\text{modes}}} \omega_{\text{osc},i} \left( v_i + \frac{d_i}{2} \right) \quad (2.5)$$

where  $d_i$  is its degeneracy. The total vibrational energy of the molecule including anharmonic terms is given as:

$$\epsilon_{\text{vib}} = \sum_{i=1}^{N_{\text{modes}}} \bar{\omega}_{\text{osc},i} \left( v_i + \frac{d_i}{2} \right) + \sum_{i \leq j}^{N_{\text{modes}}} \chi_{ij} \left( v_i + \frac{d_i}{2} \right) \left( v_j + \frac{d_j}{2} \right) + \dots \quad (2.6)$$

where,  $N_{\text{modes}}$  is number of fundamental vibrational modes,  $\chi_{ij}$  is the anharmonicity constant. The corresponding vibrational wavenumbers are given by a relation of the form:

$$\bar{\omega}_{\text{osc},i} = \frac{1}{2\pi c} \sqrt{\frac{k}{\mu_i}} \quad (2.7)$$

where,  $\mu_i$  is the effective mass for a given normal mode  $i$ .

### 2.2.1.2. Rotational Energy Levels

The rotational motion of a molecule is also quantized, and is represented by rotational quantum number  $J$ . The rotational energy levels for rigid diatomic molecules are given as:

$$E_{\text{rot}} = \frac{1}{2} I \omega^2 = \frac{L^2}{2I} \quad (2.8)$$

$$\varepsilon_J = \frac{E_{\text{rot}}}{hc} = BJ(J+1)$$

where,  $\varepsilon_J$  is in  $\text{cm}^{-1}$  and  $B(\text{cm}^{-1}) = \frac{h}{8\pi^2 Ic}$  is the rotational constant of the molecule,  $I$  is moment of inertia,  $I = \mu r^2$ ;  $L = I\omega$ ;  $\mu$  is reduced mass and  $r$  is bond length. For non-rigid molecule under simple harmonic approximation, the expression changes to:

$$\varepsilon_J = BJ(J+1) - DJ^2(J+1)^2 \quad (2.9)$$

where  $D = \frac{h^3}{32\pi^4 I^2 R^2 kc}$  is centrifugal distortion coefficient in  $\text{cm}^{-1}$ . When the anharmonic terms are included the expression for energy levels becomes:

$$\varepsilon_J = BJ(J+1) - DJ^2(J+1)^2 + HJ^3(J+1)^3 + KJ^4(J+1)^4 + \dots \quad (2.10)$$

$H$ ,  $K$ , etc are small constants dependent upon geometry of the molecules, and negligible compared with  $D$ .

A polyatomic molecule possess rotation around more than one axis. The energy of rotation of a polyatomic molecule is defined by the quantized rotational angular momentum along the three principal axes corresponding to the principal moments of inertia. The rotational kinetic energy of a rigid polyatomic molecule is represented by:

$$E_{\text{rot}} = \frac{1}{2} I \omega^2 = \frac{J_a^2}{2I_A} + \frac{J_b^2}{2I_B} + \frac{J_c^2}{2I_C} \quad (2.11)$$

where, A, B and C are mutually orthogonal along the x, y and z directions. Conventionally,  $I_A \leq I_B \leq I_C$ . The rotational energy levels of the molecules can be represented in terms of the quantum numbers J, M and K depending on symmetry of the molecule. Like rigid diatomic molecules, the energy levels of ployatomic molecules are also affected by the centrifugal distortion and anharmonic term. The energy difference between the adjacent rotational levels is 2 to 3 orders of magnitude lower than the difference between adjacent vibrational levels. Thus, there is a stack of many rotational levels associated with each vibrational level. The separation between these rotational lines in a vibration band depends on the rotational constant of the molecule.

### 2.2.1.3. Ro-Vibrational Transitions

As shown in the Figure 2.1, the vibrational transitions occur in the infrared region of electromagnetic spectrum. Each vibrational transition when viewed under sufficient resolution is seen to consist of a large number of closely spaced rotational lines resulting in the ‘band spectrum’. The resulting spectrum is known as ro-vibrational spectrum. The selection rules for vibrational quantum number for anharmonic potential are:

$$\Delta v = \pm 1, \pm 2, \pm 3, \dots \quad (2.12)$$

The  $\Delta v = \pm 1$ , represents the fundamental transition, while other values represent overtone. The overtone transitions are allowed due to the presence of anharmonicity, which leads to coupling between the vibrational levels. In case of poly atomic molecules, anharmonicity also couples various vibrational mode, which results in formation of combinational and difference bands. The combinational band is formed when two or more vibrational quanta are simultaneously excited. The selection rules for rotational quantum number depends on the type of molecules [38].

The transitions between molecular rotational-vibrational states occur in the infrared ‘fingerprint’ region of the electromagnetic spectrum, approximately between the wavelengths of 2.5 and 25  $\mu\text{m}$ . The overtone and combination vibrational bands lie typically in the 0.8 to 2.5  $\mu\text{m}$  spectral region, with peak intensity significantly lower as compared to those for fundamental vibration bands. The transitions between electronic states of molecules lie in the ultraviolet and visible spectral region, 200–500 nm. A high-resolution spectrum can be obtained by scanning the emission wavelength of a narrow linewidth laser across an individual gas absorption peak. A typical absorption spectrum consists of several discrete absorption peaks forming patterns unique to each molecule. It follows that the infra-red absorption features allow both the identification and quantification of the molecular species, such as atmospheric trace gases.

#### 2.2.1.4. Water Absorption Spectral Features

The spectroscopic features of each molecule are unique and should be known precisely for the development of any spectroscopic detector. With the aim of developing HDO detector, the spectral properties of water are discussed below.

##### 2.2.1.4.1. Vibrational Energy Levels of Water

Water is a tri-atomic nonlinear molecule as shown in Figure 2.2 and has three fundamental modes of vibration. These modes are symmetric stretching (mode I), bending (mode II) and asymmetric stretching (mode III), denoted by quantum numbers  $\nu_1$ ,  $\nu_2$  and  $\nu_3$  respectively. Thus, a vibrational state of water molecule is identified by a set of three vibrational quantum numbers,  $\nu = (\nu_1, \nu_2, \nu_3)$ .

The zero-point energy of water molecules is identified by  $\nu = (0, 0, 0)$  and is given as:

$$\epsilon(0,0,0) = \sum_{i=1}^3 \frac{\omega_{osc,i}}{2} \quad (2.13)$$

For water molecules,  $\epsilon(0,0,0) = 4629.6224 \text{ cm}^{-1}$ . The vibration modes and the corresponding transition frequencies for  $\text{H}_2^{16}\text{O}$  molecules are shown in Figure 2.3 [92].

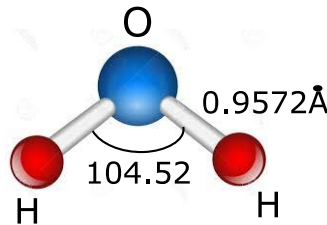


**Figure 2.2** Structure of water molecule.

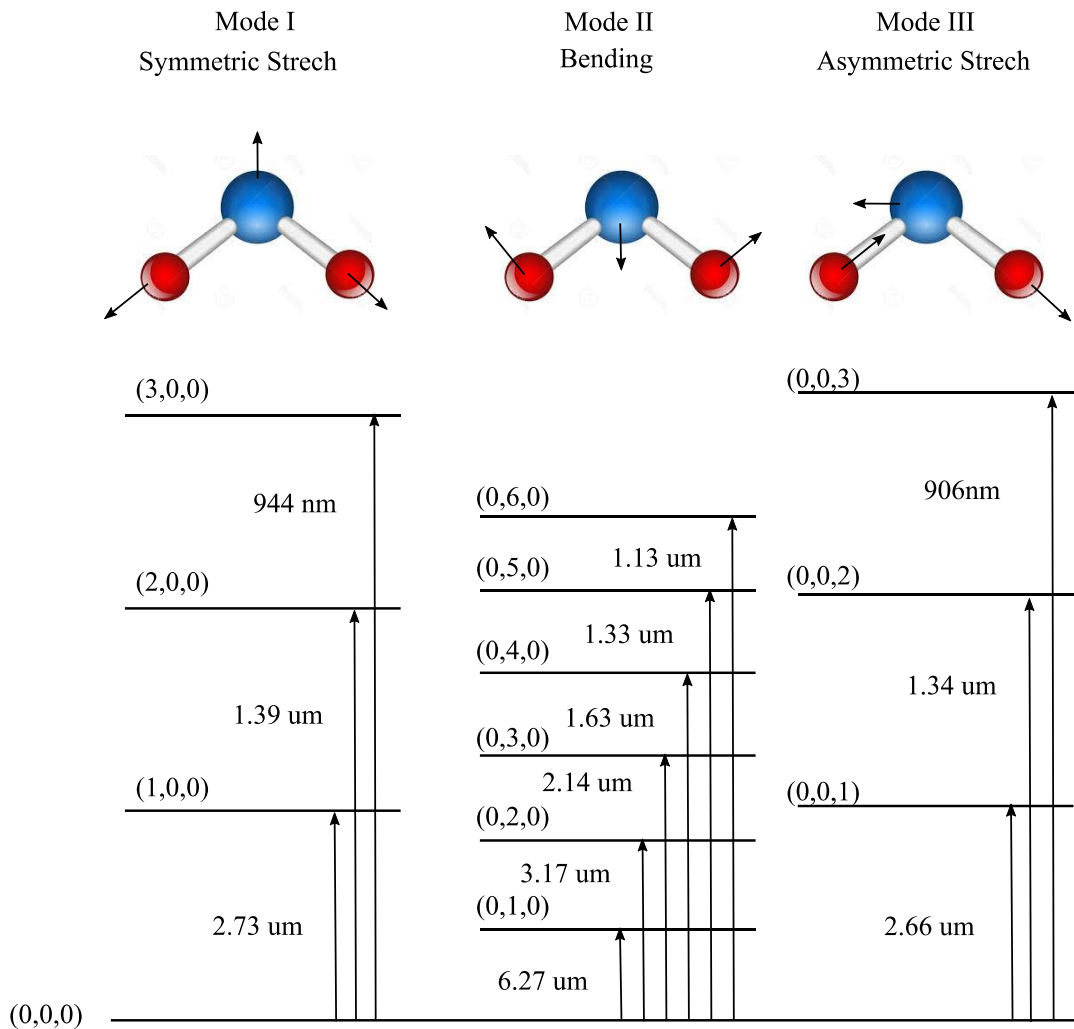


**Figure 2.3** Vibrational energy level diagram of water molecule (H<sub>2</sub><sup>16</sup>O) [92], showing three vibrational modes and the transition wavelengths corresponding to fundamental and overtone transitions.

#### 2.2.1.4.2. Rotational Energy Levels of Water

For a water molecule,  $I_A \neq I_B \neq I_C$ . Such molecules are known as asymmetric tops. The energy level structure of asymmetric molecules is very complicated with very large number of rotational energy levels designated by quantum numbers  $JK_aK_b$ , more details of which can be found in

reference [38, 93]. Here,  $J$  represents rotational quantum number along the principle axis while  $K_a$  and  $K_b$  are the projections along the principle axis.

#### 2.2.1.4.3. Effect of Isotope Substitution

There are several water isotopologues formed due to the substitution of either H or O or both by their heavier isotopes. Some of the heavier isotopologues and their natural abundances are listed in Table 2.2. The vibrational energy of these heavier variants is lower than that of  $H_2^{16}O$  due to higher effective mass as per equation (2.7). The central frequencies of some of these transition for water isotopologues are listed in reference [92]. The change in the rotation line spacing due to the isotope substitution is inversely proportional to the effective mass.

#### 2.2.1.4.4. Other Effects

The energy level structure calculated with an anharmonic oscillator and rigid rotor approximation is oversimplification of actual quantum mechanical system of the molecule. The more precise calculation of the energy levels requires inclusion of other correcting effects like centrifugal distortion, Fermi resonance, Coriolis coupling and Darling-Dennison Effect. A more rigorous treatment on the calculation of exact energy levels can be found in books on fundamentals of molecular spectroscopy [94, 95].

#### 2.2.1.5. Ro- Vibrational Absorption Spectrum of Water

Due to three vibration modes and complicated rotational energy level structure, the ro-vibrational absorption spectrum of water is very complex. The absorption spectrum of water spans the whole

spectral range from mid IR to visible region as shown in Figure 2.4. The 6.3 $\mu$  band of ro-vibrational spectrum of water is due to (0,1,0) transitions (mode II). The second band in 2.7  $\mu$ m region is known as the X band. This band is due to (1,0,0) and (0,0,1) fundamental transitions (modes I and II). In addition to, fundamental bands, there are a large number of harmonic and combination absorption bands lying in near IR region, namely  $\Omega$ ,  $\Psi$ ,  $\varphi$ ,  $\rho\sigma\tau$ , 0.8 $\mu$  and  $\alpha$ .

However, the intensities of these bands are several orders lower than the intensities of the fundamental bands. The transitions corresponding to these bands are listed in Table 2.3. Extremely weak absorption bands can also be observed in the visible region.

**Table 2.2** Natural abundance of water isotopologues [43].

Water Isotopologue	Isotopic Composition of Natural Water	Abundance of H and O
$\text{H}_2^{16}\text{O}$	99.7317 %	$^1\text{H}$ : 99.98% $^{16}\text{O}$ : 99.759%
$\text{H}_2^{18}\text{O}$	0.199983 %	$^{18}\text{O}$ : 0.204%
$\text{H}_2^{17}\text{O}$	0.0372 %	$^{17}\text{O}$ : 0.037%
$\text{HD}^{16}\text{O}$	310 ppm	$^2\text{H}$ (D): 155 ppm
$\text{HD}^{18}\text{O}$	623 ppb	
$\text{HD}^{17}\text{O}$	116 ppb	
$\text{D}_2^{16}\text{O}$	26 ppb	
$\text{HT}^{16}\text{O}$	$0 - 10^{-14}$	$^3\text{H}$ (T): trace
$\text{T}_2^{16}\text{O}$	$\sim 0$	

**Table 2.3** List of absorption band of water spectrum and the vibrational transition involved.

Absorption Bands	Constituent Vibrational Transitions
6.3 $\mu$	(0,1,0)
X	(0,2,0) (1,0,0) (0,0,1)
$\Omega$	(1,1,0) (0,1,1)
$\Psi$	(1,2,0) (0,2,1) (2,0,0) (0,0,2) (1,0,1) (0,5,0)
$\phi$	(2,1,0) (1,1,1) (0,1,2) (0,6,0)
$\rho\sigma\tau$	(2,2,0) (1,2,1) (0,2,2) (3,0,0) (2,0,1) (1,0,2) (0,0,3)
0.8 $\mu$	(1,1,2) (2,2,1) (1,7,0) (1,1,2) (1,0,3)
$\alpha$	(1,2,2) (2,2,1) (1,7,0) (2,0,2) (3,0,1) (0,7,1) (1,2,2) (0,2,3)

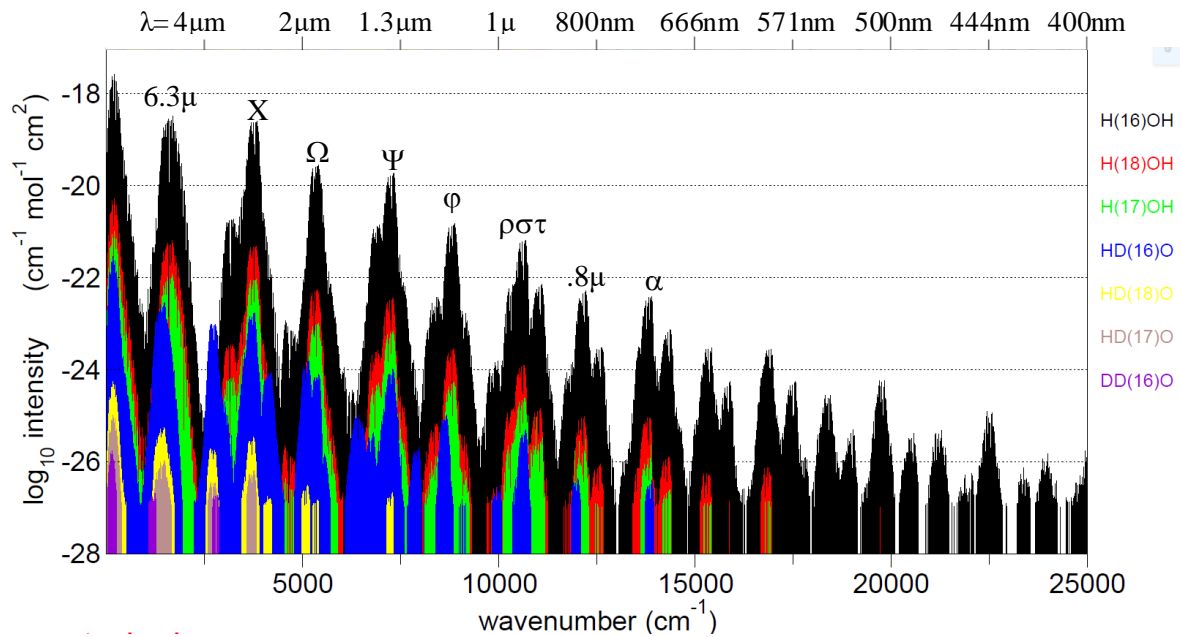


**Figure 2.4** Stick plot of absorption peaks of water molecule and its isotopologues from IR to visible range [96].

### 2.2.2. The LAS System

A basic LAS system consists of a tunable laser, an absorption cell and suitable detector as shown in Figure 2.5. The laser should have emission wavelength matching with absorption peaks of the gases under study. The absorption cell of length  $d$ , contains the sample at appropriate temperature and pressure. The laser intensity transmitted through the absorption cell is measured while scanning the laser wavelength. The detector could be a photodiode, photo-conductors or thermopile depending on the wavelength under consideration. The recorded signal is then processed to obtain the required information. The LAS finds application in concentration determination, molecules identification and in basic physics studies [28].

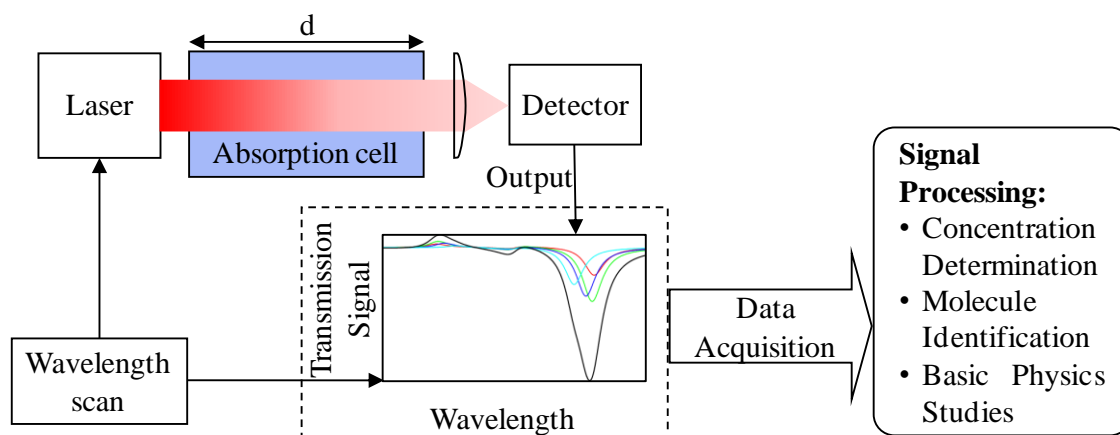


**Figure 2.5** The block diagram showing the basic blocks of a LAS system. A basic LAS system consists of laser source with wavelength scanning, an absorption cell, detector and a signal processing system.

Since, the fundamental transitions of almost all molecules are in the mid IR region, the concentration measurement studies are mainly performed in this region. However, both the lasers and detectors available in mid IR region require cryogenic cooling. This makes the system bulky and difficult to operate. Hence, the use of such high sensitivity trace gas detection systems is

limited to a laboratory setup. The availability of compact tunable diode lasers in the near IR region has made it possible to use overtone and combination ro-vibrational bands for concentration determination. Although the strength of these peaks is 300 times weaker than fundamental transitions, due to higher stability and output power of diode laser and availability of better detectors, very high sensitivity is achievable in near IR range [39].

### 2.2.3. Concentration Determination from Laser Absorption Spectra

The quantification of concentration of gases by LAS is based on Beer-Lamberts law [40]:

$$I(\nu) = I_0 e^{-\alpha(\nu)d} \quad (2.14)$$

where  $I(\nu)$  is the transmitted light,  $I_0$  is the incident light intensity,  $\alpha(\nu)(\text{cm}^{-1})$  is absorption coefficient of the sample at frequency,  $\nu$  and  $d$  (cm) is optical pathlength. In the infrared region energy is usually expressed in  $\text{cm}^{-1}$  ( $\nu=1/\lambda$ , where  $\lambda$  is wavelength in cm). The quantity  $I/I_0$  is known as the transmittance. The absorbance ( $A$ ) for a cell of length  $d$ , is defined as:

$$A = \alpha(\nu)d = \ln\left(\frac{I_0}{I}\right) \quad (2.15)$$

The absorption coefficient  $\alpha(\nu)$  is total absorption of all the species in the sample at  $\nu$  [41]:

$$\alpha(\nu) = \sum_m \sigma_{\nu m} N_m \quad (2.16)$$

where,  $N_m$  is the molecular density of the gas species labelled by index  $m$ , and is given by:

$$N_m = \frac{qP}{k_B T} \quad (2.17)$$

where  $q$  is volume mixing ratio,  $k_B$  is the Boltzmann constant,  $T$  is the gas temperature,  $P$  is the total gas pressure. The molecular absorption cross section,  $\sigma_{vm}(\nu)$ , depends on frequency and has the units of square centimetre per molecule ( $\text{cm}^2/\text{molecule}$ ). It is the sum of cross sections of all individual ro-vibrational transitions:

$$\sigma_{vm}(\nu) = \sum_n S_n \gamma_{\nu_n} \quad (2.18)$$

where  $\nu_n$  is the frequency of the  $n^{\text{th}}$  transition, expressed in  $\text{cm}^{-1}$  and  $S_n$  is its intensity (or line strength), expressed in units of  $\text{cm}^{-1}/(\text{molecule}\cdot\text{cm}^{-2})$ . The function  $\gamma$  ( $1/\text{cm}^{-1}$ ) describes the peakshape of the  $n^{\text{th}}$  transition. The integration of absorption cross-section gives line-intensity  $S_n$  which is independent of broadening mechanism.

$$\int_{-\infty}^{\infty} \sigma_{vm} d\nu = \sum_n S_n \quad (2.19)$$

The peakshape is affected by various broadening mechanisms. The broadening of the spectral peak is attributed to both, Doppler effect (Gaussian profile) and the collision effect (Lorentzian profile) [41]. The Doppler broadened normalized Gaussian peak profile is given as:

$$\gamma_G(\nu) = \frac{1}{\sqrt{2\pi} \sigma_G} e^{-\frac{(\nu-\nu_c)^2}{2\sigma_G^2}} \quad (2.20)$$

$\sigma_G$  represents the standard deviation for a Gaussian profile given by the following expression:

$$\sigma_G(\text{cm}^{-1}) = \nu_c \sqrt{\frac{k_B T}{Mc^2}} \quad (2.21)$$

where,  $\nu_c$  is the centre frequency of the transition line ( $\text{cm}^{-1}$ ),  $k_B$  is the Boltzmann constant,  $T$  is the temperature of the sample,  $M$  is the molecular mass of the gas (Kg) and  $c$  is speed of light. The

half width at 1/e of maximum intensity is  $\sqrt{2}\sigma_G$  and the half width at half maximum (HWHM) is given as,  $\Gamma_G = \sqrt{2\ln 2} \sigma_G$ . On the other hand, the pressure broadened normalized Lorentzian profile is given by:

$$\gamma_L(\nu) = \frac{1}{\pi} \frac{\Gamma_L}{(\nu - \nu_c)^2 + \Gamma_L^2} \quad (2.22)$$

where  $\Gamma_L$  is pressure broadened Lorentzian HWHM given by an empirical expression:

$$\Gamma_L = \left( \frac{T_{ref}}{T} \right)^n (\gamma_{air}(P - P_m) + \gamma_{self}P_m) \quad (2.23)$$

$\gamma_{air}$  ( $\gamma_{self}$ ) is the half width air (self) broadening coefficient,  $T_{ref}$  is the reference temperature (296 K),  $P$  is the total pressure and  $P_s$  is the partial pressure (atm) of the sample and  $n$  is the temperature coefficient for broadening. The composite peak shape is given by the convolution of both Lorentzian and Gaussian profile. The resultant peak shape is known as Voigt profile,  $\gamma_V(\nu)$ :

$$\gamma_V(\nu) = \frac{\Gamma_L}{\sqrt{2}\sigma_G\pi^{3/2}} \int_{-\infty}^{\infty} \frac{e^{-(\nu-\nu')^2/2\sigma_G^2}}{(\nu_c - \nu')^2 + \Gamma_L^2} d\nu' \quad (2.24)$$

The wings of Voigt profile have a Lorentz shape while the peak centre or core has a Gaussian peak shape. The Voigt peak profile function is calculated in this thesis using its empirical approximation [42]:

$$\gamma_V(\nu) = \frac{(1-x)e^{-0.693y^2} + \frac{x}{1+y^2} + 0.016(1-x)x(e^{-0.0841y^{2.25}} - \frac{1}{1+0.021y^{2.25}})}{2\Gamma_V(1.065 + 0.477x + 0.058x^2)} \quad (2.25)$$

where  $x$  and  $y$  are scaled variables and  $\Gamma_V$  is Voigt halfwidth expressed by:

$$\Gamma_V = 0.5346\Gamma_L + \sqrt{0.2166\Gamma_L^2 + \Gamma_G^2}$$

$$x = \frac{\Gamma_L}{\Gamma_V} \quad (2.26)$$

$$y = \left| \frac{\nu - \nu_c}{\Gamma_V} \right|$$

For computation of the concentration of gaseous species from the absorption spectrum, quantitative knowledge of these spectroscopic features such as  $\nu_n$ ,  $S_n$ , and  $\gamma_n$  is necessary. These parameters are well documented on the basis of measurements and calculations for many lightweight gas molecules. Compiled databases such as HITRAN [43-45] and GEISA [46, 47] extensively lists these parameters across the microwave and infrared spectral ranges. The availability of these databases is helpful in selecting a suitable absorption peak and for quantitative analysis of the unknown gas mixture.

#### **2.2.4. Performance Characteristics of LAS Detection System**

There are numerous spectroscopic techniques available for the detection of trace gases. Choosing a suitable technique amongst them is based on their performance characteristics as well as the size of the equipment and cost involved. Most important performance characteristics of spectroscopic trace gas detection systems are sensitivity and selectivity as described below.

The selectivity of the gas sensor is defined as ratio of response from ‘the desired target gas’ to ‘an interfering gas’. The absorption spectroscopic technique is highly selective, when an isolated absorption peak can be identified for the target gas/ molecule. Thus, when molecules are studied

using vibrational lines, then one must choose appropriate peak where there is no overlapping peak from the other molecules.

Sensitivity of the detector is its ability to distinguish between the small differences in the gas concentration and the minimum concentration it can measure. Like other high sensitivity technique, the LAS experiments for quantification of trace gases with lower detection limit down to ppt also suffer from low Signal to Noise Ratio (SNR) owing to weak absorption signal. Hence, such techniques rely heavily on signal averaging plus other techniques for sensitivity improvement (discussed later in Section 2.3). For such experiments two commonly used sensitivity parameters to compare the performance of instruments are [48]:

(a) Minimum Detectable Absorption (MDA)

MDA is defined as the fractional absorption equivalent to  $1\sigma$  uncertainty in an actual measurement, normalized to integration time of one second.

$$\text{MDA} = \left( \frac{\Delta I}{I} \right)_k \sqrt{\tau_{\text{int}}} \quad (2.27)$$

where  $\Delta I/I$  is  $1\sigma$  residual of measured optical intensity,  $\tau_{\text{int}}$  is the total integration time for  $k$  number of scans.

(b) Noise Equivalent Absorption Sensitivity (NEAS)

NEAS is another commonly used metric of instrument performance which is basically the MDA scaled to effective path length ( $L_{\text{eff}}$ ):

$$\text{NEAS} = \frac{\text{MDA}}{L_{\text{eff}}} \quad (2.28)$$

(c) Signal Averaging and Allan Variance

From the expression of MDA, it is intuitive that the sensitivity can be improved by signal averaging for longer time. However, sensitivity improvement by signal averaging is limited by the stability of the whole experimental system. The stability of a trace gas detection instruments is analysed in terms of Allan variance [49]. Allan variance distinguishes high frequency random noise from drifts at longer time scales and quantifies the maximum time for which signal averaging can improve the detection limit.

For calculation of Allan variance, let us assume a set of  $n$  time-series data represented by  $x_i$  (for  $i$  varying from 1 to  $n$ ). Average value  $A$  and variance  $\sigma$  of this set can be defined as:

$$A = \frac{1}{n} \sum_{i=1}^n x_i \text{ and } \sigma_n^2 = \frac{1}{n-1} \sum_{i=1}^n (x_i - A)^2 \quad (2.29)$$

When  $n$  elements of the original data set are divided into  $m$  subsets, then number of elements in each subset would be  $k=n/m$ . For  $j^{\text{th}}$  subgroup average value  $A_j$ , and variance  $\sigma_j^2$  can be calculated as

$$A_j = \frac{1}{k} \sum_{l=1}^k x_{(j-1)k+l} \text{ and } \sigma_j^2 = \frac{1}{k-1} \sum_{l=1}^k (x_{(j-1)k+l} - A_j)^2 \quad (2.30)$$

The optimum averaging group size is determined on the basis of  $m$  sample variance defined as:

$$\sigma_{\text{Allan}}^2(m) \equiv \sigma^2(\tau_{\text{int}}) = \frac{1}{2(m-1)} \sum_{j=1}^{m-1} (A_{j+1} - A_j)^2 \quad (2.31)$$

where  $\tau_{\text{int}}$  is called integration time, i.e. the time required to collect  $k$  samples and for sampling interval of  $\Delta t$  (time interval between starting time two successive time series),  $\tau_{\text{int}}=k*\Delta t$ . To obtain optimum integration time, Allan variance versus integration time is plotted on log –log scale. For

short integration time, Allan variance  $\sigma^2(\tau_{\text{int}})$  decreases with integration time until a minimum is reached. This integration time is known as optimum integration time  $\tau_{\text{opt}}$ . For integration times longer than  $\tau_{\text{opt}}$ , drift dominates the system and variance increases.

### **2.3. LAS TECHNIQUES FOR HIGH SENSITIVITY**

The LAS instruments directly measures abundance of the absorbing species from the change in the laser intensity as given by Beer Lambert law [40]. However, for trace level detection, a very large path length is required to achieve sufficient sensitivity. The sensitivity of a laser spectrometer is proportional to the signal-to-noise ratio of recorded data. Thus, techniques for sensitivity improvement are based on utilizing low noise systems and/ or increasing the absorption path length. Some of these techniques are detailed below.

#### **2.3.1. Optical Multipass Cell**

Optical multipass cells consist of a set of high reflectivity mirrors, arranged in geometry such that the light makes large number of passes before exiting the cell. They have been developed to achieve high sensitivity as the absorption signal is directly proportional to the interaction path length. These cells are extensively utilized for compact instrumentation as they provide much longer path lengths in small cell volumes. Simplest of these multipass cells is a spherical cavity resonator, Herriott cell [50-54]. It consists of two high reflectivity spherical mirrors of equal focal lengths  $f$ , separated by a distance  $d$ , which is less than or equal to  $4f$ . The laser beam enters through an off-axis hole. The beam is reflected back and forth in the cavity till it exits through the entrance hole after designated number of passes,  $N_r$ , following an elliptical pattern of reflection spots on

the mirrors. The condition when the laser beam exit exactly at the entry point of beam is known as re-entrant condition. The path length extension in a conventional spherical mirror Herriott cell is limited by the number of spots that can be fitted along elliptical pattern on mirrors without overlap or clipping. Thus, to increase the path length either one must use larger mirrors or longer cell which translates to the increased cell volume.

It is desirable to increase the density of spots on mirrors to increase the path length of the beam inside the cell instead of increasing its volume. Such a high density cell was first built using a pair of astigmatic mirrors [55]. This cell had a spot pattern formed due to precession of ellipses, resulting in a Lissajous pattern distributed on the entire surface of the mirrors. It results in an increased density of passes by a factor of three or more [56, 57]. The drawback of this design is that for a desired  $N_r$  and separation  $d$ , focal lengths  $f_x, f_y$  in orthogonal planes must be specified to a tolerance of 100 ppm, which is impractical to manufacture. Later, Keabian proposed to rotate one of the mirrors relative to the other around the  $Z$ - axis to compensate imprecision in focal lengths with slight adjustment in  $d$  [56]. However, this approach makes alignment of cell difficult. Furthermore, astigmatic mirrors must be custom made and are very costly.

Another way to generate dense Lissajous pattern was proposed by Hao *et al.* using two cylindrical mirrors with different focal lengths and principal axes aligned orthogonal to each other [58, 59]. In essence, it creates a cavity with mirror of focal length  $f_x(f_y)$  on one side and a plane mirror on other side, in  $X$  ( $Y$ ) direction. However, it permits only a few solutions where re-entrant condition is satisfied. J. A. Silver proposed two different approaches to achieve a dense pattern multipass cell [60]. In the first approach, two matched cylindrical mirrors were used. A wide diversity of re-entrant Lissajous patterns can be formed by rotating the principal axes of one mirror along  $Z$ - axes,

with respect to the other. In the second approach, only one spherical mirror in spherical cavity is replaced by cylindrical mirror. The major drawback of second approach is that the rays are never exactly re-entrant. Hence near re-entrant solutions were utilized.

In this thesis, a simple method to obtain dense multipass pattern by inserting a cylindrical lens inside a spherical resonator is proposed. A theoretical description and stability condition for the cell is presented. Design aspects leading to some practical designs are discussed in CHAPTER 3.

### 2.3.2. Modulation Spectroscopy

Modulation techniques have been developed for increasing SNR by the reduction of the effective noise in the measurement. In modulation techniques, the signal to be measured is modulated which transforms it from the highly noisy low frequency region to a less noisy high frequency region. The noise components associated with the signal are then removed by filtering. This noise free signal is again transformed back to original frequency region by the process of demodulation.

The optical probe beam with a sinusoidal modulation having modulation index  $m$ , modulation frequency  $\omega_m$  and optical carrier frequency  $\omega_0$  is given by [61]:

$$\begin{aligned} E(t) &= E_0 \exp(i \omega_0 t) \exp[i(\omega_m t + m \sin \omega_m t)] \\ &= E_0 \exp(i \omega_0 t) \sum J_n(m) \exp(j n \omega_m t). \end{aligned} \tag{2.32}$$

Written as summation of  $n^{\text{th}}$ -order Bessel functions,  $J_n$ , and the co-efficient of  $J_n$  characterizes frequency components of the modulated light spectrum. Depending on values of modulation index  $m$  and frequency  $\omega_m$ , modulation spectroscopy is divided into two categories: Frequency Modulation Spectroscopy (FMS) and Wavelength-Modulation Spectroscopy (WMS). In FMS, the modulation frequency  $\omega_m$  is greater than the half-width ( $\Gamma$ ) of the probed absorption feature (100

MHz to several GHz range) and modulation index  $m$  is small  $m \ll 1$ . In WMS, the modulation frequency is less than the optical half-width of the probed absorption feature (kHz to several MHz range) with  $m \gg 1$  [62].

### **2.3.3. Cavity Enhanced Absorption Spectroscopy (CEAS) Techniques**

An optical cavity consisting of two highly reflectivity mirrors ( $R > 99.9\%$ ) can provide an effective path length of few kilometres. The use of optical cavities for sensitivity enhancement has attracted attention of the spectroscopic community leading to the development CEAS techniques. Advancement in cavity enhanced techniques allow construction of scalable, modular, lightweight instrument with the sensitivity necessary for the most demanding measurements while providing multiple, direct calibration methods. Important properties of optical cavity are discussed in Appendix II, while the spectroscopic techniques using an optical cavity viz. Intra-Cavity Absorption Spectrometry (ICAS) [63], Cavity Ring-Down Spectroscopy (CRDS) [64, 65] and Integrated Cavity Output Spectroscopy (ICOS) [21, 66], etc., are introduced in Section 2.4.

## **2.4. INTRODUCTION TO HIGH SENSITIVITY TECHNIQUES USING OPTICAL CAVITIES**

Many techniques have been introduced to take advantage of path length enhancement provided by an optical cavity [22]. Some of these are detailed below:

### **2.4.1. Cavity Ring-Down Spectroscopy (CRDS)**

CRDS is the most mature of the CEAS techniques [67]. The CRDS technique is based on the direct proportionality of cavity decay time on the absorption losses [68]. A narrowband laser light is

coupled into a highly reflective optical cavity and then interrupted. The transmitted power decays exponentially with time at a rate proportional to the losses inside the cavity. These cavity losses include mirror reflectivity, scattering and light absorption by intra-cavity species. By monitoring cavity decay, in the presence and absence of an absorber, absolute concentration dependent absorption coefficient can be determined. The decay of transmitted light intensity through cavity is given by [68]:

$$I(t, \nu) = I_0 e^{-\frac{t}{\tau_{RD}(\nu)}} \quad (2.33)$$

where  $I_0$  is the transmitted intensity when laser power is interrupted,  $t$  is time elapsed after laser is interrupted and  $\nu$  is laser frequency,  $\tau_{RD}(\nu)$  is ring down time constant. The absorption coefficient,  $\alpha(\nu)$ , is calculated from the measured time constant using the following equation:

$$\tau_{RD}(\nu) = \frac{d}{c(1 - R_m + \alpha(\nu)d)} \quad (2.34)$$

The concentration of the absorbing gas is obtained from the difference in time constant of empty cavity (i.e. cavity without absorber) and time constant with absorber.

#### **2.4.2. Cavity Attenuated Phase Shift (CAPS) Spectroscopy**

CAPS Spectroscopy uses phase delay introduced by the optical cavity as a monitor of time constant [69]. CAPS spectroscopy has many advantages over CRDS including higher duty cycle and higher input signal strength on the detector making measurements much less susceptible to the detector noise. Detection bandwidth in CAPS can be made extremely narrow eliminating the need of fast detection electronics. In addition, the contribution from the detector and electronic noise is lower. CAPS spectroscopy makes use of Continuous Wave (CW) laser sources, which are much more

readily available than pulsed sources in mid-infrared region of the spectrum. Even though CAPS systems provide direct measure of the cavity decay constant, it is limited by the error in the phase determination of a noisy cavity signal. Hence, precision of measurement becomes a main problem with this technique.

### **2.4.3. Integrated Cavity Output Spectroscopy (ICOS)**

The ICOS was first demonstrated by O'Keefe [21, 66, 70]. It makes use of steady state power transmitted through the optical cavity rather than temporal properties induced by the cavity. In this technique, integrated intensity passing through the optical cavity is used for sensitive absorption measurements. A CW laser is mode matched to the cavity's lowest transverse electromagnetic mode,  $TEM_{00}$ . When the laser wavelength is swept, resonance peaks corresponding to the cavity mode spectrum are observed. The amplitude of the resonant peaks reduces due to absorption losses by the molecules inside the cavity. The change in the amplitude of these resonance peaks is proportional to the absorption coefficient of the sample. Thus, absorption spectrum is obtained at discrete points when laser frequency is tuned around the absorption peak. The cavity length scanning is required to shift the resonant peaks in order to record a continuous spectral feature. However, averaging over a large number of such scans is necessary to eliminate the mode spectrum, which remains the main source of noise limiting the sensitivity in ICOS technique.

This limitation has been addressed by Paul *et al.* and the technique is modified to Off-Axis ICOS (OA-ICOS) [48, 71, 72]. In OA-ICOS, laser beam enters the cavity at an off-axis point on the cavity mirror and is coupled to multiple  $TEM_{nm}$  modes, thus dramatically reducing the amplitude noise associated with the resonant behaviour of the optical cavity [73]. The alignment patterns are

similar to Herriot multipass cells for spherical as well as astigmatic mirrors. The desired alignment is the one in which the cavity resonances are effectively suppressed, and the transmission is wavelength independent. It is achieved when cavity FSR is significantly narrower than the laser bandwidth. As the resonance modes are suppressed, the peak transmission is significantly reduced. Figure 2.6 shows the compression in FSR of cavity with off-axis alignment relative to the on-axis alignment and absorption spectra observed with on-axis and off-axis alignment. However, for OA-ICOS technique, meeting re-entrant condition is not necessary; hence it is easy to align. Thus, the technique is insensitive to vibration, therefore is simple and robust to implement, which makes it suitable for portable instrumentation for field applications.

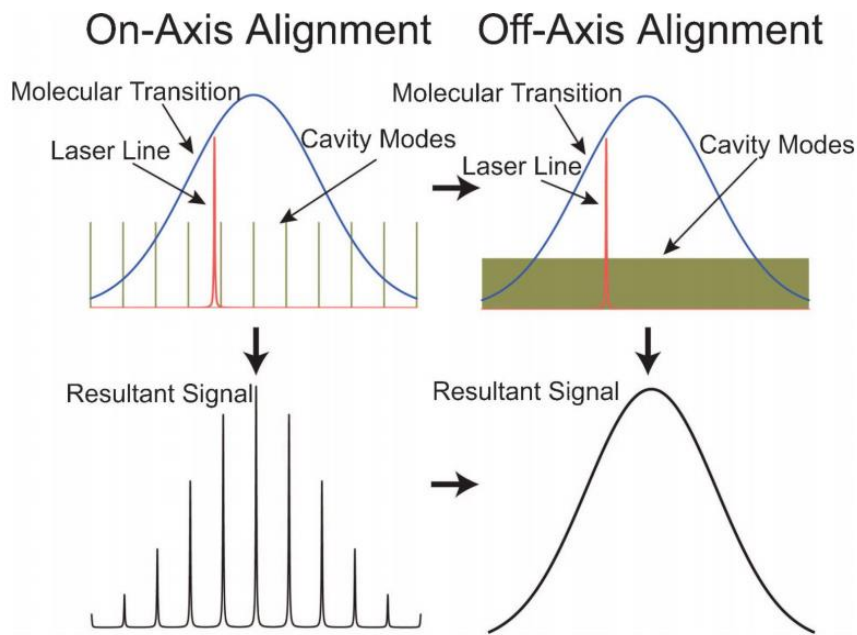


**Figure 2.6** Top panel shows mode spectra with on-axis and off-axis alignment superimposed with laser spectra and molecular transition. The lower panels illustrate the resultant signals from each alignment [73]. Reproduced from [73] with the permission of AIP Publishing.

This technique is effectively a steady state absorption method with a gain owing to path length enhancement by the cavity. This method has advantage of using CW laser, maximizing light intensity on the detector, while removing strenuous demands on detection electronics in maintaining frequency standards or high-speed acquisition. It however, suffers from noise due to spurious resonant coupling to cavity modes. The coupling of laser to the cavity is not ideal, due to chaotic behaviour of a passive optical cavity. Unlike previous two methods, while precision can be directly quantified, calibration for accuracy requires comparison with a known sample or cross-calibration with another method.

#### **2.4.4. Other Cavity Enhanced Techniques**

The limiting factor in achieving high sensitivity is the frequency response of the cavity, which directly translates to the noise in the resulting absorption spectrum. More sensitive methods involve locking the laser wavelength to cavity-mode resonance. There are two variants of such techniques: laser-locked CRDS [74] and Noise Immune Cavity-Enhanced Optical Heterodyne Molecular Spectroscopy (NICE-OHMS) [75]. Other techniques include Phase-Shift Off-Axis Cavity-Enhanced Absorption Spectroscopy (PS-OA-CEAS) [76], Optical Feedback CEAS (OF-CEAS) [77], Wavelength Modulation ICOS (WM-ICOS) [78], BroadBand CEAS (BB-CEAS) [79].

#### **2.4.5. Comparison of High Sensitivity LAS Techniques**

The sensitivity of trace gas detection system can be compared in terms of performance using the minimum detectable absorption coefficient  $\alpha_{\min}$ . Table 2.4 summarizes some of the pioneering

work in trace water vapour ( $\text{H}_2^{16}\text{O}$ ) detection using diode laser spectroscopic techniques. From the comparison, it is clear that OA-ICOS technique can be used for high sensitivity portable trace gas detection.

**Table 2.4** Comparison of performance of various reported techniques for trace detection of water vapour.

S. No.	Wave-Length (nm)	Path Length (km)	Averaging Time (s)	Specified Sensitivity	Minimum Detectable Gas Concentration	Technique Used
1	833.6	0.350	0.002	$1.7 \times 10^{-9} \text{cm}^{-1}$	1 ppm	CRDS [80]
2	1393	0.010	50	Not stated	1.6 ppb	TT-FMS [81]
3	1392.5	0.0467	70	$3.5 \times 10^{-9} \text{cm}^{-1} \text{Hz}^{-1/2}$	70 ppt	2f WMS Herriott multipass cell [82]
4	1393	.056	1	$2 \times 10^{-6}$	2 ppm	Herriot multipass cell [83]
5	935	.0068	1	Not Stated	100 ppm	off-axis astigmatic multipass absorption cell [84]
6	1392		30	$4 \times 10^{-10} \text{cm}^{-1} \text{Hz}^{-1/2}$	200 ppm <sup>#</sup>	OF-CEAS [85]
7	652.0	~10.8	10	$2.9 \times 10^{-9} \text{cm}^{-1}$	Not stated	BB-CEAS [86]
8	1651	~12	5	$1.6 \times 10^{-11} \text{cm}^{-1} \text{Hz}^{-1/2}$	50 ppm	CRDS [87]
9	6700	4.2	100	$2.4 \times 10^{-11} \text{cm}^{-1} \text{Hz}^{-1/2}$	0.28 ppm*	OA-ICOS [48]

#Isotopic ratio-  $\delta^{18}\text{O}$ : 1‰,  $\delta^{17}\text{O}$ : 3‰,  $\delta\text{D}$ : 9‰

\*Isotopic ratio-  $\text{H}_2^{18}\text{O}$ : 0.16 ppbv, HDO: 0.10 ppbv,  $\delta\text{D}$ : 50‰,  $\delta^{18}\text{O}$ : 30‰

## 2.5. SUMMARY

In this chapter, the basic principle of LAS has been discussed. Since for trace amount of gases, the absorption signal is buried in the noise, a sensitivity enhancement technique is required. A brief

introduction to multipass cell, wavelength modulation spectroscopy and optical cavity based sensitivity enhancement techniques are presented in this chapter. Among them cavity enhanced technique is found to be most suitable of our current application on trace detection of heavy water of monitoring coolant leaks in the PHWRs. Basic theory of optical cavity and techniques are discussed. Based on the literature available, a high sensitivity technique known as OA-ICOS has been selected for the development of the heavy water leakage monitoring system. The design requirements, challenges involved and the solutions are presented in the subsequent chapters.



## CHAPTER 3

### NOVEL ASTIGMATIC MULTIPASS CELL DESIGN

---

Optical multipass cells and cavities play an important role in trace gas detection by providing path length enhancement with small volume. In this thesis, a novel design of a multipass cell has been proposed for trace gas detection. The schematic of the multipass cell is shown Figure 3.1. It consists of two spherical end mirrors M1 and M2 with a cylindrical lens L. Distance between the mirrors is 'd' and the lens is placed at distance 'a' from the mirror M2. As cylindrical lens-mirror (L-M2) pair effectively acts as an astigmatic mirror, optical features for this system are similar to an astigmatic mirror system.

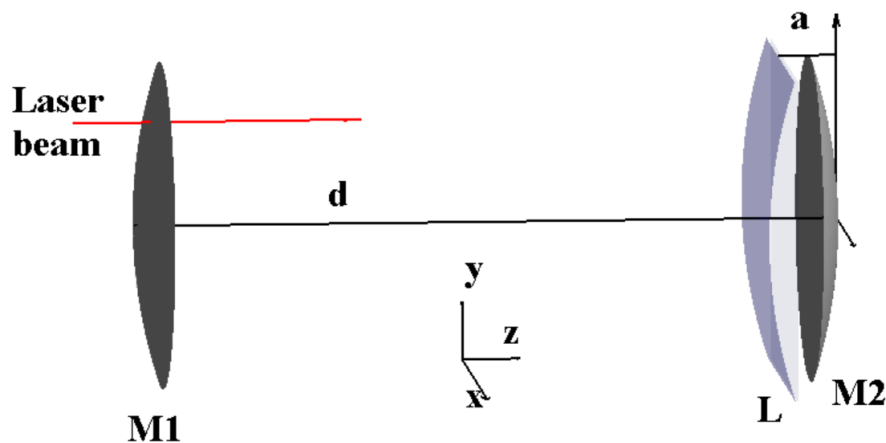


**Figure 3.1** Optical layout of modified Herriott cell with cylindrical lens. M1, M2: High reflectivity spherical end mirrors; 'd': distance between M1 and M2; L: Cylindrical lens; 'a': distance between M2 and L. The laser beam enters through a hole in mirror M1, as shown in red.

For this optical system to be usable as multipass cell, it should satisfy both stability and re-entrant condition. The condition when the laser beam exit exactly at the entry point of beam is known as re-entrant condition. In this chapter, these conditions based on paraxial ray approximation are derived theoretically. Also ray tracing based simulations are used to study some of the important design parameters that are the stability of alignment, and overlap between the laser beam spots.

### 3.1. THEORETICAL DESCRIPTION OF RE-ENTRANT CONDITION

In Cartesian coordinate system, let centre of M1 be at origin, M2 be at (0, 0, d) and L be at (0, 0, d-a). Here, z-axis is the optical axis of the system and (x, y) plane is parallel to mirror's surface. When the principal axis of the cylindrical lens is along x-axis, then the focal length in x-direction remains unaffected. Along the y-axis, lens-mirror combination (L-M2) can be replaced with an equivalent mirror of focal length  $f_{eq,y}$  with principal focal plane at  $\delta d$  from the mirror. The values of  $f_{eq,y}$  and  $\delta d$  are given by the following equations under paraxial approximation:

$$\frac{1}{f_{eq,y}} = \frac{1}{f_m} + \frac{2}{f_l} - \frac{a}{f_l} \left( \frac{2}{f_m} + \frac{2}{f_l} - \frac{1}{f_l f_m} \right) \quad (3.1)$$

$$\delta d = \frac{a^2}{f_l - a} \quad (3.2)$$

where  $f_m$  is the focal length of the spherical mirror and  $f_l$  is the focal length of the cylindrical lens.

A general resonance condition for a cavity formed by two mirrors having Radii Of Curvature (ROC)  $\mathfrak{R}_1$  and  $\mathfrak{R}_2$  separated by a distance  $d$  has been derived by Ramsay *et al.* [53] and is given by the following equation:

$$d_{\pm} = \frac{\mathfrak{R}_1 + \mathfrak{R}_2}{2} \pm \frac{1}{2} (\mathfrak{R}_1^2 + \mathfrak{R}_2^2 + 2\mathfrak{R}_1\mathfrak{R}_2\cos\theta)^{1/2}, \quad \theta = \frac{\Theta M}{N_r} \quad \forall 0 \leq M \leq \frac{N_r}{2} \quad (3.3)$$

where  $\Theta = 2\pi$  for beam entering an off-axis hole, and  $\Theta = \pi$  when beam enters the cavity at the centre position,  $N$  is the number of round trips and  $M$  is the number of rotations.

To obtain the re-entrant condition, cavity can be treated independently in two orthogonal axes with separate solutions along  $x$  and  $y$  directions. Along the  $x$ -axis, re-entrant condition will remain the same as that for a spherical Herriott cell and is given as:

$$d = 2f_m(1 \pm \cos \theta_x), \quad \theta_x = \frac{\Theta M_x}{2 N_x} \quad \forall 0 \leq M_x \leq \frac{N_x}{2} \quad (3.4)$$

where  $M_x$  is the number of rotations and  $N_x$  is the number of round trips after which beam becomes re-entrant (for solution along  $x$ -axis). However, along the  $y$ -direction, the ray path will be affected by cylindrical lens placed in front of the mirror. The re-entrant condition can be obtained by substituting  $\mathfrak{R}_1 = 2f_m$  &  $\mathfrak{R}_2 = 2f_{eq,y}$  and replacing  $d$  by  $d - \delta d$  in equation (3.3):

$$d - \delta d = f_m + f_{eq,y} \pm (f_m + f_{eq,y} + 2f_m f_{eq,y} \cos \theta_y)^2 \quad (3.5)$$

$$\theta_y = \frac{\Theta M_y}{N_y} \quad \forall 0 \leq M_y \leq N_y \quad (3.6)$$

where  $M_y$  is the number of rotations for  $y$ -direction and  $N_y$  is the number of round trips after which beam becomes re-entrant for  $y$  direction solution. The re-entrant condition can be attained for certain lens positions for a chosen focal length  $f_1$ . As the analytical solution of the above equation is cumbersome,  $y$  direction re-entrant conditions are obtained numerically.

The re-entrant number  $N_r$ , for the astigmatic cell is given by:

$$N_r = \text{Least common multiple } (N_x, N_y) \quad (3.7)$$

As the above stated re-entrant condition can be satisfied for a large combination of  $M_x$ ,  $N_x$ ,  $M_y$  and  $N_y$  for a given spherical cavity, a large variety of spot patterns are possible. It should be noted that for a given spherical cavity, the choice of focal length of the lens is constrained by the stability condition. The  $f_l$  should be chosen such that the following condition is satisfied:

$$\begin{aligned} 0 \leq d/2 \leq f_{eq,y}, \quad f_m \leq d/2 \leq f_m + f_{eq,y} & \text{ for } f_{eq,y} < f_m \text{ i. e. converging lens} \\ 0 \leq d/2 \leq f_m, \quad f_{eq,y} \leq d/2 \leq 2f_m & \text{ for } f_{eq,y} > f_m \text{ i. e. diverging lens} \end{aligned} \quad (3.8)$$

### 3.2. ALGORITHM FOR RAY TRACING

A computer program was written to trace the ray path and to obtain a spot pattern on the mirrors in the proposed cell. The ray tracing simulation was performed using paraxial ray tracing method known as matrix method of ray transformation. In this method, the transformation of ray parameters (that are coordinates and slope) after passing through an optical element is represented by ABCD matrix, and is given as:

$$\begin{pmatrix} x_0 \\ \theta_0 \end{pmatrix} = \begin{pmatrix} A & B \\ C & D \end{pmatrix} \begin{pmatrix} x_1 \\ \theta_1 \end{pmatrix} \quad (3.9)$$

The ABCD matrix for some common optical elements is given in Table 3.1.

**Table 3.1** ABCD matrix of common optical elements [88].

Optical Element	ABCD Matrix
Propagation through a medium having index-of-refraction $n$ and length $d$ .	$\begin{bmatrix} 1 & d/n \\ 0 & 1 \end{bmatrix}$
Refraction at a spherical boundary of radius $\mathfrak{R}$ , entering a medium of index $n_2$ from a medium of index $n_1$ . $\mathfrak{R}$ is positive if the centre of curvature lies in the positive direction of ray propagation.	$\begin{bmatrix} 1 & 0 \\ -\frac{n_2 - n_1}{n_2 \mathfrak{R}} & \frac{n_1}{n_2} \end{bmatrix}$
Transmission through a thin lens of focal length $f$ .	$\begin{bmatrix} 1 & 0 \\ -\frac{1}{f} & 1 \end{bmatrix}$
Reflection from a spherical mirror having ROC, $\mathfrak{R}$ . $\mathfrak{R}$ is positive if the centre of curvature lies in the positive direction of incident ray propagation.	$\begin{bmatrix} 1 & 0 \\ \frac{2}{\mathfrak{R}} & 1 \end{bmatrix}$

A program was written to simulate the laser beam path inside the optical cavity. The laser beam was created by combination of nine rays, one ray representing the beam centre and eight rays on the circumference. The divergence/ focusing of the beam was represented by slope of circumferential rays with respect to the centre ray. The following algorithm was used to trace the laser beam:

- (a) Initialize the beam parameters at the surface of front mirror:  $x$  and  $y$  coordinates and slopes.
- (b) Displace the beam to the first surface of lens:  $[1, (d-a-t); 0, 1]$ .
- (c) Transform beam through the lens:  $[1, 0; 0, n_1] * [1, n_1 * t; 0, 1] * [1, 0; (1-n_1)/(\mathfrak{R}_1 * n_1), 1/n_1]$   
(Refraction at flat surface, through lens of refractive index  $n_1$  and thickness  $t$ , refraction at curved surface with ROC,  $\mathfrak{R}_1$ ).
- (d) Displace the beam to the rear mirror:  $[1, a; 0, 1]$ .
- (e) Calculate reflected and transmitted beam parameters at the rear mirror: using  $[1, 0; -1/f_m, 1]$  and  $[1, 0; (1-n_m)/(\mathfrak{R}_m * n_m), 1/n_m]$ ; Calculate focusing of exiting beam to the detector.
- (f) Displace the beam to the second surface of lens:  $[1, a; 0, 1]$ .

- (g) Transform the beam through the lens:  $[1, 0; (n_1-1)/(-R_1), n_1]*[1, t; 0, 1]*[1, 0; 0, 1/n_1]$   
(Refraction at the curved surface, through lens thickness, refraction at the flat surface).
- (h) Displace the beam to the front mirror:  $[1, (d-a-t); 0, 1]$ .
- (i) Reflect the beam at the rear mirror:  $[1, 0; -1/f_m, 1]$ .
- (j) Repeat steps (b)- (i) till desired number of passes or till the re-entrant condition is reached.

From the calculated laser beam path, the properties for the optical cell were studied, which are presented in the subsequent sections.

### 3.3. SIMULATION OF LASER BEAM PATH IN THE OPTICAL CELL

Simulations of laser beam path were performed to study the feasibility of concept introduced in the Section 3.1. As a case study, an optical cell with two spherical mirrors with the ROC of 1 meter and aperture of 50.4 mm was considered. For a laser beam of diameter of 1 mm, maximum number of passes that can be fitted into the circumference without overlap is limited to 150 for this spherical cavity. In this study, distance between the mirrors was chosen such that the spot pattern becomes re-entrant after 20 round trips. This can be achieved for a cell length,  $d$  equal to 10.9 cm with  $M=3$  (using equation (3.3)). Figure 3.2 show the simulated laser beam path for the spherical optical cell. Here, the initial beam entry position was chosen for a circular pattern. If initial  $x$  co-ordinate is defined as  $x_0$  then for a circular spot pattern, the slope in  $x$  direction is given by [52]:

$$x'_0 = -\frac{2x_0}{d} \quad (3.10)$$

The  $y$  co-ordinate of beam entry point is given by:

$$y_0 = x_0 \sqrt{\frac{4f_m}{d} - 1}. \quad (3.11)$$

And the slope in y direction is zero. For the simulation study  $x_0 = 4$  mm was taken and other beam parameters were calculated as per above equations. The initial beam location is marked by a circle in Figure 3.2 (b).

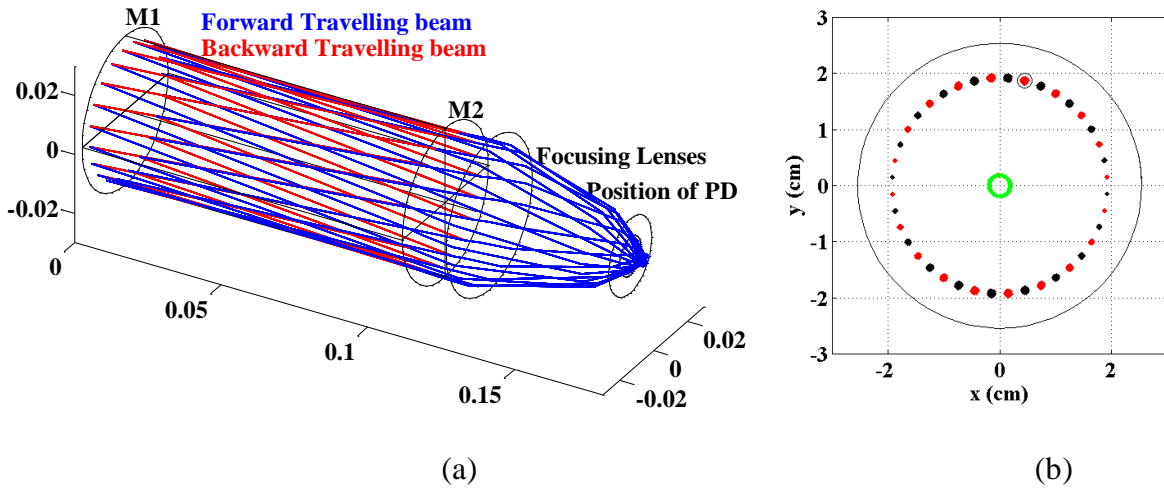


**Figure 3.2** (a) Simulated 3D laser beam path for a spherical cell of length 10.9 cm with spherical mirrors of ROC = 1 m along with focusing on photodiode (PD); (b) Laser beam spots on the front mirror (Red), rear mirror (Black) and on the photodetector (Green).

The optical cell was modified by inserting a cylindrical lens to increase the number of passes before re-entrant condition was achieved. When a cylindrical lens is inserted a dense Lissajous pattern of spots results due to the astigmatism. As a case study, a plano-convex cylindrical lens of focal length 50 cm and thickness 5 mm was used at a distance ‘a’ from the rear mirror.

To study the re-entrant condition for on axis input, the laser beam was made to enter through a hole of radius 1 mm located at the centre with a slope of 0.072 along x and y directions. The lens position, ‘a’, was varied in steps of 10  $\mu$ m. The path of the ray was traced till it exits the cavity (say after traversing  $N_r$  passes through the cavity, forming various Lissajous patterns on the mirror

surfaces). The number of round trips and exit position from the hole centre was calculated with varying lens position, ‘a’, as shown in Figure 3.3. Re-entrant pattern was observed for the lens position for which, the laser beam leaves cavity passing through the centre of the entrance hole, within an accuracy of a few microns. Although the beam centre does not coincide exactly with the entrance hole centre, these lens positions do satisfy equation (3.5). From Figure 3.3, it can be easily seen that for a fixed d, a large sets of  $(N_y, M_y)$  values exists where re-entrant condition is satisfied. Though this simulation represents a particular case of  $N_x=20$ , it is not the only possible solution. Similar, results were obtained for different cell parameters viz. d,  $f_1$ ,  $f_m$ .

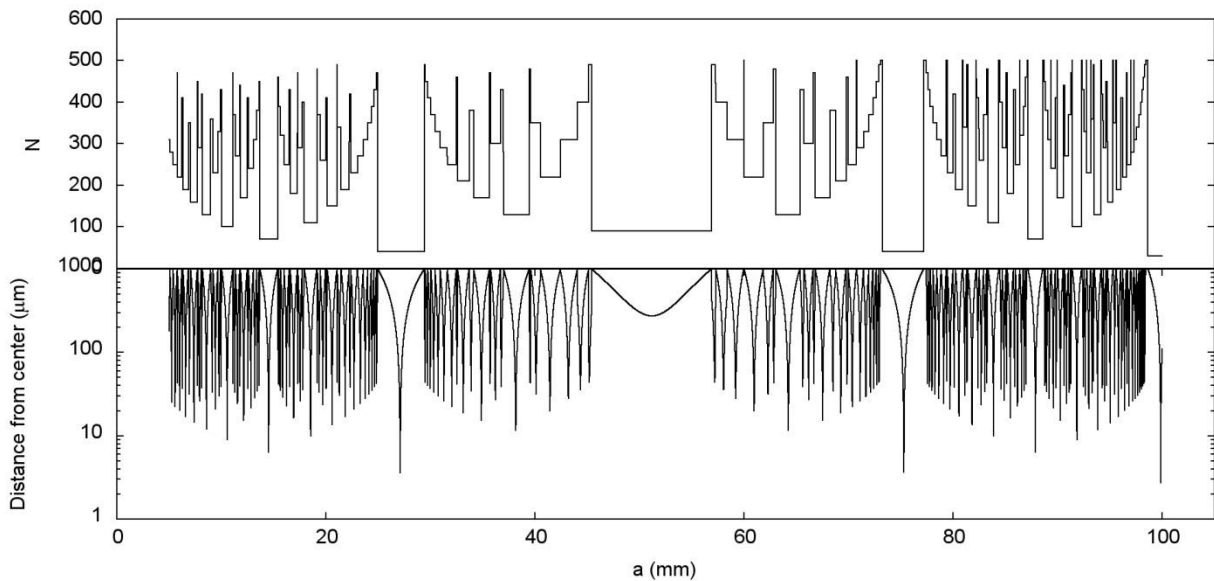


**Figure 3.3** Plot of re-entrant number  $N_r$  and distance of exit point from hole centre verses position of lens.

The simulation of re-entrant condition for off-axis input was done with initial beam position same as that for spherical optical cell stated above. It was observed that for an off-axis input, if a hole of 1 mm is used, then the circulating beam exits the cavity much before re-entrant condition is satisfied. This happens because the spacing between the spots decreases as we move away from

the centre. Accordingly, to retain the laser power inside the cavity, the hole size should be made small enough, but it also limits the entry of the laser beam. Otherwise finite transmittance of the mirror as in the case of many cavity enhanced spectroscopic techniques can be used. In this case, the number of round trips after which beam becomes re-entrant is twice of  $N_r$  for centre input, because here equation (3.3) is satisfied for  $\Theta = 2\pi$ .

Simulation study shows that for the proposed cell, re-entrant condition is satisfied with large  $N_r$ . However, owing to the shape of Lissajous pattern, there would be a finite overlap between the spots even for small  $N_r$ . It is important to estimate the overlap area of the spots, as this overlap may contribute to the noise. With progress of beam in the cell, its shape becomes elliptical due to astigmatism. Hence, the analytical formulation for calculating overlap area between the two ellipses was used for each simulated spot pattern. For this purpose, firstly all those spots were identified which lie within the range of a particular laser spot. Here, the range was defined as twice the radius of initial beam to take the divergence into account. Subsequently, relative positions of the spots were identified as described by Etayo *et al.* [89]. Depending on relative position, overlap area is calculated as detailed in [90].

Figure 3.4 (a) and (b), shows the plot of percentage overlap area versus  $N_r$  for centre input and off-axis input respectively. This figure shows that for both cases, the overlap area of the spots increases with  $N_r$ , however for some of the patterns with equal  $N_r$ , percentage overlapping area is lower than the others. Hence, it is possible to obtain very large  $N_r$  with low overlapping area by proper adjustment of lens position and/or distance between mirrors.

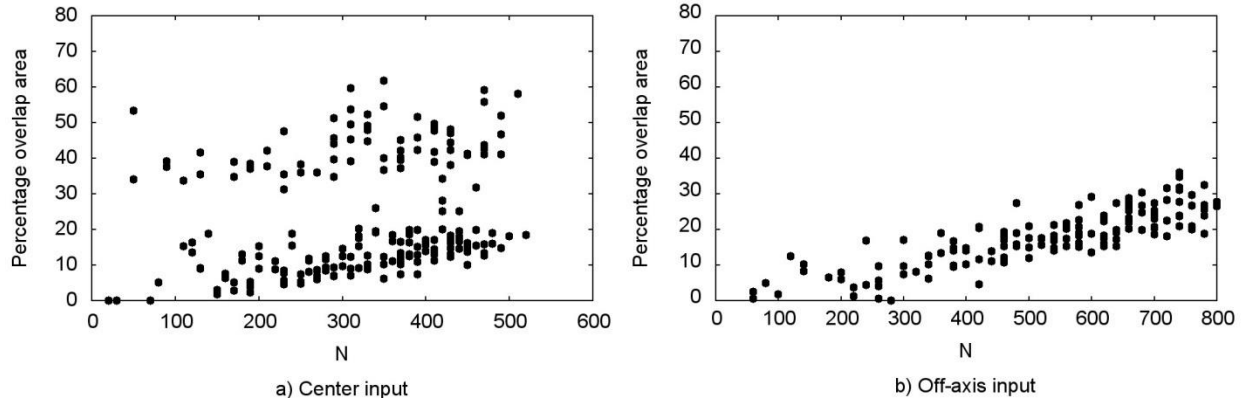


**Figure 3.4** Overlap area versus  $N_r$  for: a) Centre input; b) Off-axis input.

### 3.4. DESIGN CONSIDERATIONS

As discussed earlier, a large number of design configurations are theoretically possible. Practical configurations amongst them can be chosen based on the application. The important design parameters are discussed below:

#### 3.4.1. Important Design Parameters

##### 3.4.1.1. Coupling of Laser Power to the Cavity

The laser power can be coupled to a cavity by two methods: a) Through a hole for direct multipass absorption spectroscopy applications; b) Through partial transmittance of mirrors, for cavity based techniques [91]. In principle, for both cases, beam entry position can be located at the centre of the mirror (centre input ray) or at a location near the edge of mirror (off-axis input ray). However, when laser beam enters through a physical hole in the mirror, centre input method is appropriate. This is because, for off-axis case, the beam might exit the cavity before re-entrant condition due to closely spaced spots. Hence, centre input will give longer path length compared to off-axis input.

When the laser power is coupled through the finite transmittance of the mirrors, both solutions are feasible. Thus, in this case, the position of beam entry is governed mainly by SNR.

#### 3.4.1.2. Signal to Noise Ratio

The transmitted power from the multipass cell and the optical cavity shows interference fringes, caused by overlapping of the beams, when the laser wavelength is scanned. This wavelength-dependent transmission fringes contribute to the noise in observed absorption signal for all the multipass cell and cavity based techniques.

In multipass cell experiments, where the beam enters and exits through a hole, interference between partially overlapping spots is the main source of noise. The overlapping results in irregular fringe pattern depending on the number of passes between overlapping laser beams and the relative overlap area. Thus, for multipass cell, centre input is favoured to avoid beam exit before re-entrant condition is reached. Simulation study with centre input shows that due to the symmetry, for some configurations, the pattern of spots is retraced back. Hence, each circulating beam will have interference with another circulating beam. Such patterns are identified by a high overlap area. These configurations results in very noisy signal and hence should be avoided. All other configurations are usable and show an overlap area of less than 20% of total spot area (See Figure 3.4).

In cavity based experiments, laser power is coupled to the cavity through a finite transmittance, and this remains trapped infinity, till it decays completely. In such cases, interference between re-entrant beams gives regular interference pattern with free spectral range,  $FSR = c/(2N_r d)$  in addition to the noise discussed in the previous paragraph. However, it is possible to reduce or

completely eliminate this noise by choosing  $N_r$  high enough so that FSR is less than the laser linewidth. However, as  $N_r$  increases, the overlap between the spots also increases, thus configuration with a minimum noise is a compromise between the path length extension and overlap between the spots.

#### 3.4.1.3. Tolerance to Misalignment

Another important consideration is the tolerance to misalignment. Those patterns for which a small change in lens position can lead to a large error in exit position are generally difficult to align. Here, the tolerance is defined as a variation in lens position, for which centre position of exiting beam stays within 100  $\mu\text{m}$  of input beam centre.

### 3.4.2. Case Studies

Based on the design parameters discussed above, two designs of multipass cells are presented. First design is based on achieving a path length of at least 80 m. If 10.9 cm long cell is considered, it translates to a number of round trips greater than 366. To compensate for the volume occupied by the lens,  $N_r=380$  is chosen. In the second design, FSR less than 3 MHz is aimed to even out the fringes due to the interference amongst re-entrant beams. Hence minimum required  $N_r=460$ . In addition, overlap area between the spots should not be too high. Thus, the aim is to design a cell with maximum number of spots with overlap less than 20%. The possible configurations for both cases are shown in Table 3.2, and are compared for number of passes, overlap area and alignment tolerances for both centre and off-axis inputs.

**Table 3.2** Some of the design examples studied in this thesis. The spot patterns for selected designs marked by subscript a-f are shown in Figure 3.5 respectively.

Position of Lens 'a' (mm)	Centre Input			Off-Axis Input				
	$N_r$	Overlap Area %	Tolerance ( $\mu\text{m}$ )	$N_r$	$N_y$	$M_y$	Overlap Area %	Tolerance ( $\mu\text{m}$ )
<b>7.640</b>	380	24.3	29	760	152	4	29.4	16
<b>18.313</b>	380 <sup>a</sup>	24.5	37	760	152	4	26.2	21
<b>84.087</b>	380	18.5	30	760	760	4	20.7	17
<b>94.760</b>	380	19.3	19	760	152	4	20.8	11
<b>103.314</b>	380 <sup>b</sup>	15.7	18	760	760	4	20.0	9
<b>12.610</b>	190	42.0	67	380	380	4	16.6	36
<b>25.227</b>	190	8.2	95	380 <sup>d</sup>	190	4	14.1	51
<b>77.173</b>	190	6.6	83	380	190	4	14.8	42
<b>89.790</b>	190	36.5	51	380 <sup>e</sup>	380	4	9.4	28
<b>99.225</b>	190	4.2	40	380	95	4	9.9	22
<b>91.901</b>	390	50	23	780 <sup>f</sup>	780	4	18.6	12
<b>93.029</b>	470 <sup>c</sup>	18.1	18	940	235	4	25.6	9

(a) Design with Required Number of Round Trips,  $N_r=380$

In the case of input beam at the centre,  $N_r = 380$  is attained for five lens positions from rear mirror, viz.  $a = 7.640, 18.313, 84.087, 94.760, 103.314$  mm. Amongst them  $a = 103.314$  mm results in a minimum overlap while maximum tolerance is attained for  $a = 18.313$  mm. In the case of 'off axis input' with  $N_r=380$ , possible lens positions from rear mirror are  $a = 12.610, 25.227, 77.173, 89.790, 99.225$  mm, with minimum overlap for  $a = 89.79$  mm and maximum tolerance for  $a = 25.227$  mm.

From Table 3.2, it is clear that off-axis input gives lower overlap and better tolerance compared to the centre input case; hence it is preferred when light is coupled to the cavity through the transmittance of mirrors. For direct absorption, centre input hole is mandatory and the patterns with higher tolerance are preferred for easy alignment of the detectors.

(b) Design for Maximum Number of Round Trips with Overlap Area Less Than 20 %

From Figure 3.4, one can obtain large number of passes with an overlap area less than 20% for many lens positions. At the same time, alignment tolerance should be high enough for practical alignment. Taking this into account, the maximum number of spots with overlap area less than 20 % is 470 for centre input and 780 for off-axis case.

The design parameters for both designs as discussed in (a) and (b) above are listed in Table 3.2. Some of the selected designs with large re-entrant condition are marked by superscript (a)-(f). Figure 3.5 (a)-(c) shows the simulated spot pattern for centre input with re-entrant number 380, 380 and 470 respectively. Figure 3.5 (d)-(f) shows the simulated spot pattern for off-axis input with re-entrant number 380, 380 and 780 respectively. For all these designs, overlap area is less than 20% and lens position tolerance more than 18  $\mu\text{m}$ .

### **3.5. DESIGN OF OPTICAL CAVITY FOR TRACE HDO DETECTION SYSTEM**

The optical cavity for trace gas detection using OA-ICOS technique was designed using astigmatic end mirrors. Since tracing exact beam path is not critical for optical cavity, the alignment tolerances of optical cavity are more relaxed. The selection of mirrors of the optical cavity was based on achieving effective path length of more than 200 m with a small cell of length 10 cm,

implying reflectivity more than 99.95% at selected wavelength 1390.6 nm ( $=7191 \text{ cm}^{-1}$ ). In order to minimize the cavity mode noise, mirrors with 50.4 mm aperture were chosen so that large re-entrant condition with minimum overlap can be achieved, based on simulation of optical cavity. The design of optical cell for mounting these mirrors is discussed in the next chapter (Section 4.4).

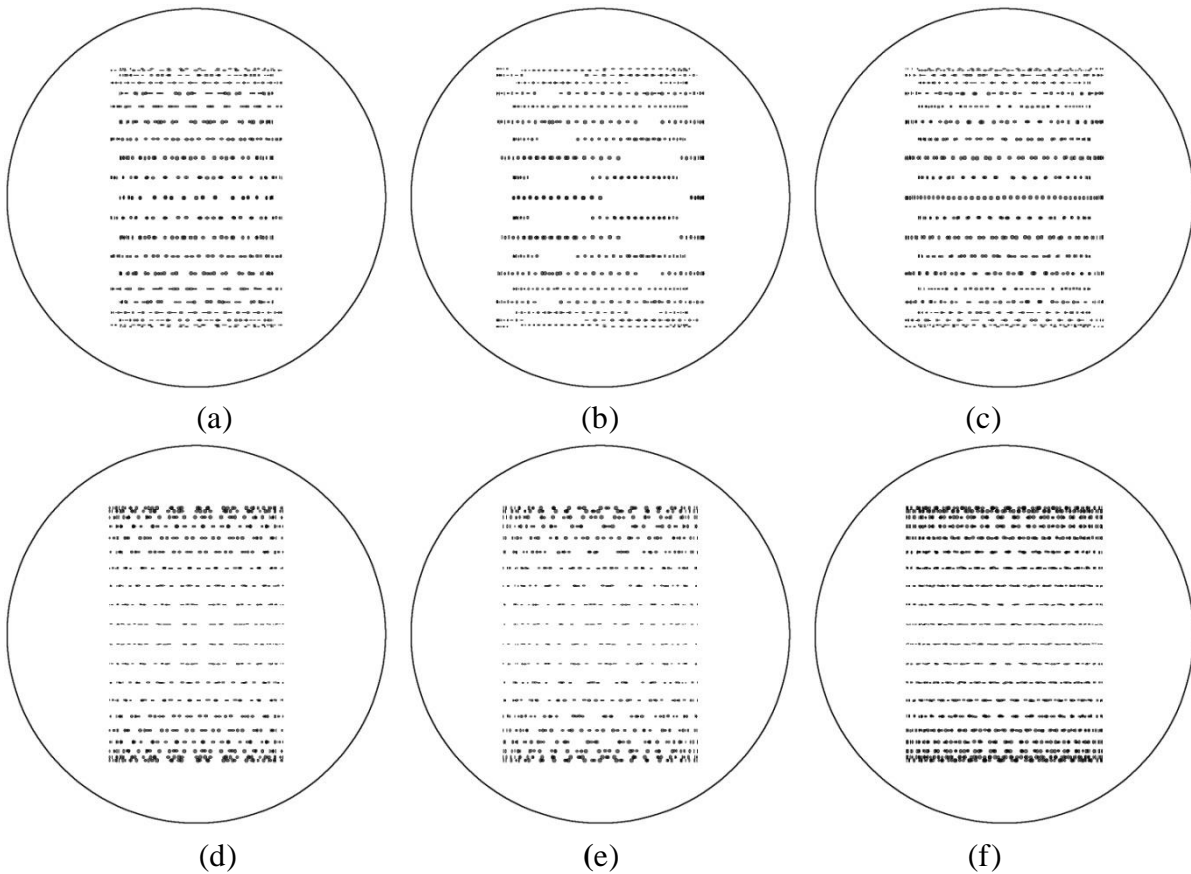


**Figure 3.5** Observed spot patterns of selected design examples with parameters as given in Table 3.2. (a)-(c) Shows the simulated spot pattern for centre input with  $N_r = 380, 380$  and  $470$  respectively; (d)-(f) Shows the simulated spot pattern for off-axis input with  $N_r = 380, 380$  and  $780$  respectively.

### **3.6. SUMMARY**

A new variant of multipass cell design with spherical end mirrors and a cylindrical lens placed close to the rear mirror was presented. Introduction of astigmatism in the cavity due to cylindrical lens results in a dense pass beam pattern on mirror surface. This increases total path length in the cavity for the laser to the medium interaction in the cell. A study of this design based on the simulation of laser beam path by optical ray tracing in the cavity is presented. The number of passes and beam spot patterns with respect to the position of cylindrical lens was examined. A large set of solutions have been found that satisfies re-entrant condition in the cell. As such cells have additional losses introduced by the additional lens, hence are less preferable in optical cavity design. To the contrary such cells can be effectively utilized for spectroscopic studies using a multi-pass cell design where precise alignment is required.

## CHAPTER 4

### **DESIGN AND IMPLEMENTATION OF OA-ICOS SYSTEM FOR TRACE HEAVY WATER DETECTION**

---

Various aspects of LAS and optical cavities have been discussed in CHAPTER 2. For the measurement of heavy water concentration, an OA-ICOS technique based system has been implemented. The choice of various components used in the system has major impact on its performance. In this chapter, design aspects of the developed system are discussed. The photograph of the developed system is shown in Figure 4.1 and the block diagram and the optical layout of the developed OA-ICOS system is shown in Figure 4.2. The system consists of an IR laser source, an optical cavity, alignment optics, photodetectors and an electronics system for the control and data acquisition. The laser beam emitted by the IR laser source is collimated, and this collimated laser beam is split into two parts using a pellicle beam splitter with 8:92 splitting ratio. The major portion is aligned to the optical cavity (alignment process is described in Section 4.4.3). The smaller portion of the laser beam is focused on the photodiode PD1 to monitor the laser power variation. The integrated cavity output leaking through the rear mirror is focused on the photodiode, PD2. The outputs of the photodetectors are digitized and processed by the data acquisition system. The component selection and important specifications of the various components are discussed in this chapter. Before specifying other components, it was important to select the absorption peak, which is presented in the next section.

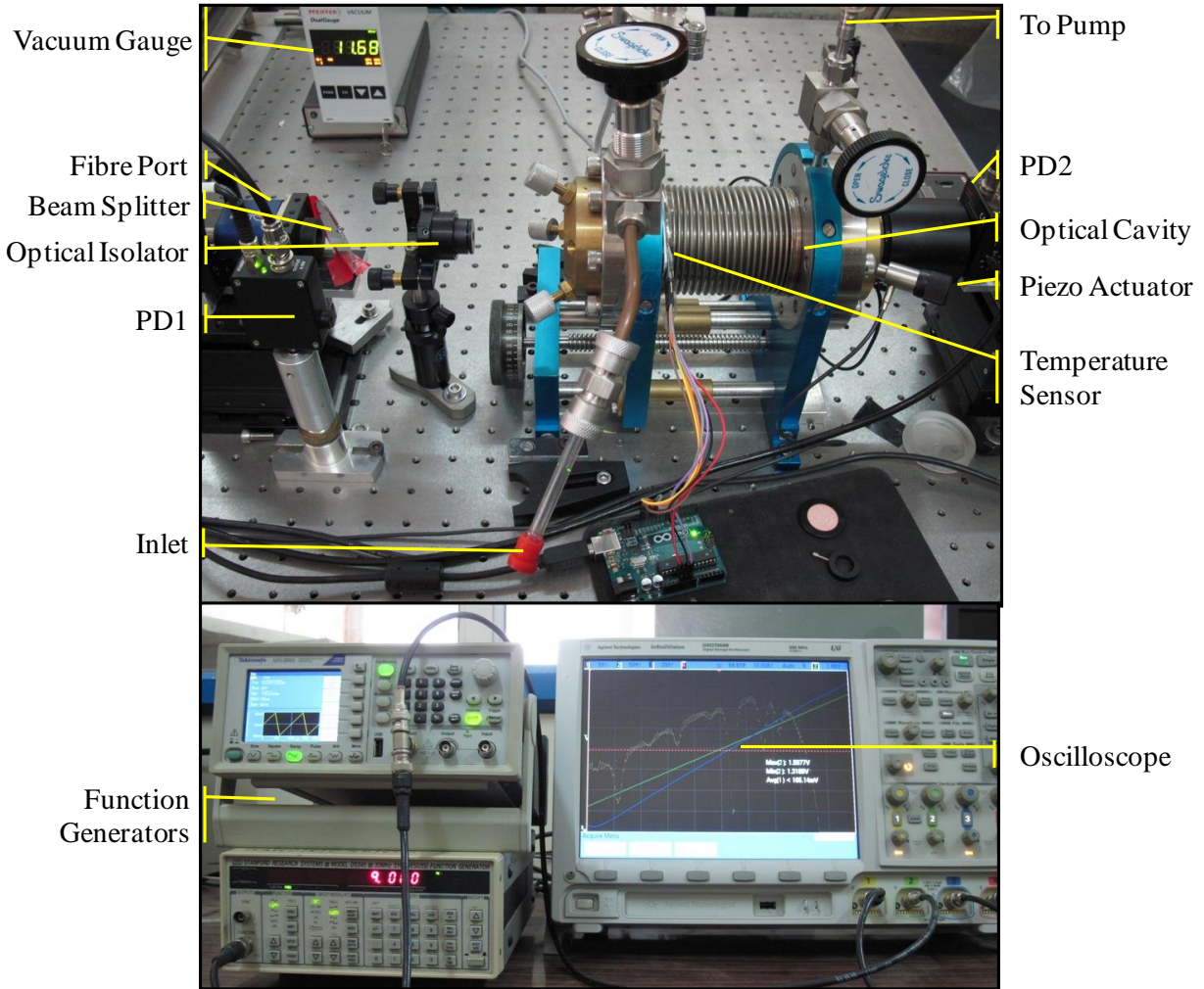


**Figure 4.1** Photograph of the developed HDO detection system.

#### 4.1. SELECTION OF ABSORPTION PEAKS

The performance characteristics of a spectroscopic system depend on the selection of suitable absorption peaks for the measurement. The important considerations for the selection of a suitable absorption peak for determination of the concentration of a molecule are:

- (a) It should have sufficient line-strength, so that absorption signal can be easily distinguished from the noise.

- (b) The peak should be isolated and free from the interference from other gases.
- (c) For isotopic ratio determination, the line-strength of different isotopes should not be too different. The selected peaks should be free from the interference from other isotopes.
- (d) In addition, a suitable laser source and detector should be easily available.

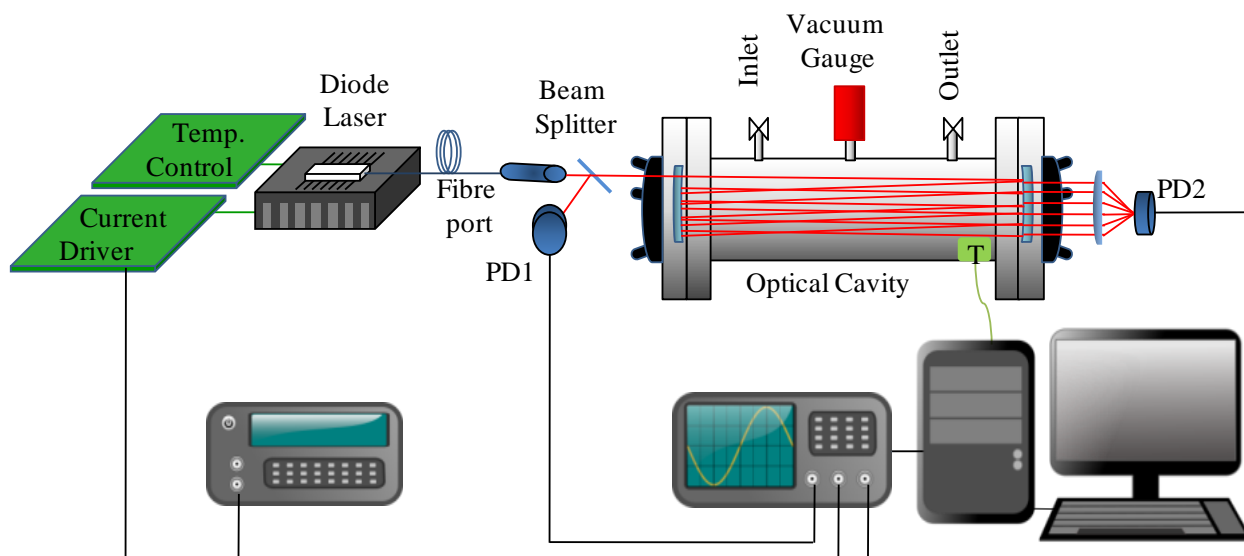


**Figure 4.2** The block diagram and optical layout of the developed OA-ICOS system. The main of the system are OEM diode laser, optical cavity, optical componets, detectors, oscilloscope for data acquisition and computer for sihnal processing.

Since the strength of absorption peaks are high in the mid-infrared “fingerprint” region from 3  $\mu\text{m}$  to 25  $\mu\text{m}$ , the trace gas sensing in this region yields highest sensitivity. However, the lead salt CW diode lasers operating at mid-infrared wavelengths require cryogenic cooling. Hence, these lasers are not suitable for the development of portable equipment. From past few decades, compact, CW semiconductor diode lasers, which are primarily developed for communications, are readily available from the commercial sources [17, 97]. These lasers operate at room temperature. The

reliability, power, and wavelength coverage of these lasers is steadily improving, while the cost is decreasing. They are mass produced for commercial application, mainly in three bands viz. 800, 1300 and 1500 nm. The laser at 1300 and 1500 nm, are based on quaternary InGaAsP semiconductors and those in the 750-890 nm region are based on AlGaAs. These lasers typically produce output powers of 5-15 mW with single-mode emission using distributed feedback technology. They provide high modulation frequencies; continuous wavelength tuning and have lifetime in excess of 10 years. These lasers can be used to access the molecular overtone and combinational transitions. These transitions are typically, 30 to 300 times weaker than the fundamental transitions in the mid-IR region. However, very high sensitivity can still be achieved owing to the higher stability of diode laser in near IR region compared to lead salt laser available in mid IR region.

In this thesis, heavy water leaks on PHWR are monitored by measuring HDO concentration, because the leaked heavy water is immediately converted to HDO, due to the following equilibrium reaction with moisture in the surrounding air:



For low D/H ratio, most of the deuterium exists in form of HDO and the remaining concentration of D<sub>2</sub>O is orders of magnitude lower than HDO. Hence, the heavy water concentration is determined by measuring the [HDO]. Like H<sub>2</sub><sup>16</sup>O, the HDO molecule also has a large number of absorption peaks from near-infrared region to far infrared region as shown in Figure 2.4 . As can be seen, the absorption spectrum appears as number of bands and the HDO peaks with lower intensity coexist with H<sub>2</sub><sup>16</sup>O peaks of much higher intensity.

Amongst the various water absorption bands, the  $\Psi$  band can be easily covered by 1300 nm band of commercially available diode lasers. Thus, the absorption peaks in this band find application in moisture sensing due to the availability of low-cost diode lasers. A stick plot of absorption peaks in  $\Psi$  band is shown in Figure 4.3. This band arises due to the harmonic transition (2,0,0), (0,5,0) and (0,0,2) as well as combinational transition (1,2,0), (0,2,1) and (1,0,1). Although there are a large number of absorption peaks for HDO, all of them are not suitable for concentration determination. This is mainly due to the interference from strong absorption peaks of other isotopologues ( $\text{H}_2^{16}\text{O}$ ,  $\text{H}_2^{18}\text{O}$ ,  $\text{H}_2^{17}\text{O}$ ). The absorption peaks in the  $\Psi$  band were explored for the suitability for [HDO] measurement. Some of these are listed in Table 4.1. Amongst various listed peaks, the HDO absorption peaks at  $7191.04\text{ cm}^{-1}$  ( $=1390.619\text{ nm}$ ) and  $7183.97\text{ cm}^{-1}$  ( $=1391.987\text{ nm}$ ) were studied further. The selected peaks are marked in bold letters in the Table 4.1. The plot of recorded spectrum for the selected regions, for a deuterium enriched water sample is shown in Figure 4.4. From the plot it is clear, that the absorption peak at  $7191.04\text{ cm}^{-1}$  has higher line strength but the peaks are not well separated which may lead to error in the computation of concentration. Since the absorption peak at  $7183.97\text{ cm}^{-1}$  is well separated, fitting error was expected to be less. Nevertheless, if the overlapping of absorption peaks is properly modelled, better sensitivity can be achieved with stronger peak (i.e. the HDO absorption peak at  $7191.04\text{ cm}^{-1}$ ). Thus, this peak was selected for the further studies and the spectrum fitting algorithm was developed to take this in to consideration as detailed in Section 5.2. Figure 4.5 shows the stick plot at  $7191.04\text{ cm}^{-1}$  along with other nearby peaks.

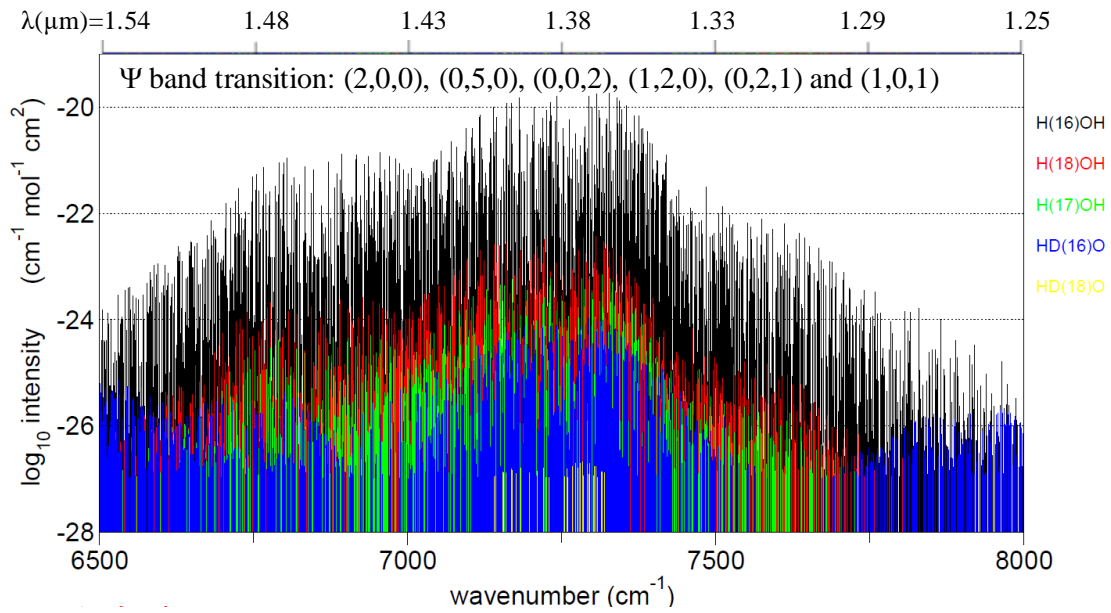


**Figure 4.3** Stick plot of  $\Psi$  band of water absorption peaks [96].

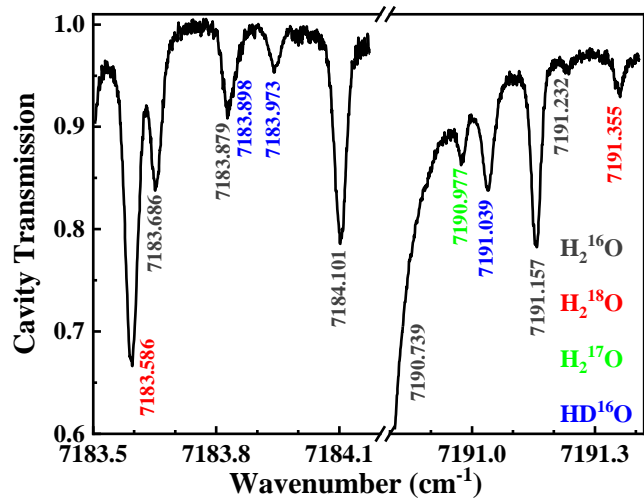


**Figure 4.4** Observed water spectrum around 7183.97 and 7191.04  $\text{cm}^{-1}$  HDO absorption peaks with assigned wavenumbers for water sample.

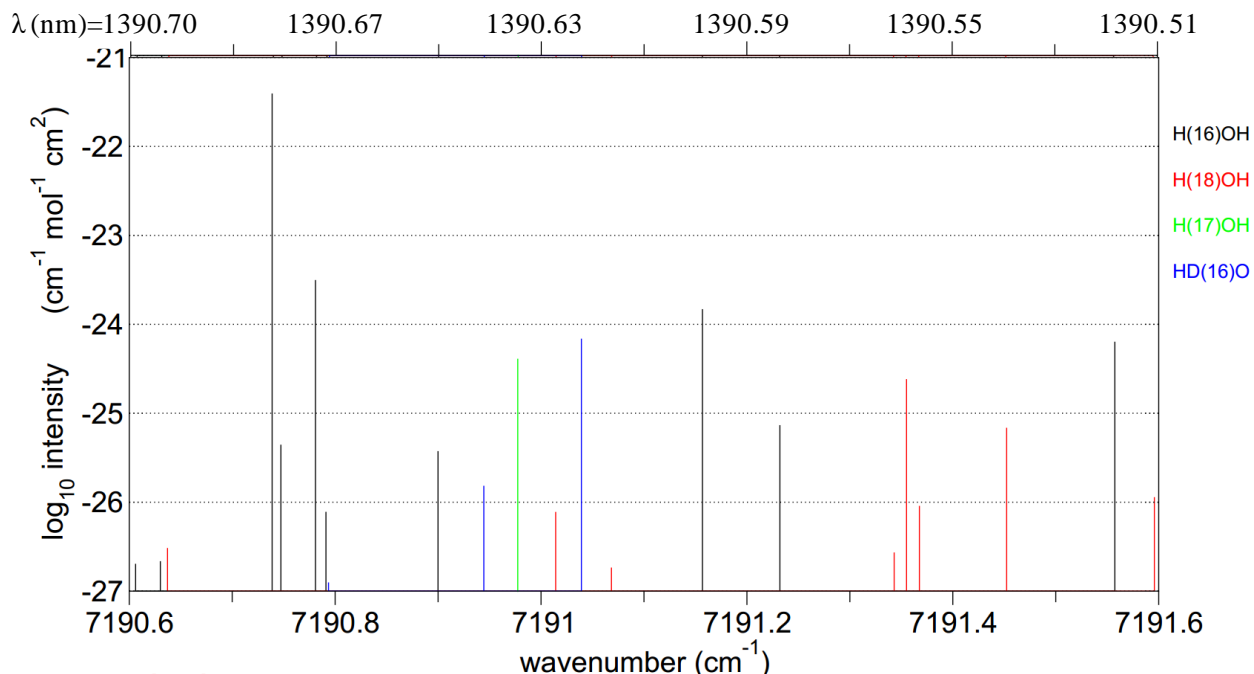


**Figure 4.5** Stick plot of absorption peaks used in the developed system [96].

**Table 4.1** Table showing HDO absorption peaks and their suitability for concentration determination. The peaks are listed in decreasing order of HDO line-strength.

	HDO Peak Position (cm <sup>-1</sup> )	HDO Peak Position (nm)	HDO Line-strength (cm <sup>-1</sup> /molecule/cm <sup>2</sup> )	Nearest H <sub>2</sub> O Peak Position (cm <sup>-1</sup> )	Nearest H <sub>2</sub> O Line-strength (cm <sup>-1</sup> /molecule/cm <sup>2</sup> )	Suitability
1	7190.28	1390.766	8.88E-25	7190.28	2.41E-22	Merged with strong H <sub>2</sub> O peak
2	<b>7191.04</b>	<b>1390.619</b>	<b>8.15E-25</b>	<b>7191.16</b>	<b>1.52E-24</b>	<b>Suitable</b>
3	7175.83	1393.567	7.86E-25	7175.88	6.31E-25	Peak too close
4	7197.95	1389.284	7.34E-25	7197.55 7198.54	5.62E-24 1.04E-25	H <sub>2</sub> O Peaks too far
5	7181.30	1392.506	6.33E-25	7181.31	3.90E-25	Not resolvable
6	7179.99	1392.76	4.92E-25	7180.32	3.73E-25	Suitable
7	<b>7183.97</b>	<b>1391.988</b>	<b>3.95E-25</b>	<b>7184.10</b>	<b>1.49E-24</b>	<b>Suitable</b>

## **4.2. LASER SYSTEM: ALIGNMENT OF LASER AND IR SOURCE AT 1390 NM**

Two lasers were used in the HDO detection system developed in this thesis. A He-Ne laser in the visible region for the alignment and a near IR diode laser with centre wavelength of 1390 nm as a source for the absorption measurement. The important characteristics for both lasers are presented in this section.

### **4.2.1. He-Ne Laser for Alignment**

For the optical alignment of various components, a laser in the visible region is required. For this purpose, a He-Ne laser lasing at 632.8 nm (red light) with optical power of 3 mW and beam size of 1 mm was used.

### **4.2.2. NIR Laser Source with Centre Wavelength at 1.39 $\mu\text{m}$ (7191 $\text{cm}^{-1}$ )**

The selected HDO absorption peak at 7191.04  $\text{cm}^{-1}$  (1390.619 nm) can be accessed using a laser lasing at 1390.5 nm. A tunable discrete mode (DM) diode laser EP-1390-5-B in a 14-pin butterfly package manufactured by M/s. Eblana Photonics was selected. This laser was mounted on a butterfly laser diode mount, LM14S2 (Thorlabs), with type 2 configuration card. The current of the laser diode was controlled by a 500 mA laser driver IP500. This OEM unit can be used to modulate the laser diode current using an external signal on analog modulation input, at frequencies up to 50 kHz. As the wavelength of a DM diode laser is extremely sensitive to its temperature, for a stable operation, it is necessary to maintain a constant temperature. This was achieved by using TCM1000T 3W TEC Controller from Thorlabs. This Module regulates current through the integrated Thermal Electric Cooler (TEC) while maintaining a constant temperature

of a device, using a feedback from the internal 10 k $\Omega$  NTC thermistor. The most important specifications of diode laser are listed in Table 4.2.

**Table 4.2** The important specifications of DM diode laser, EP1390-5-DM-B01-FA (14 pin butterfly package).

Parameter	Typical Value
<b>Laser Power</b>	18 mW
<b>Max Current</b>	120 mA
<b>Slope Efficiency</b>	0.18 mW/mA
<b>Threshold Current</b>	11.49 mA
<b>Wavelength Temperature Tuning Coefficient</b>	0.1 nm/K
<b>Wavelength Current Tuning Coefficient</b>	0.014 nm/mA
<b>Linewidth</b>	2 MHz

The DM laser diode was integrated with the driving modules. The slope efficiency and wavelength current tuning coefficient of the laser were measured experimentally. For these measurements, a ramp voltage was applied to the analog modulation input of the laser current driver IP500. The resulting laser power variation with the analog modulation voltage is shown in Figure 4.6. The plot also shows linear variation in the laser power with modulation voltage  $V_{\text{analog}}$ . The small dips in the intensity are due to the presence of strong water absorption peaks. The observed threshold voltage was 0.25 V, which is equivalent to the measured threshold current of 12.5 mA.

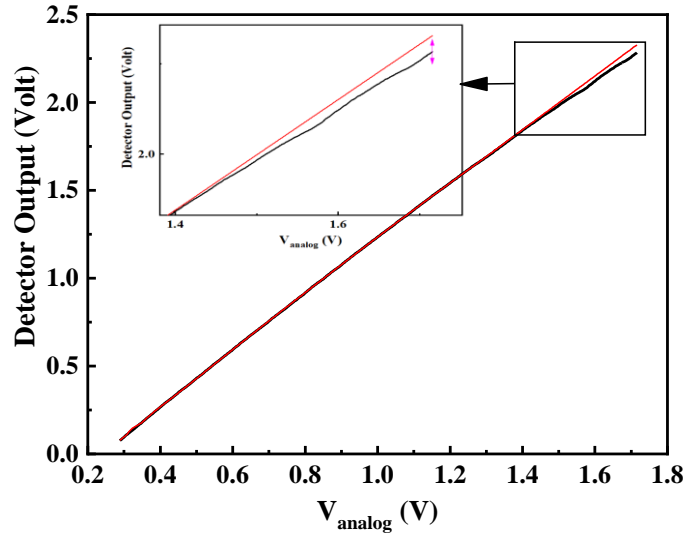


**Figure 4.6** Plot of laser output power with analog modulation voltage ( $V_{\text{analog}}$ ) for DM diode laser EP1390-5-DM-B01-FA. The zoomed region is shown in inset.

For the calibration of wavelength with analog voltage, the spectrum of water vapour was recorded. The observed spectral peaks were compared with the peak position database available on HITRAN. The wavelength was assigned to each observed peak by comparing it with the database. The recorded spectrum and the plot of assigned wavelength with the analog voltage are shown in Figure 4.7. The plot shows deviation from ideally expected linear curve. The deviation from linearity is inherent to laser diode used. Hence, to account for non-linearity, the wavelength curve with analog voltage was fitted to a quadratic equation (one-degree higher polynomial). The fitted curve is represented by the following equation:

$$\lambda = a + bV_{\text{analog}} + cV_{\text{analog}}^2 \quad (4.2)$$

$$\lambda = 1390.1315 - 0.0355 V_{\text{analog}} + 0.24062 V_{\text{analog}}^2$$

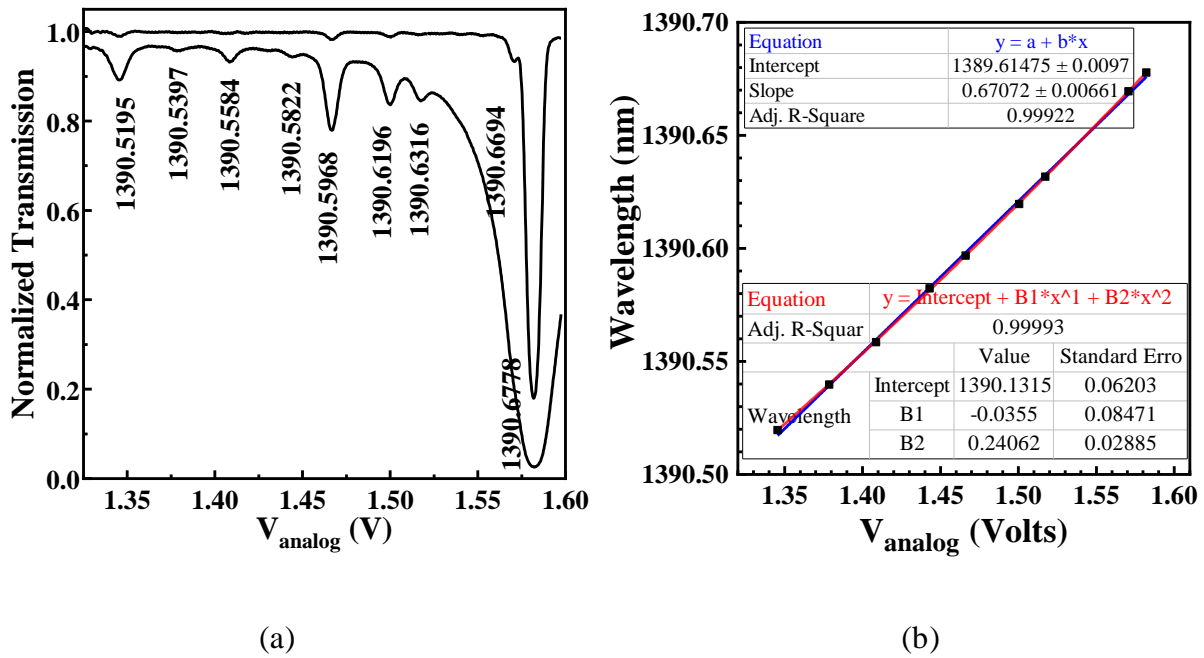


**Figure 4.7** The variation of laser wavelength for diode laser EP1390-5-DM-B01-FA with analog modulation voltage on laser current driver IP500. (a) Shows the spectrum recorded at two different pressures and the wavelengths (in nm) assigned to the absorptions peaks. (b) Plot of assigned wavelength versus the analog voltage with the linear and second order polynomial fit. 2<sup>nd</sup> polynomial shows better fit to assigned wavelength.

### 4.3. PHOTODETECTORS FOR SENSING CAVITY OUTPUT

For the wavelength around 1390 nm, Ge and InGaAs photodiodes and photoconductors are the most suitable photodetectors. However, due to the temperature sensitivity of photo-conductors, they cannot be used for CW applications. Both Ge and InGaAs photodiodes provide similar performance for CW as well as pulsed applications. Hence a germanium photodiode, PDA50B from Thorlabs Inc., with sensor diameter of 5 mm was selected. It includes a reverse-biased PIN

photo diode and an inbuilt switchable gain transimpedance amplifier. Its operating wavelength range is 800- 1800 nm and the photodiode have responsivity of 0.75 A/W at 1390 nm.

#### **4.4. OPTICAL CAVITY FOR OA-ICOS EXPERIMENTAL SYSTEM**

The optical cavity consists of high reflectivity mirrors mounted on the end flanges of a vacuum cell. The vacuum cell design and alignment of the optical cavity are presented in this section.

##### **4.4.1. Specifications of High Reflectivity Mirrors for the Optical Cavity**

The basis of high reflectivity mirrors selection has been discussed in Section 3.5. The mirrors suitable for cavity enhanced spectroscopy are available from a few manufactures such as New Port and CRD optics Inc. Amongst the commercially available mirrors; mirrors with 99.98% reflectivity at the appropriate wavelength from CRD optics Inc. were selected. The manufacture's specifications of the selected mirrors are given in Table 4.3. A cell of 10 cm length was expected to yield more than the required path length.

##### **4.4.2. Vacuum Cell Design for the Optical Cavity**

The vacuum cell for mounting the mirrors forming the optical cavity was designed and fabricated in-house. Figure 4.8 shows a 3D drawing of the designed vacuum cell. The body of the cell is made using compressible bellows with 63CF end flanges. One of the end flanges is fixed on a mount while other end flange is movable. The to and fro motion of the flange can be controlled by a threaded screw of 25 mm diameter with pitch of 3mm. To maintain parallelism between the mirrors while adjusting the cavity length, its motion is guided by three rails. The parallelism can

be maintained for small adjustments in cell length. However, when the cell length is varied by more than 1 cm fine adjustment in mirror tilt screws is required to make the mirrors parallel again. The length of the cavity can be varied from 10 cm to 18 cm. The cell length used in the experiments was 13.5 cm (for water samples) and 14.5 cm (for air samples). Larger cell length for air samples is required to achieve better sensitivity, since absolute water content in air is only about 1 to 3% of air pressure. Due to path length enhancement by optical cavity, 1 cm change in cell length, results in 12.5 m increase in effective path length.

**Table 4.3** Manufacturer’s specification of high reflectivity mirrors used in the developed system.

S. No.	Parameter	Specified Value
1	Reflectivity	99.98% at 1390 nm
2	ROC	1 meter
3	Aperture	50 mm
4	Transmittance	30 to 50 ppm

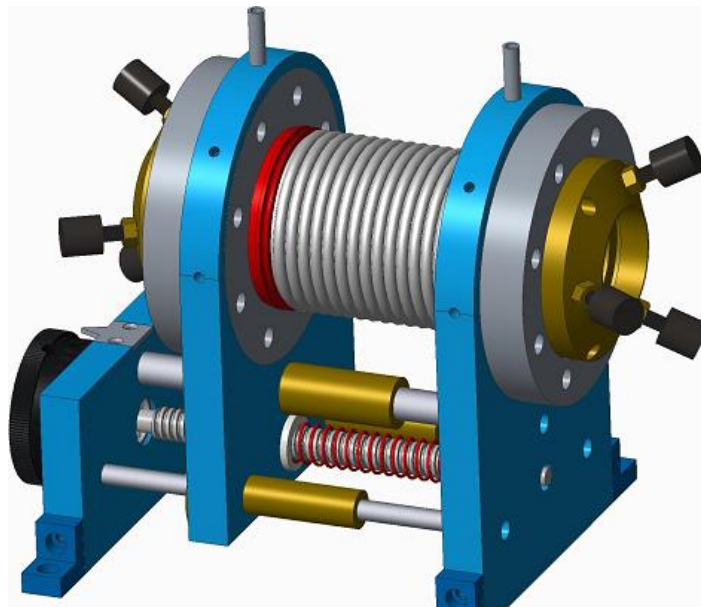


**Figure 4.8** 3D drawing of the designed assembly for the optical cavity.

The ends of the cell are sealed with a set 63CF flanges on which high reflectivity mirrors are mounted. The mirrors sit on the silicon o-ring placed in the grooves on the flanges. They are held in place by three alignment screws pressing the brass ring holding the mirrors from the other side. These screws allow centring and precise tilting of mirrors for achieving parallelism.

#### **4.4.3. Alignment of the Optical Cavity**

The alignment of the optical cavity was most critical part in the implementation of OA-ICOS techniques. The steps involved in the cavity alignment are detailed below:

##### **4.4.3.1. Alignment of Mirrors of the Optical Cavity Using a He-Ne Laser**

The first step in the alignment was positioning the mirrors such that they are perfectly parallel to each other. The procedure to achieve this alignment is shown in Figure 4.9.

- (a) The rear mirror was centred and was aligned perpendicular to the optical axis of the cavity. In this position, reflections from both surfaces are superimposed forming concentric circles. Next, the laser beam was aligned to the axis of cavity. The orthogonality of mirror with optical axis was ensured by passing the laser beam through an iris and making the reflected beam pass back through it (Figure 4.9 (a)).
- (b) The front mirror was placed and aligned in the similar way. At this point, a large number of spots were visible in the transmitted pattern (Figure 4.9 (b)).
- (c) After fine tuning the mirror and laser direction, multiple reflections on the front and back of the two mirrors overlapped. Thus, a single spot in transmitted and reflected beam pattern

ensured that mirrors were parallel to each other and laser beam was aligned to the optical axis of the cavity (Figure 4.9 (c)).

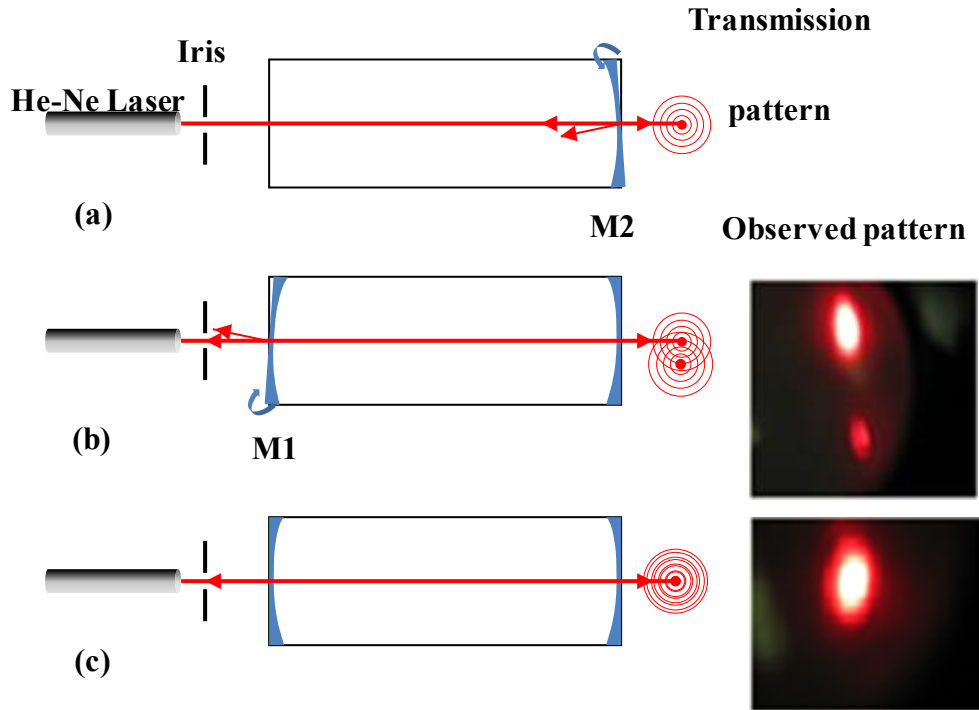


**Figure 4.9** Steps to align the mirrors parallel. (a) Alignment of rear mirror, M2; (b) Alignment of front mirror, M1; and (c) Fine tuning of both mirrors and laser beam.

#### 4.4.3.2. Coupling of IR Laser to the Optical Cavity

Once the mirrors were aligned, next task was to couple the near IR laser source to the cavity. The DM diode laser used in the system was a fibre coupled laser (pig tailed); hence the output laser beam was highly divergent. The output beam of the diode laser was made parallel by a collimator (Toptica Photonics). The optical collimator was aligned parallel to the principal axis of the optical cavity with He-Ne laser coupled to it. The setup used is shown in Figure 4.10 (a). The collimator

was mounted on a kinematic mount placed over xyz translation stage. This arrangement provides all the required degrees of freedom for accurate positioning of laser beam with respect to the cavity. After the alignment of the collimator, the IR laser was connected to it as shown in Figure 4.10 (b). Here an optical isolator was inserted because the IR laser is sensitive to optical feedback. Initially, the laser beam was aligned parallel to the axis of the optical cavity. The transmission signal showed that few lower order modes were excited along with  $TEM_{00}$ . This was expected as mode matching to  $TEM_{00}$  mode was not performed.

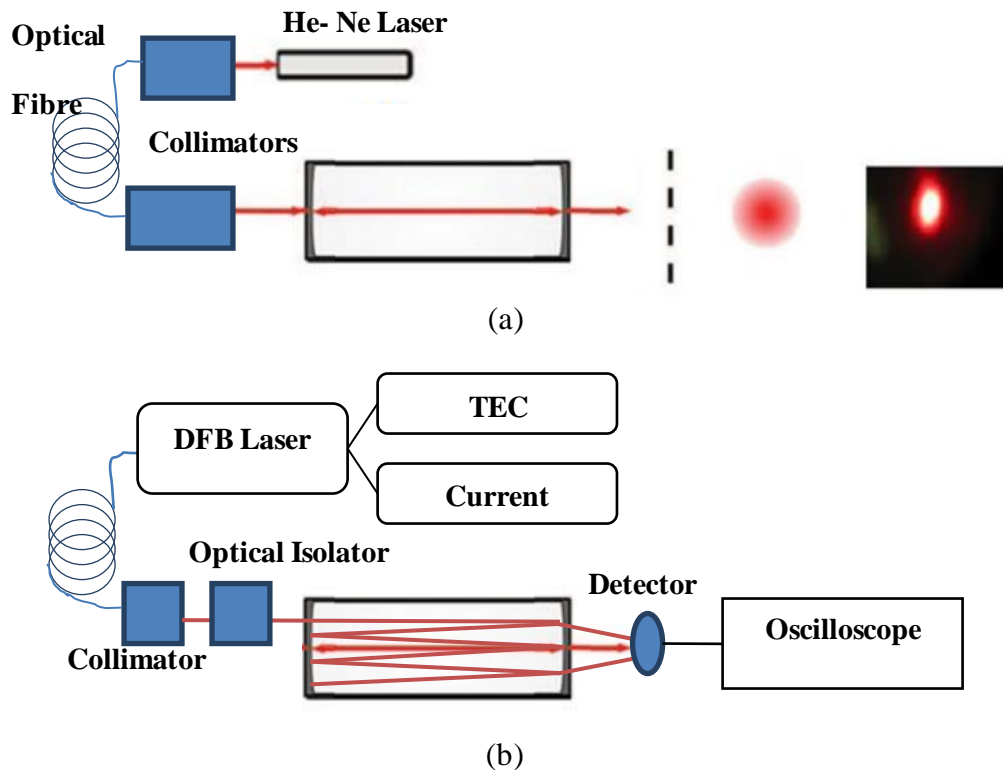


**Figure 4.10** (a) Setup for the alignment of collimator to the axis of optical cavity, (b) Setup for coupling the IR laser to the optical cavity.

The laser beam was then moved to an off-axis position. The coupling efficiency of the laser to the cavity depends on the mode matching between the laser and the optical cavity. Hence the position of laser beam and its direction were optimized. The maximum coupling efficiency was achieved

at the optimized laser beam position of  $x=10.77$  mm,  $y=9.15$  mm and  $\theta_x=\theta_y=0.9^\circ$ . Figure 4.11 (a) shows the transmitted intensity at various positions of laser beam with respect to the centre of the front cavity mirror, for a constant laser power. Figure 4.11 (b) shows the variation of transmitted intensity with  $V_{\text{analog}}$  for two different alignments of input laser beam. Finally, the alignment procedure required fine tuning of the laser beam direction and position, to minimise the optical fringes in the system. For fringe minimization, the collimator was moved horizontally to another off-axis position and y angle was tilted such that the laser spots are distributed over maximum area of the mirror.

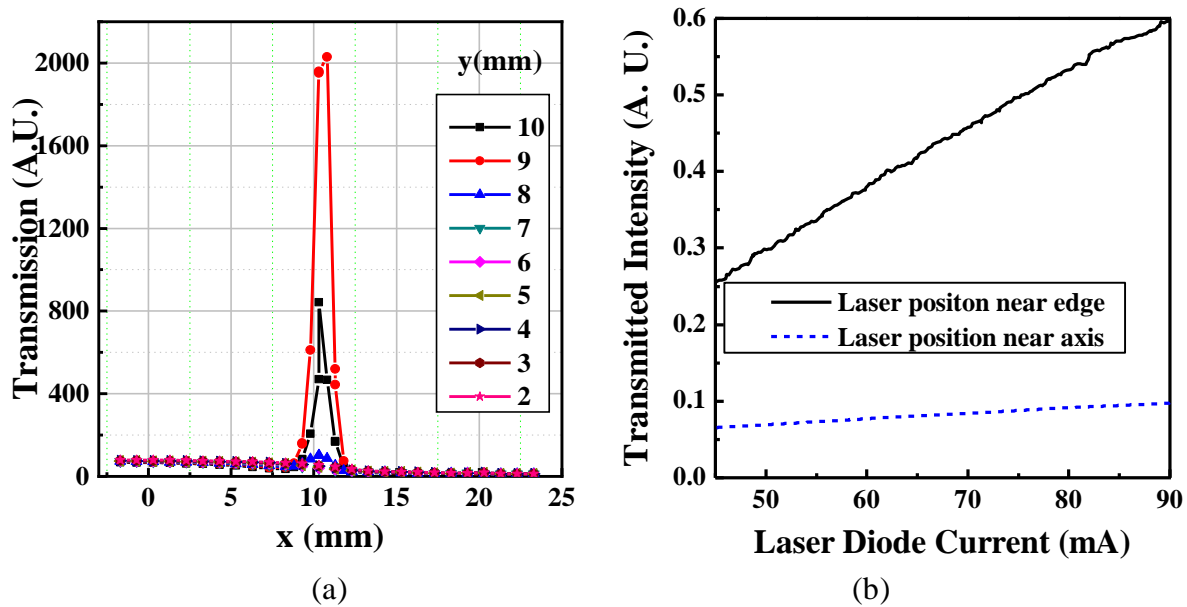


**Figure 4.11** (a) Optimization of coupling of laser power to the optical cavity; (b) The variation of transmitted intensity for two different alignments of input laser beam.

#### 4.4.4. Piezoelectric Actuator for Cavity Length Dithering

As will be discussed later in Section 5.1.2.2, the effect of residual cavity modes leads to the appearance of fringes in the transmitted baseline. The optical fringes limit the sensitivity of the

system. One method to remove the effect of these fringes is cavity length dithering. For cavity length dithering, the tilt adjustment screws on one of the mirror mounts can be replaced with piezoelectric actuators, PE4 (Thorlabs). These actuators provide 4 mm of manual coarse travel via a 0.010" pitch leadscrew, which allows coarse tilt adjustment of the mirrors. The 15  $\mu\text{m}$  open-loop piezo travel controlled by 150 V internal piezo stack, can be used for cavity length dithering. The actuator is driven by TPZ001 Piezo Driver (Thorlabs). With the internal capacitance of PE4 of 1.4  $\mu\text{F}$ , the operating bandwidth of the actuator is 30 Hz.

#### **4.5. VACUUMSYSTEM**

The isotopic ratio measurement for water must be performed at a pressure much lower than the atmospheric pressure, i.e. under the vacuum condition. The requirement of lower pressure (vacuum) arises from broadening of the absorption peaks due to pressure broadening. The effect of broadening is merging of peaks; the effect is more serious in case of water absorption in near IR region, due to closely spaced peaks owing to complex absorption spectra. The effect of pressure broadening is shown in Figure 4.12. The figure shows that the width of the absorption peaks increases with increasing pressure as per equation (2.23). Since the fraction of water in air is constant, the total content of water increases hence height of the peak also increases. For low pressures, the height to width ratio of the peaks increases with increasing pressure, till it reaches a maximum value. Beyond this, the peak height to width ratio starts decreasing with increasing pressure due to broadening. The optimum pressure is one at which the height to width ratio is maximum. The optimization of pressure is discussed in Section 5.9. At this pressure, maximum

sensitivity can be obtained. Thus, for accurate spectroscopic measurements, the pressure inside the vacuum cell must be precisely controlled to an optimum value.

The various components of the vacuum system used in the experimental setup are shown in Figure 4.13. For the calibration and measurements reported in this thesis, a turbo-molecular pump (HiCube 300 Classic, Pfeiffer Vacuum) was used. This pump can achieve ultimate vacuum level of the order of  $10^{-6}$  mbar. In the final compact system for online measurements in air, a dry diaphragm vacuum pump (MVP 020-3 AC PKT01100, Pfeiffer Vacuum) can be used. The later pump can achieve ultimate vacuum of 1 mbar.

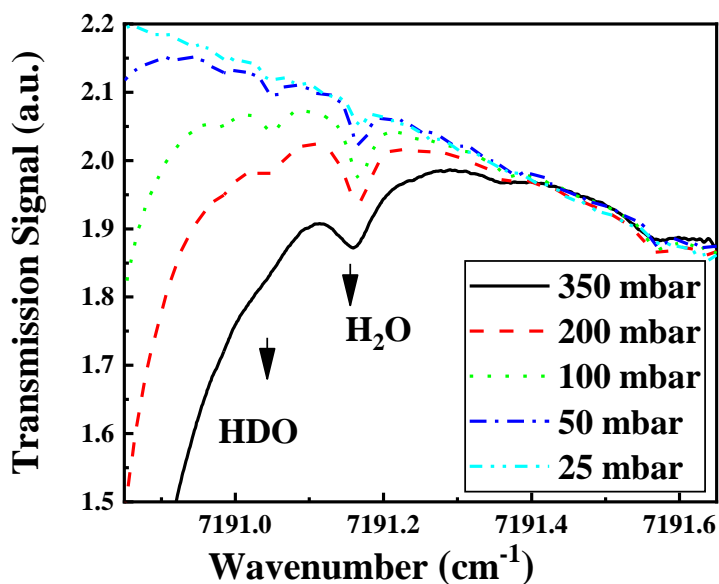


**Figure 4.12** The observed transmission signal at different pressures of air containing moisture.

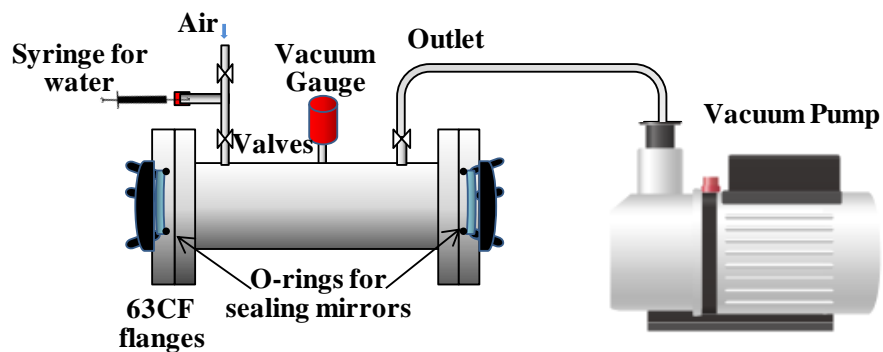


**Figure 4.13** Vacuum system used in development of OA-ICOS based trace heavy water detection system.

#### 4.5.1. Introduction of Sample into the Vacuum Cell

##### (a) Sampling Air

Air samples in the cavity can be introduced by a continuous flow through the system. The pressure inside the cell has been maintained by controlling the air flow through the inlet and outlet valves.

##### (a) Introducing Water Samples

The water samples must be vaporized into the cell for isotopic ratio measurements. Thus, for introduction of water samples, the cavity should be first evacuated to the base pressure of  $10^{-3}$  mbar, using the turbo molecular pump. A few micro litres of water sample can then be injected into the cavity by a micro-litre syringe through a silicon septum, which evaporates completely into the cavity. Since the volume of cavity is approximately 0.4 litres, 1 micro litre produces approximately 3.6 mbar of vapour pressure. The effect of phase change on the isotopic ratio is discussed later in Section 5.3.1.

#### **4.6. TEMPERATURE SENSOR FOR MEASURING THE TEMPERATURE OF THE SAMPLE**

In an equilibrium condition, the temperature of the vapor inside the cell is equal to the temperature of the vacuum cell. Thus, the temperature of the sample inside the cavity was monitored accurately by monitoring the cell temperature while acquiring the spectrum. For temperature measurement, a semiconductor based sensor (TSYS01) having accuracy of  $\pm 0.1$  °C and temperature resolution of 0.01 °C was used. The temperature sensing chip has 24 bit  $\Delta\Sigma$ - analog-to-digital converter (ADC) with internal factory set calibration enabling a good measurement accuracy. The effect of temperature on the measurements is described in Section 5.3.2.

#### **4.7. DATA ACQUISITION FOR OA-ICOS SYSTEM**

For recording the cavity transmission signal, the laser wavelength was scanned across HD<sup>16</sup>O and H<sub>2</sub><sup>16</sup>O peaks at 7191.039 and 7191.157 cm<sup>-1</sup> respectively by ramping the laser diode current. The ramp signal was generated using an arbitrary function generator. The output of both photodiodes and the wavelength scanning ramp were digitized using an oscilloscope (DSO7054, Agilent Technologies). The acquired signals were transferred to a personal computer for further processing. A user-friendly program was written, to acquire the averaged waveforms from DSO7054, using RS232 interface of the oscilloscope. The program also acquires the temperature of the cell and the pressure data while waveform averaging is performed with the oscilloscope. Screen shot of the signal on the oscilloscope is shown in Figure 4.14. Once acquisition is completed, the data was processed and spectrum fitting is performed to obtain the [HDO]. The details of fitting process are discussed in next Chapter. The measured temperature, pressure and [HDO] were displayed on the screen. Screen shot of the results displayed by the program are shown

in Figure 4.15. The fitted spectrum is plotted on left hand side of computer monitor; the temperature and pressure of the sample and [HDO] obtained from the fit are also displayed on the top of spectrum. On the right-hand side computer monitor, the time series plot of the measured [HDO] is shown. The values obtained from each fitted spectrum are shown by blue dots; and the moving average of 16 such values is plotted in red dots. The measured average [HDO] along with its standard deviation is also displayed on the monitor.

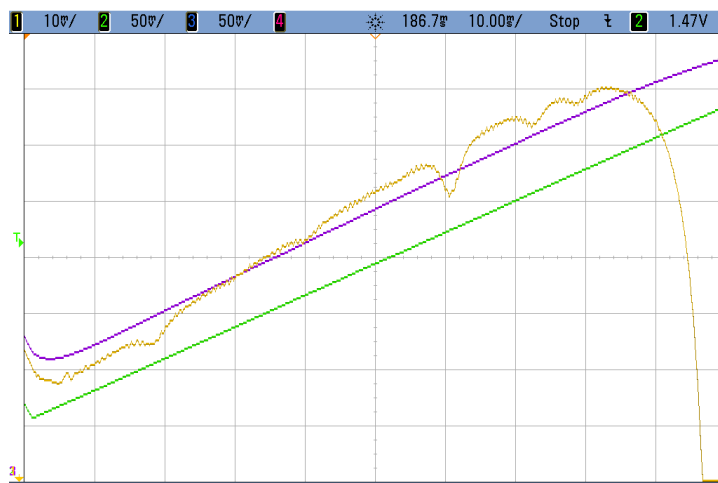


**Figure 4.14** Screen shot of the typical display on the oscilloscope. The averaged waveforms for the cavity output, laser intensity and the laser scanning voltage are shown in yellow, green and magenta respectively.

#### 4.8. SUMMARY

In this chapter, development and component selection of the OA-ICOS based HDO monitoring system are presented. An HDO peak at  $7191.04 \text{ cm}^{-1}$  has been found suitable as discussed in Section 4.1. Appropriate laser and mirrors were selected for achieving the required sensitivity. The design and alignment of the optical cavity is presented in this chapter. The requirements of the vacuum system and its specifications have been discussed. The data acquisition system for the

developed system is also briefed in this chapter. The results of various experiments conducted using this system are presented and discussed in the next chapter.

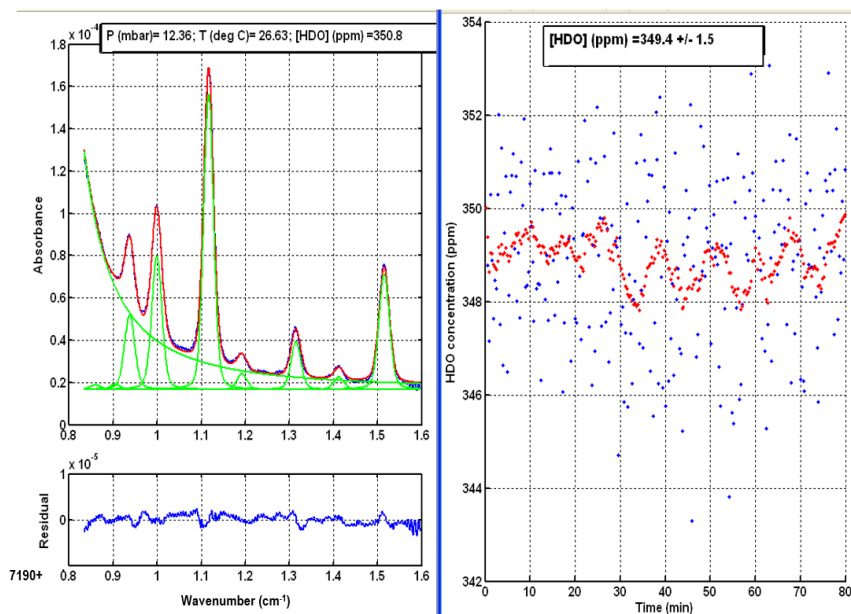


**Figure 4.15** Screen-shot of the results displayed by the program used for signal processing. The acquired spectrum and its fitting results are shown on left side of the monitor. The measured [HDO] along with the averaged time series plot of [HDO] are displayed on right side of the monitor. The averaged value of [HDO] and its standard deviation are displayed on top right.



## CHAPTER 5

### **SIGNAL PROCESSING, DATA ANALYSIS, CHARACTERIZATION AND VALIDATION OF THE DEVELOPED SYSTEM**

---

The acquired transmission signal contains the quantitative information of the concentration of the species existing in the sample. For extracting unknown concentration using the information from the acquired spectrum, it needs to be analysed processed and fitted with respect to the known spectral parameters. In this chapter, curve fitting methods and various parameters affecting the results are discussed. Finally, the important results of various measurements are presented and discussed.

#### **5.1. OA-ICOS SIGNAL: THEORETICAL ANALYSIS**

In this Section, the cavity transfer function; i.e., relation between transmitted intensity and the absorption coefficient is derived. Finally, limiting factors on sensitivity enhancement are discussed.

##### **5.1.1. Signal Enhancement by OA-ICOS Technique**

In OA-ICOS technique, the absorbance of the sample is calculated by measuring the transmitted intensity as a function of frequency [98, 99]. Figure 5.1 shows the intensity variation of the laser beam travelling inside the cavity. If  $I_{in}$  is the light intensity incident on the cavity mirror, the light reaching rear mirror after first pass is,  $I_{in} T_m e^{-\alpha(v)d}$ , where  $T_m$  is transmittance of mirror; the factor

$e^{-\alpha(\nu)d}$  comes from the absorption, governed by Beer-Lambert law, where  $\alpha(\nu)$  is frequency dependent absorption coefficient and  $d$  is the distance between mirrors. The intensity of the light reflected inside the cavity is attenuated by a factor of  $R_m e^{-\alpha(\nu)d}$  for each passage in the cavity, where  $R_m$  is reflectivity of mirrors. Hence, light intensity transmitted through the rear mirror after  $n^{\text{th}}$  round trip will be:

$$I_n = I_{in} T_m e^{-\alpha(\nu)d} * (R_m e^{-\alpha(\nu)d})^{2n} * T_m \quad (5.1)$$

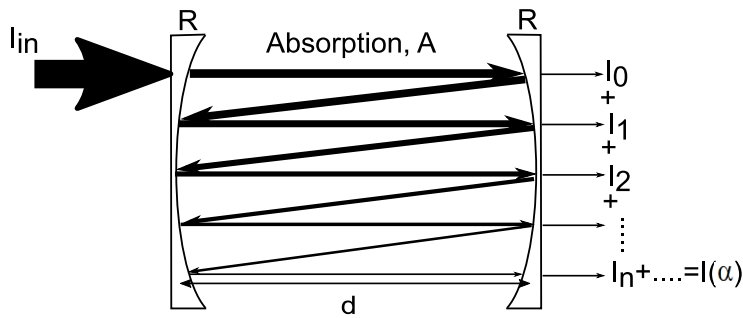


**Figure 5.1** Transmission signal for the optical cavity. The integrated cavity output is the sum of light intensity leaking on each reflection at rear mirror.

Total transmitted intensity can be written as the infinite sum (or integral) of intensities transmitted after each round trip:

$$I(\alpha) = I_{in} C_p T_m^2 e^{-\alpha(\nu)d} \sum_{n=0}^{\infty} (R_m e^{-\alpha(\nu)d})^{2n} \quad (5.2)$$

$$= I_{in} C_p T_m^2 \frac{e^{-\alpha(\nu)d}}{1 - (R_m e^{-\alpha(\nu)d})^2} \quad (5.3)$$

In the above equation, additional factor  $C_p$  is the coupling efficiency, whose value lies between 0 and 1, depending on degree of mode matching between cavity and laser. The above expression is valid when interference terms average out to zero. This happens when the cavity mode separation

(FSR) is less than the laser linewidth. Such a condition can be achieved in case of the off-axis alignment and also in the case of broadband or swept laser sources [100]. In the absence of absorber, the steady state transmission is given by:

$$I(0) = \frac{I_{in} C_p T_m^2}{1 - R_m^2} \quad (5.4)$$

This expression shows a significantly reduced power transmission through the cavity demanding a high-power laser to achieve a sufficient throughput. Here, maximum transmitted light intensity  $I(0)_{max} \approx \frac{I_{in} T_m}{2}$  can be obtained when  $T_m=1-R_m$  and  $C_p=1$ . However, this maximum transmission is difficult to attain in practical systems because the mirror transmission  $T_m$  is much lower than  $1-R_m$  for high reflectivity mirrors. This is due the fact that the scattering losses are of the order of  $1-R_m$ . In addition, ideal coupling is unattainable (hence  $C_p < 1$ ).

The normalized cavity transmittance is defined as:

$$T_{cavity} = \frac{I(\alpha)}{I(0)} = \frac{e^{-\alpha(v)d}}{1 - (R_m e^{-\alpha(v)d})^2} * (1 - R_m^2) \quad (5.5)$$

And the fractional absorption can be written as:

$$\frac{\Delta I}{I(0)} = \frac{I(0) - I(\alpha(v))}{I(0)} = (1 - e^{-\alpha(v)d}) \left( \frac{1 + R_m^2 e^{-\alpha(v)d}}{1 - R_m^2 e^{-2\alpha(v)d}} \right) \quad (5.6)$$

$$\frac{\Delta I}{I(0)} \cong (1 - e^{-\alpha(v)d}) \left( \frac{1}{1 - R_m e^{-\alpha(v)d}} \right) \text{ for } R_m \rightarrow 1 \quad (5.7)$$

where  $(1 - e^{-\alpha(v)d})$  is fractional absorption per pass. For weak absorption,  $\alpha(v)d \ll 1-R_m$ , the fractional absorption can be approximated as:

$$\frac{\Delta I}{I(0)} = \frac{1 - e^{-\alpha(v)d}}{1 - R_m} \cong \frac{\alpha(v)d}{1 - R_m} \quad (5.8)$$

Thus, for the limits  $\alpha(v)d \ll 1 - R_m$  and  $R_m \rightarrow 1$ , the effective path length is approximated to,

$$L_{\text{eff}} = \frac{d}{1 - R_m}. \quad (5.9)$$

The gain in fractional absorption signal due to cavity is derived using equation (5.7), is given by the following expression:

$$G = \left( \frac{1 + R_m^2 e^{-\alpha(v)d}}{1 - R_m^2 e^{-2\alpha(v)d}} \right) \cong \frac{1}{1 - R_m e^{-\alpha(v)d}} \text{ for } R_m \rightarrow 1 \quad (5.10)$$

Thus, the cavity gain is a function of absorbance. In a linear approximation, the gain can be written as:

$$G_0 \cong \frac{1}{1 - R_m} \quad (5.11)$$

The linear gain is valid only for very weak absorption. However, as the absorbance per pass,  $A(v)$  ( $= \alpha(v)d$ ) increases, the gain due to the cavity starts falling in accordance with equation (5.10). Physically, it can be interpreted as the decrease in the effective path length (or photon residence time in cavity) due to the absorption losses inside the cavity.

The absorbance per pass for which the effect of nonlinearity becomes significant, depends on the ratio of absorption losses relative to the mirror losses ( $1 - R_m$ ). Thus, a universal cavity gain and transmittance versus absorbance curve was obtained by normalizing the absorbance  $A$  by  $(1 - R_m)$ .

Figure 5.2 (a) shows the plot of normalized cavity transmittance,  $T_{\text{cavity}}$  as a function of  $\frac{A}{1 - R_m}$ .

Transmittance for an imaginary cell of length equal to  $L_{\text{eff}}$  is given as,  $T_{\text{eff}} = e^{-\alpha(v)L_{\text{eff}}}$ , which is

also been plotted in the figure for comparison. As shown in this figure, the dip in the transmission intensity for an optical cavity is lesser than that for an imaginary cell of length  $L_{\text{eff}}$ . The difference in two signals increases with increasing the absorbance per pass. This is also reflected in the normalised cavity gain function,  $G/G_0$ , calculated using equations (5.10) and (5.11) and is shown in Figure 5.2 (b). Both the curves show that the linear approximation is valid only for  $\frac{A}{1-R_m}$  up to 0.01, i.e. when the losses due to the absorption are two orders lower than the mirror losses. For absorption losses above this, the cavity gain starts falling rapidly with increasing absorbance.

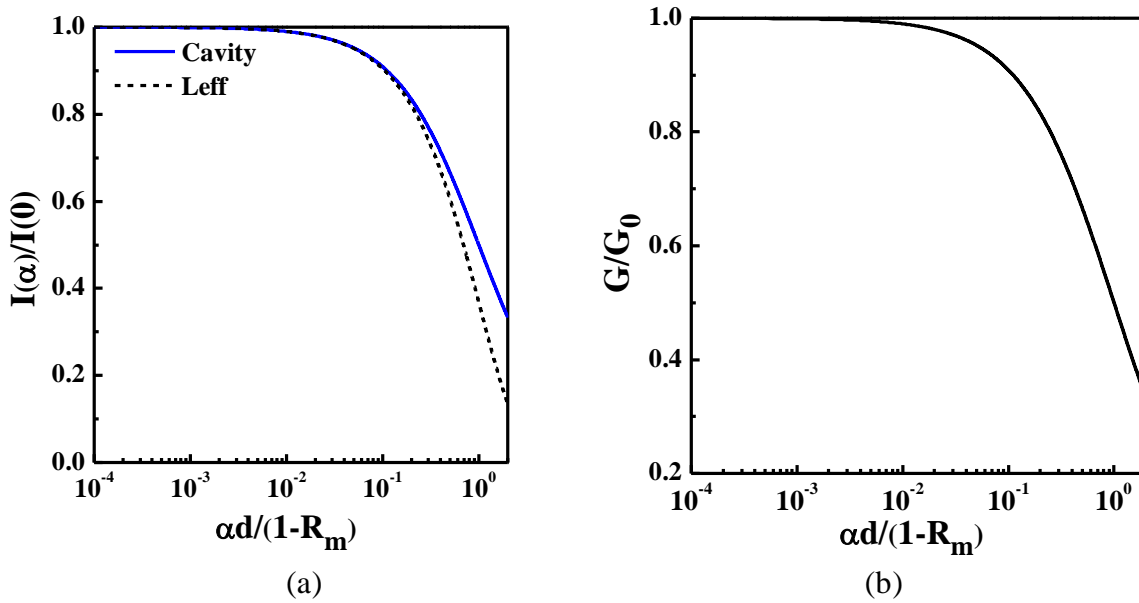


**Figure 5.2** (a) Comparison of the cavity transmission signal with an imaginary cell with path length  $L_{\text{eff}}$  as function of normalised absorbance per pass. The dip in transmission intensity for an optical cavity is lower than that for an imaginary cell of length  $L_{\text{eff}}$ ; (b) This is also reflected in the normalised cavity gain function,  $G/G_0$ , as a function of normalized absorbance per pass.

It must be emphasized that the gain of optical cavity is a complex function of the quantity to be measured, i.e. absorbance (see equation (5.5)). This complexity in the cavity gain function affects

the transmission spectrum in many ways. Figure 5.3 shows the effect of non-linearity on the cavity transmission function with respect to the linear gain assumption. The nonlinearity in gain effects quantitative concentration analysis, using integrated absorbance (IA), i.e. area under the recorded absorption spectrum defined as:

$$IA = \int_{-\infty}^{\infty} \frac{I(0) - I(\alpha(\nu))}{I(0)} d\nu \quad (5.12)$$

The calculated value of IA shows saturation with increasing concentration. The absorption saturation regime approaches earlier as compared to the equivalent direct path as shown theoretically by Maddaloni *et al.* [101]. They have also concluded that the optical cavities introduce an additional peak broadening and the absorption peak shapes show a clear disagreement from Gaussian (or Lorentzian or Voigt) peak shape as expected from the case of Beer-Lambert law [102]. The saturation effect in IA was observed experimentally for H<sub>2</sub>O peak at 7191.1568 cm<sup>-1</sup>, with increasing pressure as shown in Figure 5.4. However, many authors have used IA as the measure of concentration [101, 103, 104]. The calibration curves obtained by them have been reproduced in Figure 5.5 (a), (b), (c). These figures clearly show the effect of saturation in IA, due to cavity gain nonlinearity. Hence in this thesis, the transmittance per pass  $e^{-\alpha(\nu)d}$  is evaluated first by solving the transmission spectra for equation (5.6).

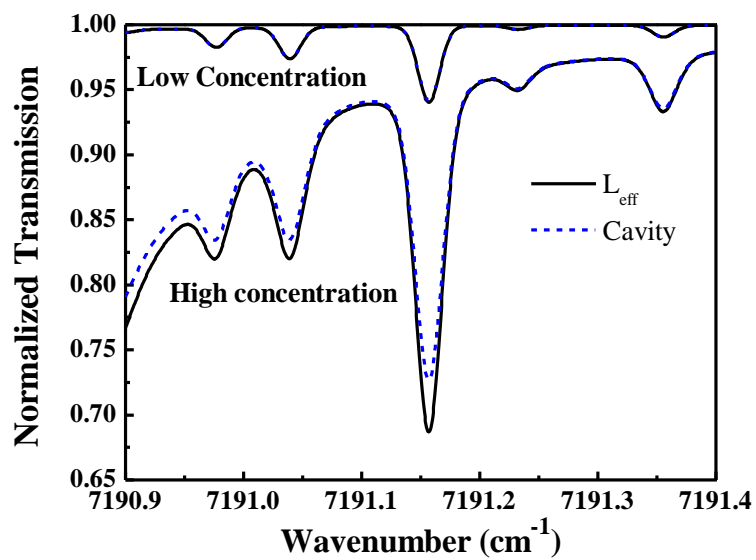


**Figure 5.3** Plot showing the effect of cavity gain nonlinearity on the absorption signal. For low concentration, the cavity acts like a cell with effective path length  $L_{\text{eff}}$ . However, at higher concentrations, the absorption signal deviates from linear approximation.

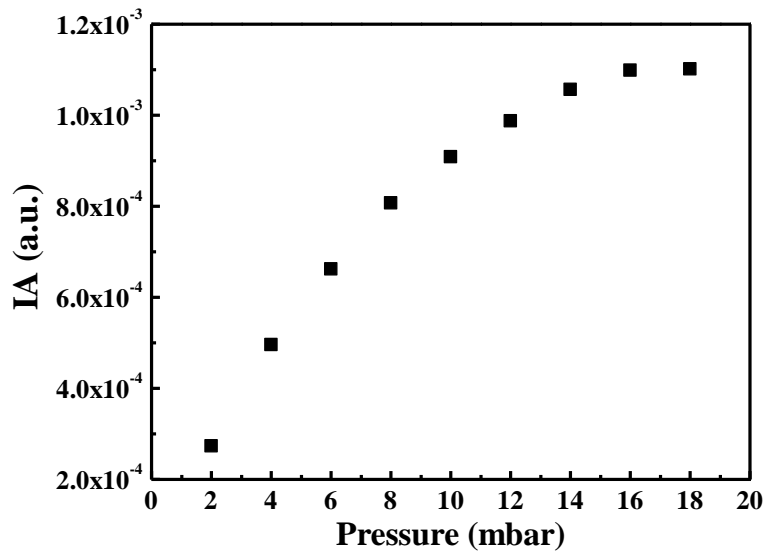


**Figure 5.4** The plot of observed integrated absorbance (IA) for water absorption at  $7191.16 \text{ cm}^{-1}$  with pressure shows saturation effect due to cavity gain nonlinearity.

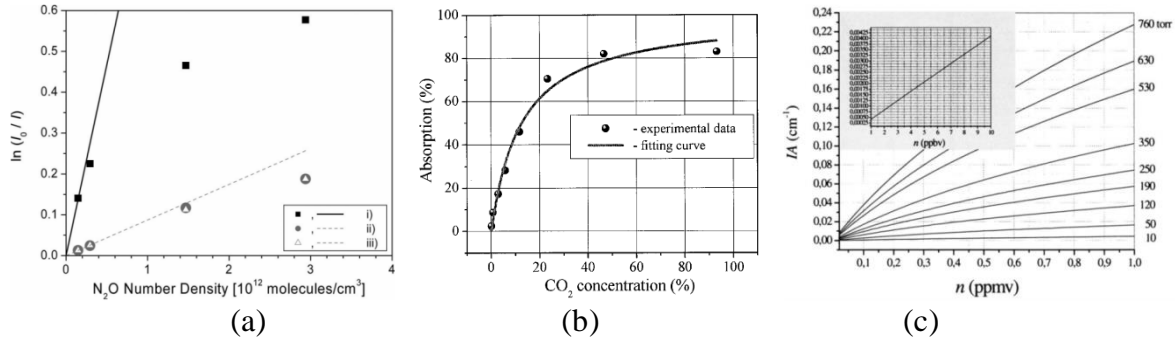


**Figure 5.5** Figures show non-linear calibration curves for concentration measurement when the concentration is calculated using integrated absorbance as obtained by: (a) Welzel et al. [103]\*; (b) Yury et al. [104]†; (c) Maddaloni et al. [101].

\*Reprinted with permission from [103]© The Optical Society;

†Reproduced from [104] [101] with the permission of AIP Publishing.

### 5.1.2. Limits on Sensitivity Enhancement by Optical Cavity

In the previous section (Section 5.1.1), through equations (5.6) to (5.11), it was shown that pathlength enhancement in OA-ICOS technique is proportional to  $1/(1-R_m)$ . However, in a practical system, the enhancement achievable is lower than this ideal approximation because of the electronic noise in the system and the optical noise due the cavity mode structure. The effect of these are quantified as shown below:

#### 5.1.2.1. Effect of Different Types of Noise in the System

The enhancement in ICOS technique comes at the cost of lower throughput (i.e. reduced signal intensity). The loss of signal intensity can result in a reduced SNR depending on the type of dominant noise. The effect of different types of noise on SNR enhancement has been studied by various researchers [105, 106]. B. Ouyang and Jones [105] have shown that the SNR enhancement

factor,  $Q_1$ , in case when the dominant noise is of type1 (like environmental noise which scales linearly with intensity) is given by:

$$Q_1 = \frac{1 + R_m^2 e^{-\alpha(\nu)d}}{1 - R_m^2 e^{-2\alpha(\nu)d}} \approx_{(R_m \rightarrow 1, \alpha(\nu)d \rightarrow 0)} \frac{1}{1 - R_m} \quad (5.13)$$

The SNR enhancement factor,  $Q_2$ , in case when the dominant noise is of type2 (like shot noise which scale as the square root of the light intensity) is given by:

$$Q_2 = T_m \frac{1 + R_m^2 e^{-\alpha(\nu)d}}{(1 - R_m^2 e^{-2\alpha(\nu)d})^{3/2}} \approx_{(R_m \rightarrow 1, \alpha(\nu)d \rightarrow 0)} \frac{T_m}{2(1 - R_m)^{3/2}} \quad (5.14)$$

The SNR enhancement factor,  $Q_3$ , in case when the dominant noise is of type3 (like thermal noise the photo-detector and associated electronics which is independent of intensity) is given by:

$$Q_3 = T_m \frac{1 + R_m^2 e^{-\alpha(\nu)d}}{(1 - R_m^2 e^{-2\alpha(\nu)d})^{3/2}} \approx_{(R \rightarrow 1, \alpha(\nu)d \rightarrow 0)} \frac{T_m^2}{2(1 - R_m)^2} \quad (5.15)$$

Since noise of all three types is are present in the system, the enhancement factor is expected to lie between  $\frac{1}{1-R_m}$  to  $\frac{T_m^2}{2(1-R_m)^2}$ , depending on the amplitudes of each type of noise in the system.

#### 5.1.2.2. Effect of Cavity Modes

Besides noise, other limiting factor in sensitivity enhancement comes from the cavity output intensity variation due to the residual effect of cavity mode structure. This mode structure arises from interference effects of overlapping beams. Kasyutich and Sigrist have calculated the peak-to-peak variation in the transmitted baseline intensity as a function of the laser linewidth ( $\Delta\nu$ ), cavity length ( $d$ ) and re-entrant number ( $K$ ) [107]. The important results derived by them are reproduced here. The cavity transmission in the presence of interference effects is given as:

$$\frac{I}{I_{in}} = T_c = C_p T_m^2 \frac{e^{-\alpha(v)d}}{1 - (R_m e^{-\alpha(v)d})^2} \times \frac{1 - (R_m e^{-2\alpha(v)d - 2\pi\tau_{RD}\Delta v})^{2K}}{1 - (R_m e^{-2\alpha(v)d - 2\pi\tau_{RD}\Delta v})^{2K} + 4(R_m e^{-2\alpha(v)d - 2\pi\tau_{RD}\Delta v})^K \sin^2\left(\frac{\pi c K \tau_{RD}}{v} + \phi_A K\right)} \quad (5.16)$$

The first term represents the cavity transmission in the absence of interference effects (See equation (5.3)), while the second term represents the additional factor arising due to the interference effects. The peak to peak baseline variation in the cavity transmission is given as:

$$\frac{T_{c \max} - T_{c \min}}{T_{c \max}} = \frac{M}{1 + M} \quad (5.17)$$

where M is defined as:

$$M = \frac{4(R_m e^{-2\alpha(v)d - 2\pi\tau_{RD}\Delta v})^K}{(1 - (R_m e^{-2\alpha(v)d - 2\pi\tau_{RD}\Delta v})^K)^2} \quad (5.18)$$

Equations (5.16) - (5.18) show that a large re-entrant number is required for complete mode noise suppression with narrow linewidth lasers and/or small cavity lengths. However, if the re-entrant number is large, there is a possibility of partial overlap of spots after a finite number of round trips, before reaching re-entrant condition. In such cases, the baseline intensity variation consists of various frequency components based on the number of round trips after which the overlap happens. The amplitude of variation however depends on the number of overlapping spots and the extent of overlap. In addition, any mechanical instability can cause hops between the different re-entrant conditions, resulting in drifts in the interference fringes. Hence, for narrow linewidth lasers, baseline intensity variation due to residual mode structure along with its drift deteriorates the sensitivity of the OA-ICOS system.

In such cases, where complete mode suppression cannot be achieved by off-axis alignment, the cavity mode suppression is achieved by either dithering the cavity length or laser frequency or both. Fast scanning of laser frequency along with averaging can also be used to achieve the same effect. Various authors have demonstrated the use of ICOS technique for ultrasensitive trace gas detection, some of which are found in references [59, 103, 108-115].

## **5.2. DATA PROCESSING AND SPECTRUM FITTING**

The major components of the data acquisition system used in the developed system are described in Section 4.7. In this section data processing and spectrum fitting are detailed. In the system, the laser wavelength was varied by applying a saw tooth wave with amplitude of  $0.28 V_{p-p}$  and a 1.46 V offset at 8 Hz rate to the analog input of the laser driver module, i.e.,  $V_{analog}$  varies from 1.18 V to 1.74 V, and diode laser current varies from 59 mA to 87 mA. This scans the laser wavelength from 1390.51 to 1390.69 nm ( $\equiv$  wavenumber 7191.6 down to 7190.7  $cm^{-1}$ ). The transmission signal from the cavity, the laser intensity and the ramp voltage were recorded on a digital oscilloscope. The signals were averaged for 100 cycles, resulting in 0.08 Hz averaged data rate (integration time of 12.5 sec). The plot of typical signals recorded using the developed system is shown in Figure 5.6. The absorbance per pass is calculated from the recorded signals using equations (5.5), “Cavity transmission equation” and (4.2), “laser wavelength calibration”. A plot of typical absorption spectrum and curve fitting results are shown in Figure 5.7. Appendix IV lists the absorption peaks with measurable absorption in the spectral window under consideration. By fitting the obtained absorption spectrum, the concentration of the constituent species can be determined using the information of spectral parameters listed in Appendix IV.

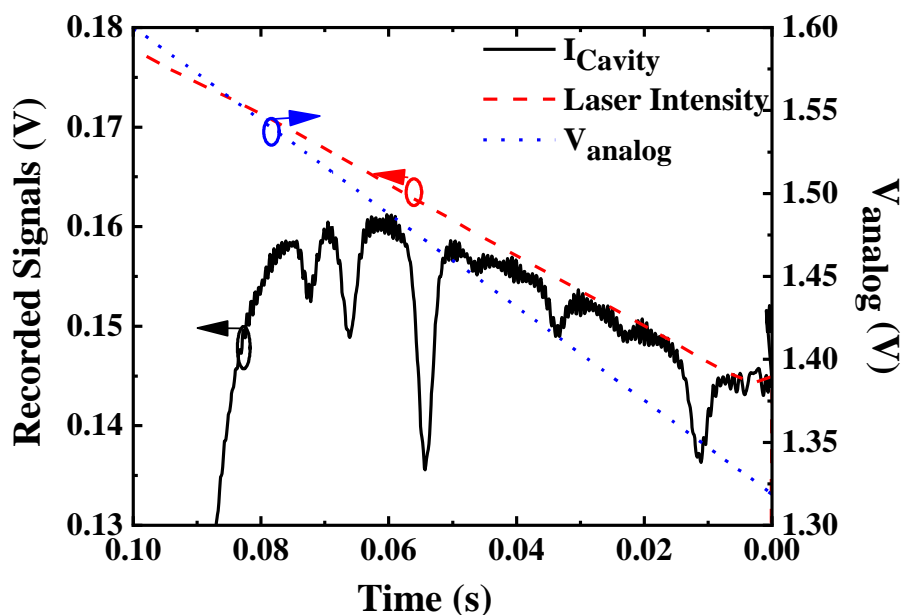


**Figure 5.6** Plot of the typically recorded oscilloscope signals showing variation of recorded cavity output, laser intensity and laser scanning voltage ( $V_{\text{analog}}$ ) with time.  
 Note: Time scale is reversed to show the spectrum from lower to higher wavenumber.

The accurate determination of concentration from this spectrum is strenuous because of the following complexities associated with the recorded spectrum:

- (a) The peaks under consideration are sitting on the Lorentzian wing of a strong absorption peak at  $7190.7385 \text{ cm}^{-1}$ . Hence baseline is not clearly defined.
- (b) There is some overlap between most of the peaks. Thus, shoulder of the peaks is not clearly distinguishable.
- (c) The fringes generated due to the cavity modes and overlapping spots results in both high and low frequency fluctuations in the baseline of the spectrum.

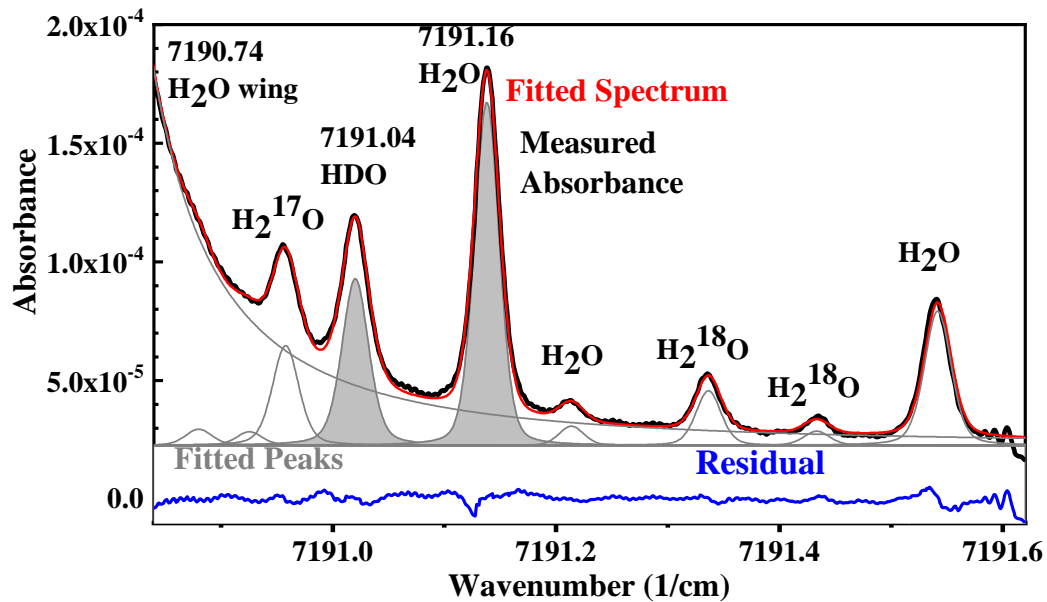


**Figure 5.7** Typical observed absorption spectrum and curve fitting results (fitted Voigt profile for each peak, overall spectrum and the residual). The peak position and corresponding isotopologue for each peak are indicated. The area under the HDO and H<sub>2</sub>O peak is shown by shaded region.

Hence, a fitting algorithm is devised to overcome the above limitations and for accurate determination of absorption coefficient. More details in least square curve fitting and fitting algorithm are given in Appendix III.3. The important features of the fitting algorithm are as following:

- (a) The relative distance between the peak positions in the algorithm are kept fixed while an overall shift in spectrum is allowed to take the laser frequency shifts into account, if any.
- (b) Each absorption peak is fitted to the Voigt profile and the absorbance spectrum is obtained by adding contribution of all peaks.

- (c) The peakwidths of each absorption peak are calculated using spectroscopic parameters, which is kept fixed in the fitting algorithm.
- (d) Other broadening effects are included in the model by allowing a constant broadening to the Gaussian component of the peak profile.
- (e) The strong absorption peak which lies outside the spectral window is also included in the fitted peaks. Thus, the baseline is fitted to a constant bias plus its Lorentz wing.
- (f) The peaks with strength less than  $1e-26$  are not included in the fitting algorithm, as the absorption signal produced by them is lower than noise amplitude. This assumption is valid because there are a large number of weak absorption peaks and the combined effect of all these is a constant shift in the baseline of spectrum.
- (g) The peak widths used in the fitting algorithm are calculated from the measured temperature and pressure while recording the spectrum.
- (h) To remove the high frequency mode noise, the spectrum is smoothed before fitting.
- (i) To eliminate the effect of drifts due to low frequency mode noise, heavy averaging is used.

These features of the fitting algorithm ensure fast, robust and a good quality fit ensuring accurate determination of the concentration. The area under the peak is calculated by trapezoidal integration of fitted peaks. The volume mixing ratios,  $q$ , is then calculated from area under the peak using spectral parameters listed in table IV.1 Since, the absorption peaks corresponding to major water isotopologues ( $H_2^{16}O$ ,  $H_2^{18}O$ ,  $H_2^{17}O$ ,  $HD^{16}O$ ) is present in the spectrum, the concentration of all these can be studied using the recorded spectrum.

### 5.3. FACTORS AFFECTING ISOTOPIC RATIO MEASUREMENT USING OA-ICOS TECHNIQUE

The isotopic composition of a sample in OA-ICOS system is measured from the observed absorption spectrum, by calculating area under the absorption peak of respective isotopologues. However, observed experimental spectrum is affected by the experimental conditions. The parameters which have significant effect on the measured concentration are isotopic fractionation and temperature. There might be change in the concentrations due to isotopic fractionation, owing to difference in physical properties for each isotopologue. Since isotopic fractionation is also temperature dependent, the concentrations are temperature dependent. In addition, the line-strength and peak profile of each absorption peak are affected differently by the temperature and pressure. The systematic effect of these factors on the isotopic ratio measurement of water is described in this section.

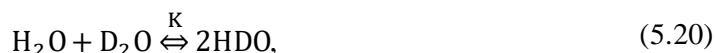
#### 5.3.1. Effect of Isotopic Fractionation on Sampling

The relative partitioning of the lighter and heavier isotopes between two coexisting phases is known as isotopic fractionation. In order to measure the isotopic (D/H) ratio, the water sample must be vaporized into the cavity. The isotope fractionation during the phase change from liquid to vapor affects the concentration of HDO in both the phases. Isotopic distribution amongst the molecules depends on D/H fractionation factor  $\alpha_{L-V}$  between liquid phase L and vapor phase V, which is defined as:

$$\alpha_{L-V} = \left(\frac{D}{H}\right)_L / \left(\frac{D}{H}\right)_V \quad (5.19)$$

where  $(D/H)_L$  and  $(D/H)_V$  are atomic ratios in the liquid phase and vapor phase respectively.

The fractionation factor  $\alpha_{L-V}$  and ratio of equilibrium constant ( $K_V/K_L$ ) for the reaction,



under equilibrium condition have been calculated by Kakiuchi *et al.* [116], and; which are reproduced in Table 5.1. Since the values of fractionation ratio,  $\alpha_{L-V}$  is greater than one, the D isotope remains preferentially in the liquid during vaporization. Thus, when a fraction of sample is vaporized, then the [HDO] in the remaining liquid will be higher than that in the vapour phase. During the construction of the HDO detection system, the effect of isotopic fractionation was observed experimentally.

**Table 5.1** D/H fractionation data values and equilibrium constant ratios between vapour and liquid phases in the temperature range from 0- 100°C in pure water system [116].

Temperature (° C)	$10^3 \ln \alpha_{L-V}$	$\alpha_{L-V}$	$K_V/K_L$
0	106.2	1.112	0.992
10	92.7	1.097	0.993
20	81.1	1.084	0.994
30	71.1	1.074	0.994
40	62.4	1.064	0.994
50	54.7	1.056	0.995
60	48.0	1.049	0.995
70	42.1	1.042	0.995
80	36.8	1.037	0.996
90	32.1	1.033	0.996
100	28.0	1.028	0.997

For this experiment, the port with septum (for sample injection with syringe) was replaced with a glass container. Few drops of water were filled in the container and then it was sealed to the inlet

of vacuum chamber. A portion of sample was vaporised so as to fill the optical cell at approximately 10 mbar vapour pressure. The concentration of HDO in the vapours was measured by using the procedure described in section 5.2. The cell was evacuated to  $10^{-3}$  mbar to ensure that previous sample is completely removed and refilled to measure the [HDO] in the remaining liquid. The process of evacuation and refilling took about 10 minutes of time. The process was repeated till the glass container was empty. The remaining sample shows an increasing concentration of HDO as shown in Figure 5.8. Thus, when it is required to measure the isotopic ratio in liquids samples by vaporizing them, the fractionation ratio should be taken into account, if the complete sample is not vaporized. To avoid an error due to fractionation, the liquid phase samples should be inserted in a small quantity such that the whole sample is vaporized.

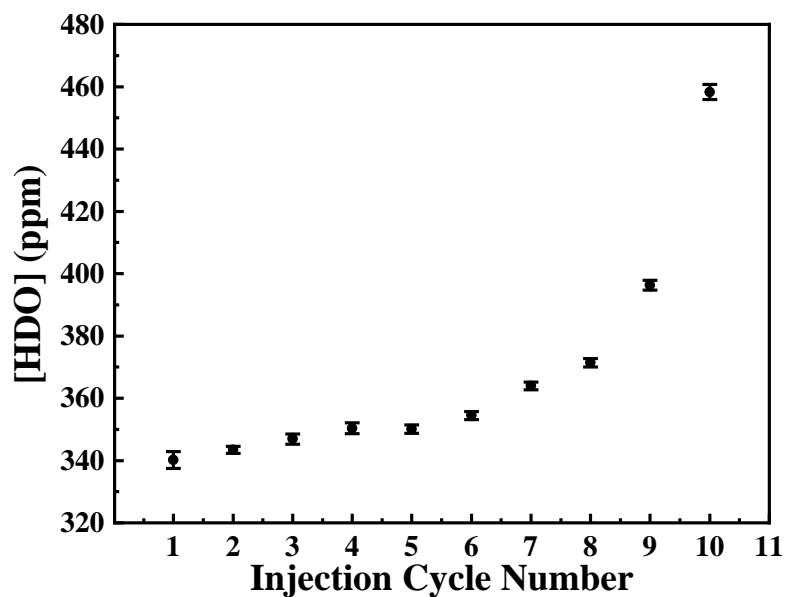


**Figure 5.8** Effect of isotopic fractionation on the observed value of [HDO] in the water sample, for successive injection of same sample after each cycle off evacuation and injection.

### 5.3.2. Effect of Temperature on Estimated Concentration

In the method presented in this thesis, the [HDO] is determined from the ratio of area under HDO and H<sub>2</sub>O absorption peaks at 7191.0392 and 7191.1570 cm<sup>-1</sup> respectively. The temperature of the sample affects the line-strength, *S*, and peak shape parameter,  $\Gamma$ , of both the absorption peaks differently. Since, the area under absorbance per pass, *A*, is directly proportional to the line-strength, *S*(*T*), its temperature dependence makes isotopic ratio measurement temperature dependent. The temperature dependence of *S*, is due to the change of population in the lower and upper energy levels with temperature. This can be calculated using the following equation and parameters listed in HITRAN database [43],

$$S(T) = S(T_0) \frac{Q(T_0) \exp\left(-\frac{hcE_L}{kT}\right) \left(1 - \exp\left(-\frac{hcv_c}{kT}\right)\right)}{Q(T) \exp\left(-\frac{hcE_L}{kT_0}\right) \left(1 - \exp\left(-\frac{hcv_c}{kT_0}\right)\right)} \quad (5.21)$$

where, *E<sub>L</sub>* represents the lower energy level (in cm<sup>-1</sup>), *v<sub>c</sub>* is the centre wavenumber of transition, *T<sub>0</sub>* is the reference temperature, *T* is the temperature of sample, and *Q*(*T*) is the total internal partition sum. An empirical formula for calculating *Q*(*T*) is approximated by a polynomial:

$$Q(T) = a + bT + cT^2 + dT^3 \quad (5.22)$$

The coefficients of empirical polynomial are calculated by Gamache *et al.* [117]. During the analysis, typographical errors were found in Table 1 of reference for water isotopologues; where the negative sign for *d* coefficient is missing. The corrected values are given in Table 5.2. The values were verified by comparing the *Q*(*T*) values (for low temperature range) obtained from HITRAN database website, (<http://www.hitran.org/docs/iso-meta/>). Figure 5.9 (a) and (b) show

the comparison of  $Q(T)$  values from HITRAN data base, and with corrected coefficients for  $H_2O$  and HDO respectively.

**Table 5.2** The polynomial coefficients for equation (5.22) for a low temperature range of 70 to 500 K.

Water Isotope	$a$	$b$	$c$	$d$
$H_2^{16}O$	-4.4405	0.27678	0.0012536	$-4.8938 \times 10^{-7}$
$H_2^{18}O$	-4.3624	0.27647	0.0012802	$-5.2046 \times 10^{-7}$
$H_2^{17}O$	-25.767	1.6458	0.0076905	$-3.1668 \times 10^{-6}$
HDO	-23.916	1.3793	0.0061246	$-2.1530 \times 10^{-6}$

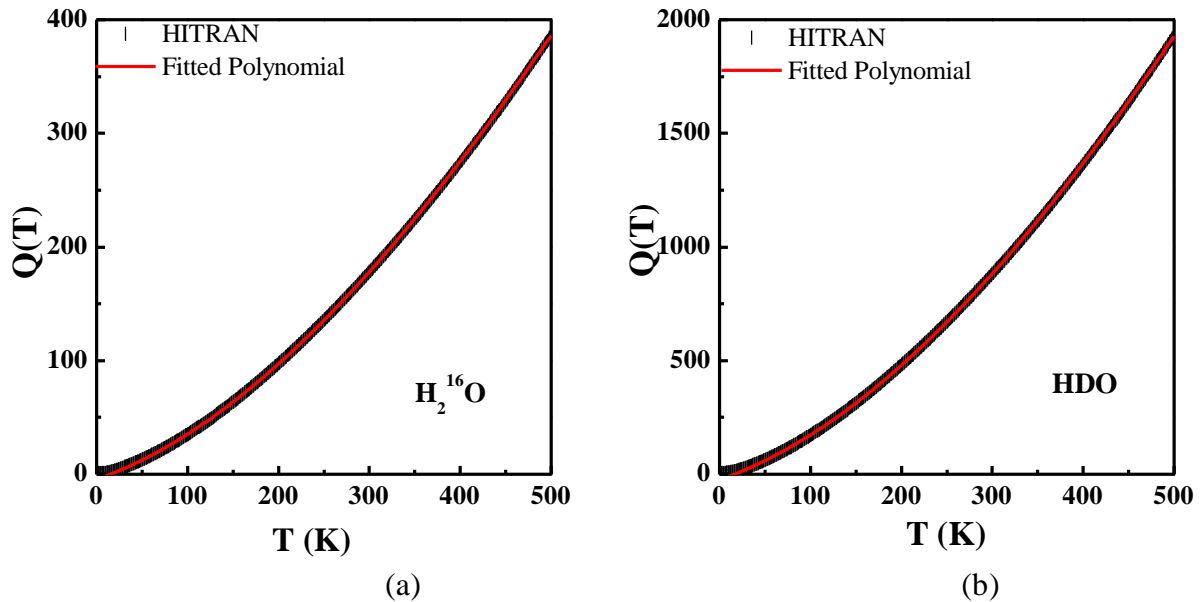


**Figure 5.9** Comparison of temperature dependent total internal partition function  $Q(T)$  values for (a)  $H_2^{16}O$  and (b) HDO, obtained from HITRAN database and calculated values with coefficients given in Table 5.2.

The variation of line-strength with temperature,  $S(T)$ , for the absorption peaks were calculated by substituting the values from Appendix IV and Table 5.2 in equation (5.22). Figure 5.10 shows the plot of calculated values of  $S(T)/S(T_0)$  for these peaks and their ratio, i.e.

$[S(T)/S(T_0)]_{7191.039}:[S(T)/S(T_0)]_{7191.157}$  at different temperatures. The area under the HDO absorption peak decreases by 0.26 %/K, while for H<sub>2</sub>O peak, it increases by 2.56 %/K. From the slope of the ratio of  $[S(T)/S(T_0)]_{7191.039}:[S(T)/S(T_0)]_{7191.157}$ , the temperature coefficient of the concentration measurement is determined to be approximately -2.81 %/K change in temperature. It means that for natural water samples, 1 K error in temperature measurement can result in 8.99 ppm error in the measured concentration. Thus for  $\pm 1$  ppm accuracy in [HDO], the temperature of the sample must be known with an accuracy of  $\pm 0.1$  K.

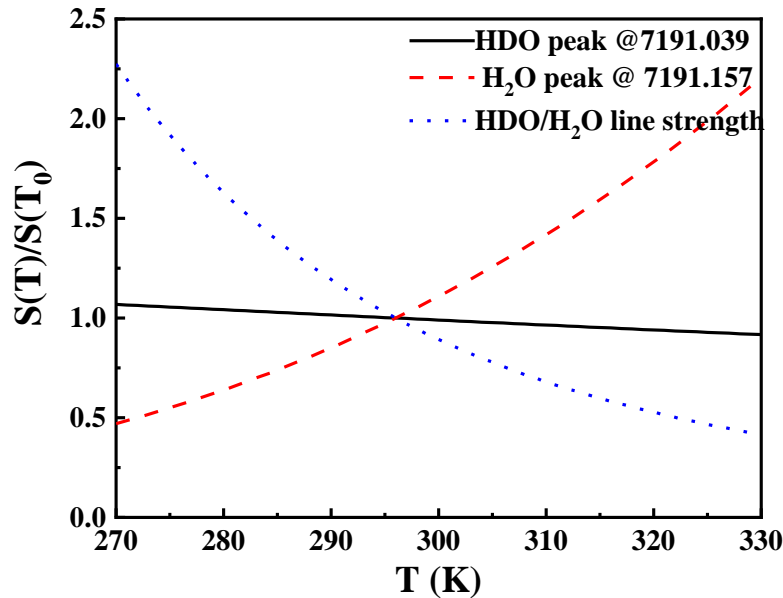


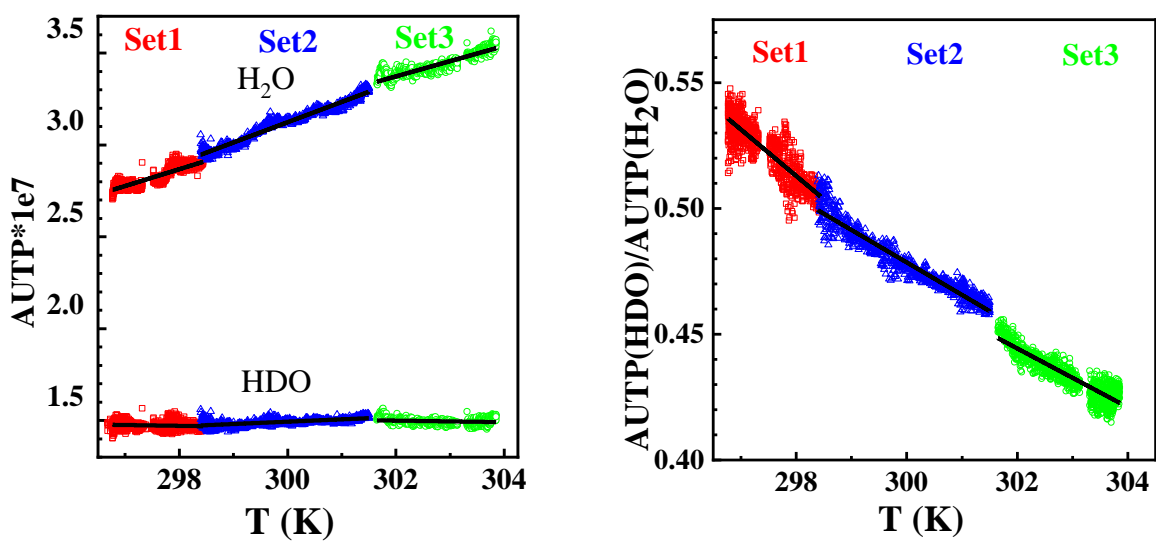
**Figure 5.10** Normalized variation of line-strengths for HDO peak at 7191.0139 cm<sup>-1</sup>, H<sub>2</sub>O peak at 7191.157 cm<sup>-1</sup>, and ratio of HDO to H<sub>2</sub>O line-strength, with temperature from 270 to 330 K (-3 to 57 °C).

To verify the effect of temperature on the measurements, the concentration data was recorded for three days while varying the room temperature. Figure 5.11 (a) shows three sets of experimentally observed variation in area under the H<sub>2</sub>O and HDO peaks. The ratio of area under the peaks is

shown in Figure 5.11 (b). The measured [HDO] with temperature is shown in Figure 5.11 (c). The linear fit to the data is shown in red line in Figure 5.11. The observed change in area under HDO and H<sub>2</sub>O peaks is tabulated in Table 5.3. The measured results are in agreement with the theoretical values. The calculated variation in the measured [HDO] with temperature is less than  $\pm 0.7\%/K$  which is within the measurement error bar of [HDO] (see Table 5.3). This variation might be the effect of some other unknown parameters. Hence, accurate [HDO] can be obtained by including temperature variation of spectral parameters while fitting the spectrum.

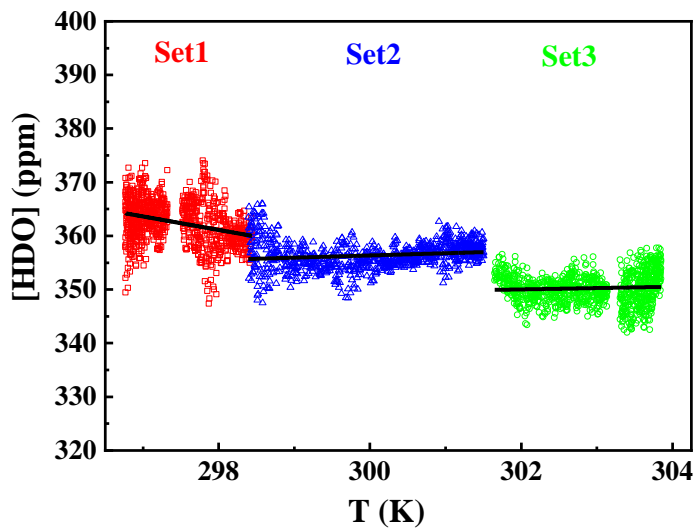
**Table 5.3** Effect of temperature on the measured parameters of absorption peaks.

Parameter (%/K)	Set 1 (Black Markers), T=298		Set 2 (Blue Markers), T=300 K		Set 3 (Red markers), T=303 K	
	Theoretical	Measured	Theoretical	Measured	Theoretical	Measured
Variation of Area Under HDO Peak	-0.26	-0.52	-0.26	0.84	-0.26	-0.38
Variation of Area Under H <sub>2</sub> O Peak	2.59	3.08	2.55	2.63	2.49	2.37
Variation of Ratio	-2.84	-3.58	-2.81	-2.69	-2.75	-2.76
Variation in [HDO]	0	-0.66	0	0.11	0	0.07
Measured [HDO] (ppm)	361.1 $\pm$ 4.79		356.74 $\pm$ 2.60		350 $\pm$ 2.82	



(a)

(b)



(c)

**Figure 5.11** Three sets of experimentally observed variation (with linear fit) in; (a) Area under H<sub>2</sub>O and HDO peaks shows the total water concentration inside the cell; (b) Ratio of area under the H<sub>2</sub>O and HDO peaks is in agreement with the change in line-strengths with temperature; and (c) [HDO] with temperature after correcting for temperature variation. AOTP: Area under the peak.

### **5.3.3. Measurement of Mirror Reflectivity**

As per equations (5.7)-(5.11), the absorption signal gain in an optical cavity is a function of the mirror reflectivity. Thus, for calculating the absolute absorption coefficient  $\alpha(\lambda)$  of the sample, the reflectivity of mirrors should be precisely known. The quoted value of reflectivity of mirrors obtained from CRD optics Inc. is 99.98 %. However, practical reflectivity may be slightly different from the quoted values for commercially procured mirrors. In addition, there may be degradation of mirror reflectivity with continuous use, due to degradation of surface and accumulation of dust. Thus, accurate determination of reflectivity is necessary.

The calibration of the mirror's reflectivity was performed by injecting known quantities of water vapour with natural isotopic composition. The mirror reflectivity is deduced by fitting the observed spectrum with the variable reflectivity values while ensuring that it yields correct composition. Water vapour introduced into the cavity at different pressures was used for the calibration. To minimize the uncertainty, it is important to ensure that there are no residual gases in the cavity. For this purpose, the cavity was first evacuated to the base vacuum of  $10^{-3}$  mbar and the water vapour was flushed through the cavity thrice, while evacuating to the base vacuum each time. Finally, the water vapour was introduced at the pressures varying from 2 to 18 mbar. From these measurements, the reflectivity of mirrors has been deduced to be 0.9992 %.

### **5.3.4. Selection of Appropriate in Database**

The HITRAN and GEISA databases are the two well-known compiled spectral databases. The spectral parameters of water absorption peaks obtained from HITRAN and GEISA are reproduced in Appendix IV. The values of some of the parameters are different for both the

databases. For example, the line-strengths given by GEISA database are up to 47.2 % higher compared to that in HITRAN database. Table 5.4 shows the comparison of line-strengths listed by HITRAN and GEISA databases for absorption peaks under consideration.

**Table 5.4** Comparison of line-strengths listed by HITRAN and GEISA databases.

Isotopologue	Transition Wave Number ( $\text{cm}^{-1}$ )	Line-Strength		% Difference
		HITRAN	GEISA	
$\text{H}_2^{16}\text{O}$	7190.7388	3.94E-22	3.941E-22	0.025
$\text{H}_2^{16}\text{O}$	7190.7473	4.43E-26	4.625E-26	4.402
$\text{H}_2^{16}\text{O}$	7190.7809	3.15E-24	4.639E-24	47.270
$\text{H}_2^{16}\text{O}$	7190.8999	3.75E-26	3.745E-26	-0.133
<b>HDO</b>	7190.9444	1.53E-26	1.847E-26	20.719
$\text{H}_2^{17}\text{O}$	7190.9774	4.11E-25	4.275E-25	4.015
<b>HDO</b>	<b>7191.0392</b>	<b>6.90E-25</b>	<b>8.145E-25</b>	<b>18.043</b>
$\text{H}_2^{16}\text{O}$	<b>7191.1568</b>	<b>1.48E-24</b>	<b>1.517E-24</b>	<b>2.500</b>
$\text{H}_2^{16}\text{O}$	7191.2320	7.35E-26	7.35E-26	0.000
$\text{H}_2^{18}\text{O}$	7191.3550	2.42E-25	2.503E-25	3.430
$\text{H}_2^{18}\text{O}$	7191.4523	6.86E-26	8.542E-26	24.519

The difference in the line-strength of HDO peak at 7191.0392 and  $\text{H}_2\text{O}$  peak at 7191.1568  $\text{cm}^{-1}$  is 18.04% and 2.5% respectively. In the experiments, the fraction of HDO in water sample was evaluated by taking the ratio of area under the respective peaks. In this case, the values evaluated using GIESA database are 15.2% lower than that evaluated using HITRAN database. Also, air pressure shift of the peak position for HDO peaks is zero in GEISA database while there is a finite shift as per HITRAN database. The difference in the peaks positions is up to 0.001  $\text{cm}^{-1}$ . This difference is neglected for the fitting model used in this thesis, since error in fitting due to

difference in peak position was negligible. This is due to the fact that the peak widths are more than an order higher than the shift in peak positions.

Selection of the appropriate database among the available databases was based on the measurement on known samples of varying concentration. Figure 5.12 shows the comparison of estimated [HDO] using HITRAN and GEISA databases. With the HITRAN database the slope of measured and actual change in concentration curve is approximately one. Hence, the HITRAN database was used in all measurements presented in this thesis.

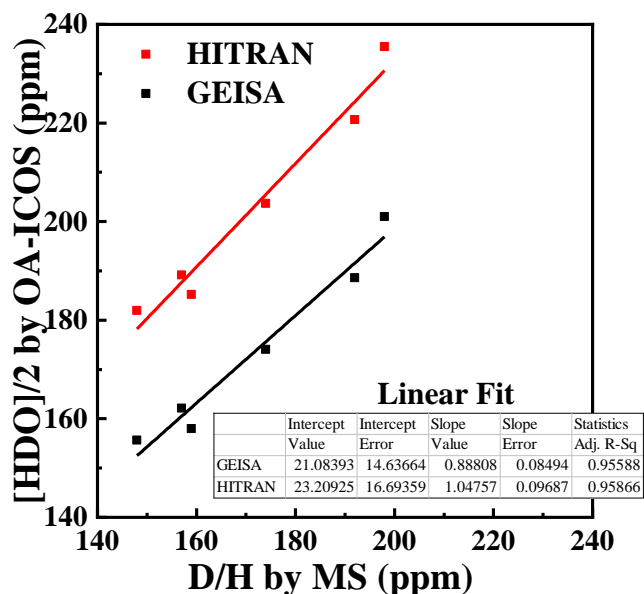


**Figure 5.12** Comparison of the [HDO] obtained using HITRAN and GEISA database. [HDO] is divide by 2 to get equivalent D/H. Since the slope of plot using HITRAN database is approximately 1, the HITRAN database was used in all subsequent measurements.

#### 5.4. CALIBRATION WITH STANDARD SAMPLES

For checking the sensitivity and accuracy of the system for [HDO] measurement, samples with different [HDO] were prepared by mixing standard water samples viz. natural water, D enriched water and D depleted water. The equilibrium [HDO] was calculated from the equilibrium constant and known initial concentration of the standard samples. The [HDO] varying from 20 ppm to 310 ppm were prepared by mixing the standard deuterium depleted water sample with natural water in known ratios. The samples with [HDO] above natural composition were prepared by adding a few micro-litres of 96% pure heavy water to the natural water. Four micro-litres of these samples were introduced into the evacuated cavity. A typical observed absorption spectrum in the wavenumbers ranging from 7190.8-7191.4  $\text{cm}^{-1}$  is shown in Figure 5.7. The volume mixing ratios,  $q$ , for HDO and  $\text{H}_2\text{O}$  peaks ( 7190.03 and 7190.16  $\text{cm}^{-1}$  respectively) are determined by the procedure described in Section 5.2. The [HDO] concentration in water sample is obtained from the ratio of calculated  $q$  values.

Figure 5.13 shows the correlation plot between measured [HDO] and prepared concentration by using linear least square fit. The linearity correlation is 0.998 which shows a quite good linearity in the measurement for [HDO] ranging from 20 ppm to 2280 ppm. Each point in the plot represents the concentration value obtained from curve fitting to the recorded absorption signal as shown in Figure 5.7. A number of such scans were recorded for each concentration. The values obtained show a standard deviation of less than 2.5% for sample concentration higher than 100 ppm, however for lower concentrations, standard deviation is up to 5%. To improve the accuracy of the measurements, averaging over a fixed number of individual values was necessary to obtain the accurate value of the measured concentration. The percentage error in the average measured

concentration (averaging over 20 data points) as compared to the prepared concentration is less than 5%. The measurement of isotope ratio in water samples was earlier observed to show a significant memory effect, due to the condensation of water on the walls of optical cavity [118]. Hence, such large steps are avoided in the calibration procedure. In addition, system is rinsed with sample before starting measurement.

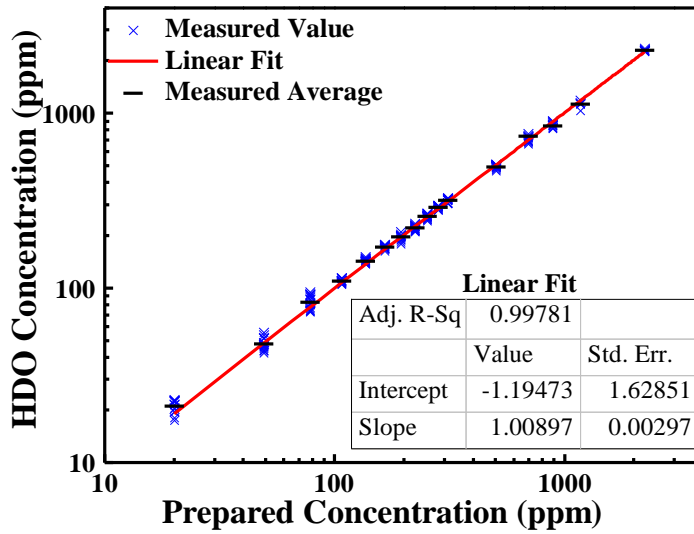


**Figure 5.13** Correlation plot of concentration measurement, shows linearity in measurement for [HDO] ranging from 20 ppm to 2280 ppm. Twenty sets of measurements were taken for each concentration. As individual measurement shows some deviations, averaging over these sets is required to obtain the accurate measured value.

The MDA per pass is  $1 \times 10^{-6}$ , which is mainly limited by the fringes in the absorption spectrum. The standard deviation for twenty independent measurements is below 5% over the entire range of [HDO]. This deviation is attributed to the uncertainties in the curve fitting as well as experimental errors, like uncertainty in the amount of injected sample, measurement error in temperature and pressure, etc. The contribution of error due to the uncertainties in curve fitting is

rather small, and is approximately 1 ppm and the error is mainly due to other experimental conditions. The error in fitting was estimated from the error in area under the peak. Since, the uncertainties in these measurements are high, improvement in sensitivity was essential, which is described in subsequent sections.

## **5.5. SENSITIVITY AND ALLAN VARIANCE OF [HDO] MEASUREMENT**

The sensitivity and the detection limit for concentration measurement by the laser spectroscopic method can be improved significantly by averaging. However, the averaging time is limited by the time dependent drifts in the system. Thus, it is important to quantify the maximum averaging time within which the sensitivity of the detection system can be improved by means of averaging. The maximum averaging time for the developed system was estimated by means of Allan Variance.

For the determination of maximum averaging time, the concentration in natural water sample was recorded for whole day. About 12 mbar of water vapour was created by inserting approximately 4  $\mu$ l of water sample through a silicone septum. The spectrum is recorded along with the pressure and temperature continuously. Typically observed pressure drift during the measurement was about 1 to 2 mbar and temperature drift was about 1 K. The data is processed to determine [HDO] and the time series of the [HDO] was recorded. The effect of pressure drift and temperature drift were compensated in the fitting algorithm as discussed in section 5.3. The time series plots of recorded [HDO] with and without cavity length dithering are shown in Figure 5.14 (a) and (b) respectively.

In the above measurements, the main limiting factor deciding the sensitivity is the fringe noise due to cavity mode structure. As discussed in Section 5.1.2.2, the cavity mode noise can be averaged

out by cavity length dithering. Thus, one of the tilt adjusting screw was replaced by a piezoelectric actuator. The time series plot shows a considerable reduction in the fluctuations in individual measurement, as shown in Figure 5.14 (b). The same reduction can also be seen in Allan variance plot, as shown in Figure 5.14 (c). The Allan variance plot, for all three sets, shows that optimum averaging time for measurement is 1280 sec (= 21 minutes). Since each data point was recorded approximately after 20 seconds, this corresponds to an average of 64 data points. Figure 5.15 shows the plot of standard deviation with averaging time. The standard deviation of less than  $\pm 1.5$  ppm can be obtained by averaging for 160 sec (8 averaging). The sensitivity can be improved to  $\pm 1.2$  ppm by averaging for longer time up to optimum period of 1280 sec. For faster acquisition, averaging for 160 sec was used.

To evaluate the long-term stability and precision of the system, [HDO] data was recorded for many days. The plot of [HDO], averaged for 64 consecutive measurements is shown in Figure 5.16. The error bars show the standard deviation in the measurements. Data shown in Figure 5.16 (a) recorded without using cavity length dithering, show higher standard deviation ( $\sim 10$  ppm). This high error in measurement was due to noise high frequency noise created by cavity mode structure. Data shown in Figure 5.16 (b) recorded with cavity length dithering shows a standard deviation of approximately 1.5 ppm. Thus, there is a considerable improvement in standard deviation when cavity length dithering is used, due to averaging out of cavity mode structure. The overall average value of measured [HDO] is 359.68 ppm and total standard deviation is  $\pm 4.41$  ppm indicating the long-term reproducibility of the measurements as 1.2%.

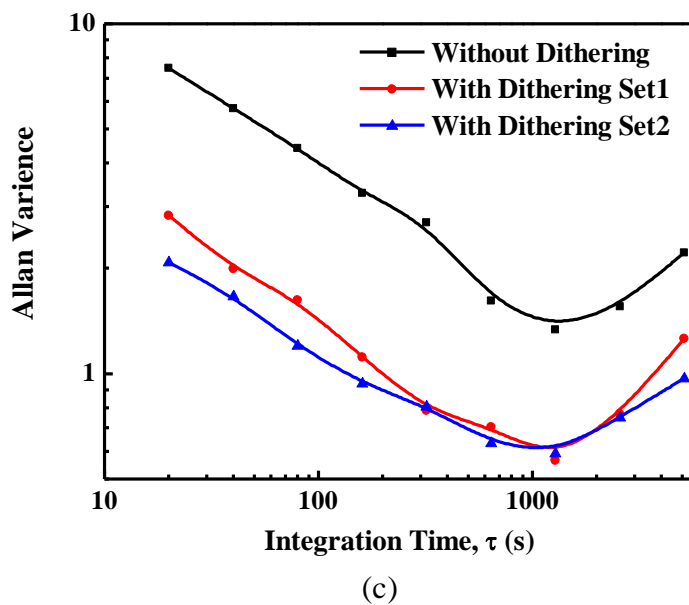
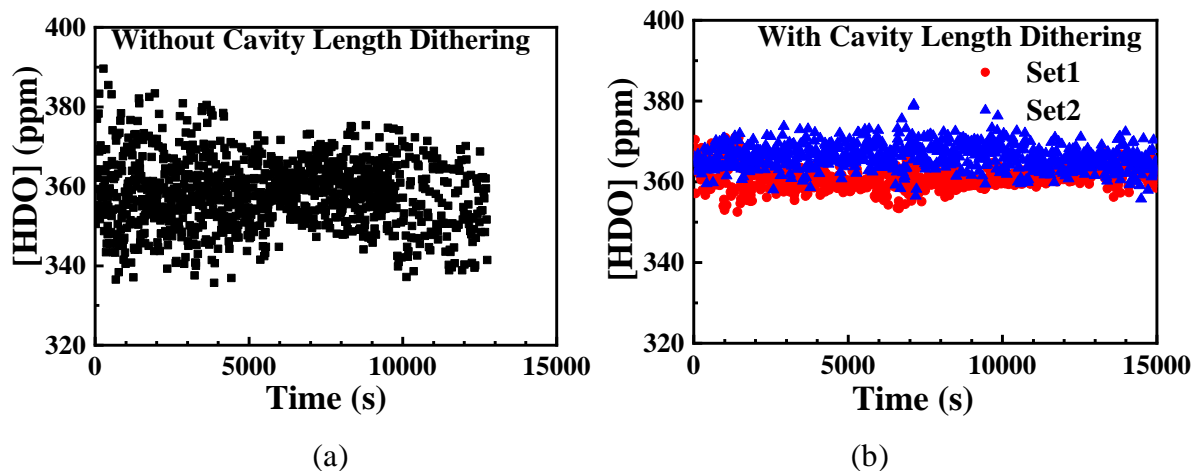


**Figure 5.14** Time series plot of recorded [HDO]; (a) Without cavity length dithering; and (b) With cavity length dithering; (c) Allan variance plots for all three datasets.

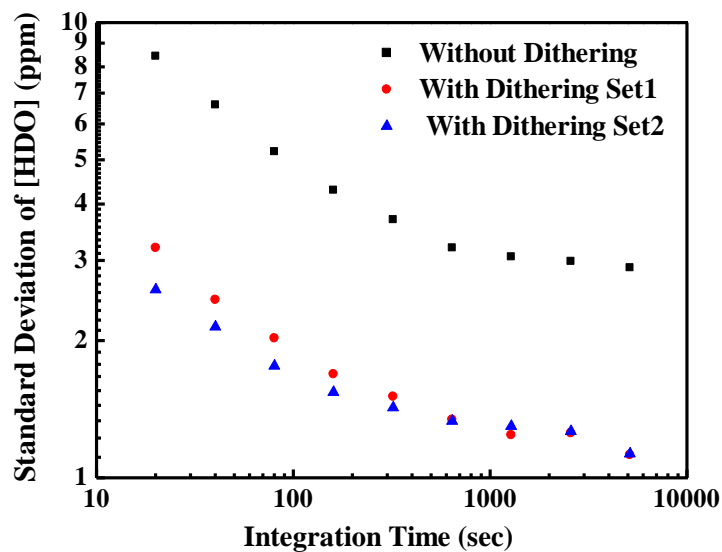


**Figure 5.15** Plot of standard deviation of measured [HDO] with integration time: with and without dithering. Plot shows considerable improvement in standard deviation when cavity length dithering is used, due to averaging out of cavity mode structure.

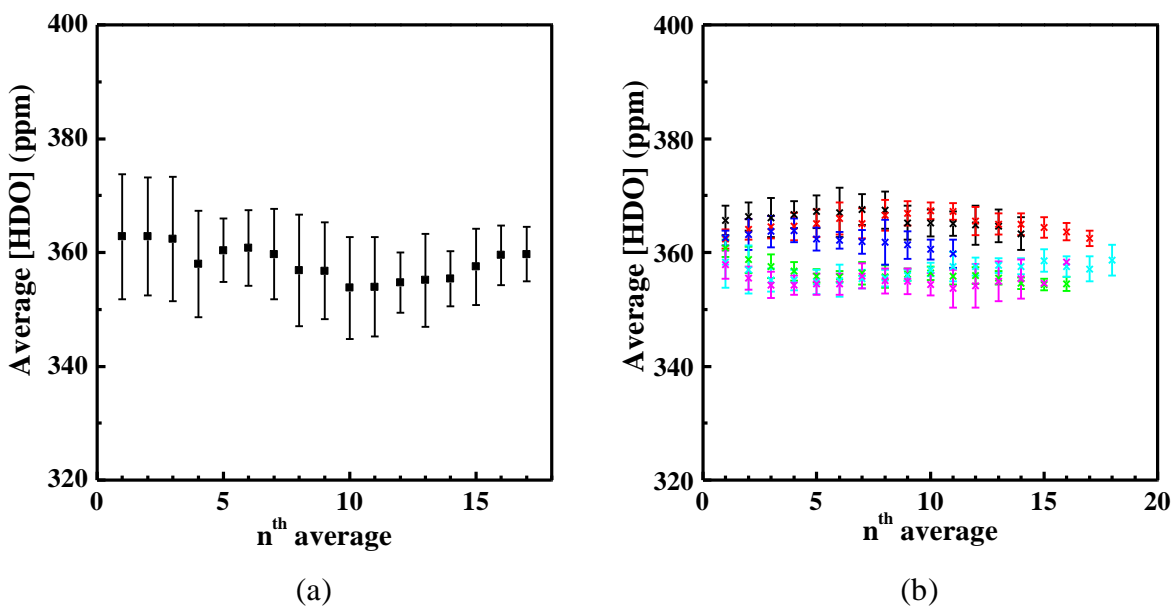


**Figure 5.16** The plot of [HDO], averaged for 64 consecutive measurements. The error bars show the standard deviation in measurements. (a) Data recorded without cavity length dithering; (b) Data recorded with cavity length dithering on six different days as shown in different colours.

## 5.6. SENSITIVITY IMPROVEMENT BY WAVELENGTH MODULATION

Wavelength modulation is a commonly used technique for improving the sensitivity of detection in LAS techniques. Hence, for further improvement in the sensitivity, possibility of using wavelength modulation was investigated. This technique is known as WM-OA-ICOS [104, 119]. The wavelength modulation was done with the sine wave generated from the internal oscillator of lock-in-amplifier (LIA), having the peak-to-peak amplitude of 4 mV and 1 kHz frequency. For the detection, second harmonic signal was recorded with LIA sensitivity set to 500 mV and the time constant set to 1 ms.

Figure 5.17 shows the transmission signal recorded with OA-ICOS, along with the WM-OA-ICOS second derivative signal recorded using LIA. Following observations were made in the recorded WM-OA-ICOS signal:

- (a) The wavelength modulation leads to broadening of absorption peaks, which is consistent with the theoretical calculations by Supplee *et. al.* [120]. Thus, the extent of overlap of already overlapped signal increases.
- (b) The major advantage of recording the second derivative signal is removal of baseline fluctuations in the transmission signal. However, in the recorded signal shown in Figure 5.17, baseline of the second derivative signal was not clearly distinguishable due to overlapping of peaks.
- (c) Negative excursion of most of the peaks is overlapping.
- (d) The positive excursion of the peaks is not proportional to the absorption signal height.
- (e) The wavelength modulation does not reduce the effect of optical noise, which is caused due to cavity mode structure.

All these complications associated with the recorded WM-OA-ICOS signal along with the nonlinear response of optical cavity, make the quantitative analysis of the concentration extremely mathematically involved and prone to errors. Hence, for this thesis, the use of wavelength modulation was not considered suitable.

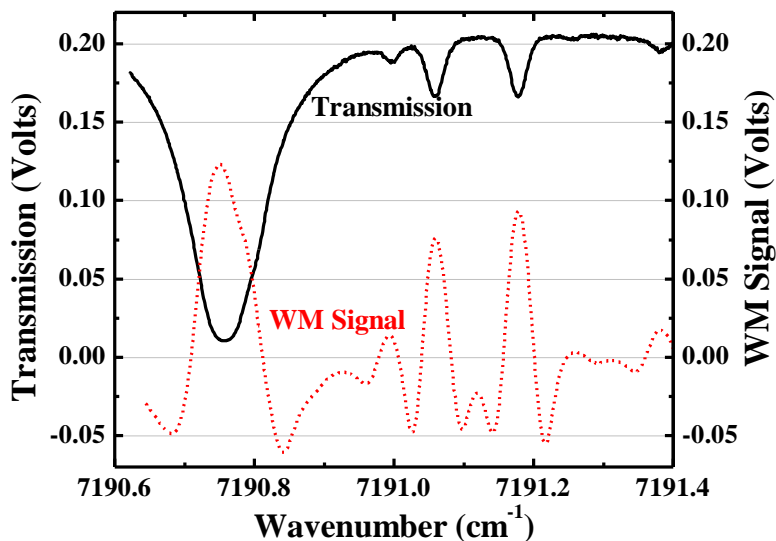


**Figure 5.17** A comparison of OA-ICOS transmission signal and WM-OA-ICOS signal recorded using a lock-in-amplifier. The WM-OA-ICOS signal shows non-proportionality of positive excursion of the peaks to the absorption signal height and broadening of peaks.

## 5.7. OPTIMIZATION OF FITTING PROCESS

The accuracy of all LAS techniques is deteriorated by many factors. These include interference fringes of optical components, background drifts and electronic white noise. The effect of these factors can be corrected by using digital signal processing methods [121]. Amongst these, suitable filtering can eliminate electronic white noise. The background drifts can be corrected by intensity

normalization of raw signal with laser intensity. The effect of interference fringes is the most difficult to correct. These interference fringes can be divided into three categories:

- (a) Fringes with frequency less than 0.1 times the halfwidth: these fringes appear as drift in the baseline. The effect of these can be corrected with appropriate baseline fitting process in time domain.
- (b) Fringes with frequency ranging from 0.1 - 4 times the halfwidth: effect of these fringes is most difficult to correct, as they indistinguishable from the signal in both the frequency and the time domain. These can be corrected by incorporating a sinusoidal etalon fringe signal in the least square fitting process. However, for successful implementation of this method the frequency of etalon fringes should be known and fixed, else fitting process becomes unstable. Another method to deal with such fringes is arithmetic elimination (or semi-parametric method) [122, 123]. However, this method is applicable for single isolated peak and cannot be applied to the spectrum consisting of multiple overlapping peaks.
- (c) Fringes with frequency greater than 4 time the halfwidth: such fringes can be eliminated by low pass filtering. The most commonly used method for spectrum analysis is Savitzky-Golay (S-G) filter. The main advantage of S-G filter is that it performs de-noising while preserving the peak shape [124, 125].

In the initial experiments reported earlier, the spectrum fitting was performed by simultaneous fitting of all absorption peaks while keeping their relative positions fixed. In this method to account for additional peak broadenings, a peak broadening parameter was used, which was assumed to be equal for all the peaks. For comparison with other fitting methods, this process is labelled as FM1.

Since the observed spectrum shows presence of etalon fringes in all three frequency ranges, the optimization for fitting process was performed, to reduce the error in estimated concentration.

To remove the high frequency fringes S-G filter with 21 window size was used. Figure 5.18 shows the reduction in high frequency etalon fringes by application of S-G filter.

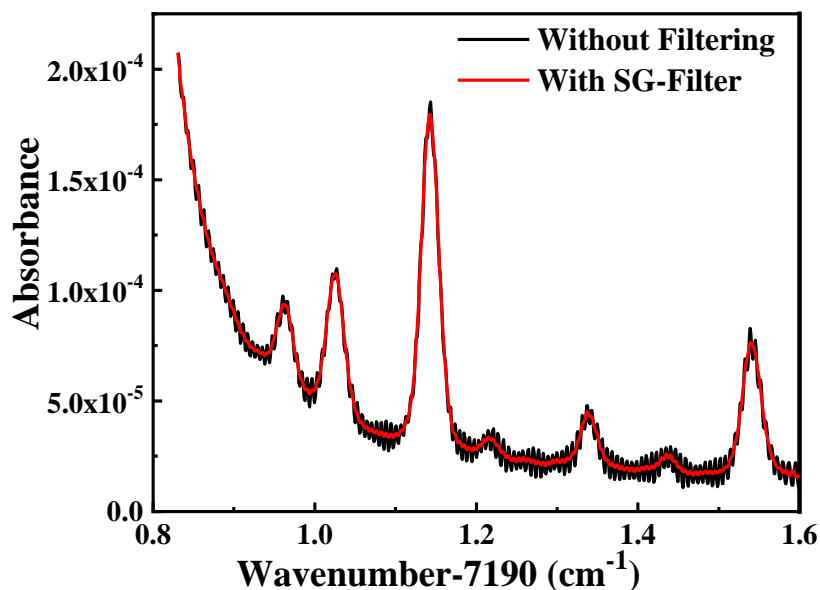


**Figure 5.18** Plot shows the acquired absorbance spectrum without any filtering and reduction of high frequency etalon fringes by using S-G filter.

In the observed spectrum, the baseline drifts due to low frequency etalon are indistinguishable from the Lorentzian wing of the strong absorption peak at  $7190.74 \text{ cm}^{-1}$ . The effect of the drift however can be seen in the residuals for the portion of spectrum between the peaks. These portions of spectra were extracted to determine the baseline drift, which was then subtracted from the spectrum. The corrected spectrum was again fitted and  $[\text{HDO}]$  was determined. This process is labelled as FM2. In another method labelled as FM3, individual peaks are extracted from the

spectrum and are fitted independently. This method also corrects the slight shift in relative peak positions which can be seen in Figure 5.19 (a).

Figure 5.19 (a) shows the comparison of curve fitting by FM1 and FM2. It was seen that for the observed spectrum, the FM1 has resulted in overestimation of [HDO]. It can be inferred that FM2 effectively removes the baseline drift due to low frequency etalon. Figure 5.19 (b) shows the comparison of fitted spectrum by FM1 and FM3. This method shows lower standard deviation in the residual and seems to be better fitting model. Table 5.5 shows the improvement in residuals with fitting methods FM2 and FM3 as compared to FM1. However, due to presence of etalon fringes in the frequency range close to half-width, each peak is distorted to some extent. Some peaks are broadened while other are narrowed, which leads to either overestimation or underestimation of concentration respectively. Hence, estimated [HDO] shows higher standard deviation with FM1 as shown in Figure 5.19 (c). Thus, it can be concluded that S-G filtering along with baseline correction (FM2) is optimum method for spectrum fitting in this case. This fitting method also results in improvement in long term reproducibility from 4.4 ppm to 3.2 ppm.

**Table 5.5** Comparison of standard deviation of residuals for all three fitting methods.

<b>Fitting Method</b>		<b>Standard Deviation in Residual</b>
<b>FM1</b>	All peaks fitted simultaneously without any correction	1.63E-06
<b>FM2</b>	Baseline correction and simultaneous fit	1.33E-06
<b>FM3</b>	Fitting to isolated peaks after baseline correction	1.07E-06

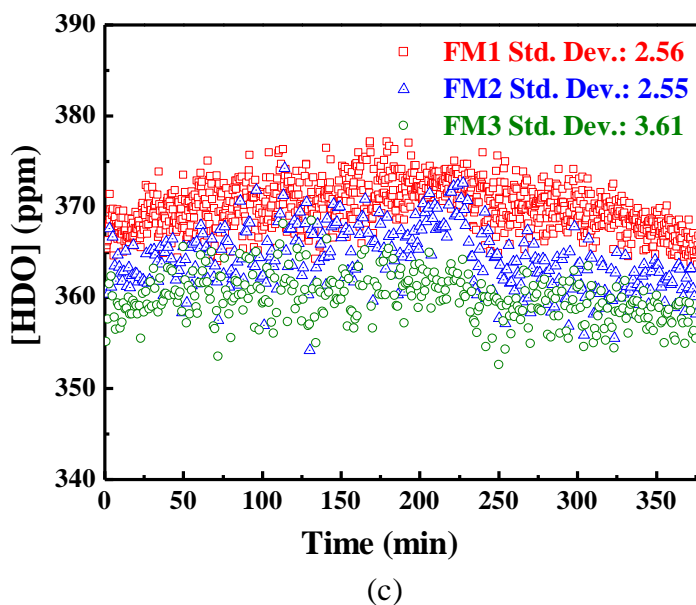
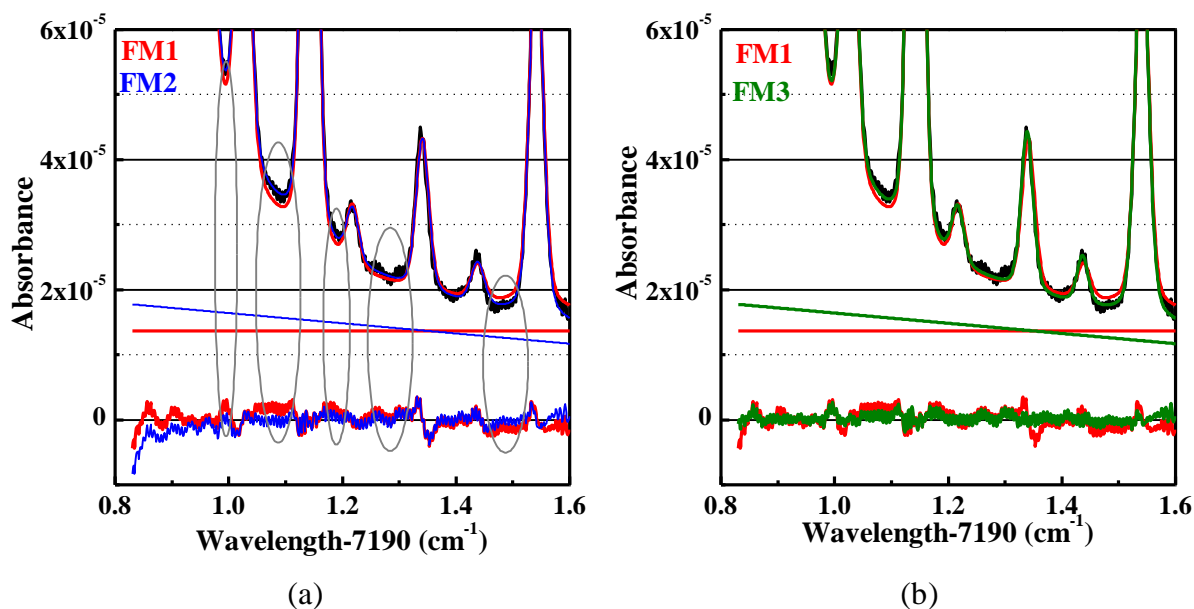


**Figure 5.19** Comparison of three fitting methods. (a) FM2 with baseline correction shows better fit compared to FM1; The effect of FM2 w.r.t. FM1 can be seen in the region between the peaks as shown by ovals. (b) FM3 leads to reduction in standard deviation in residual; (c) FM3 shows higher standard deviation in estimated [HDO]. Hence it is concluded that FM2 is better curve fitting method.

## 5.8. PERFORMANCE VALIDATION

The performance of the developed OA-ICOS based system for heavy water leak monitoring was studied by measuring the concentration of HDO in the water samples collected from different locations in Dhruva research reactor, at Bhabha Atomic Research Centre. The samples were injected in the optical cell using a syringe. For each measurement, the syringe and the cell were cleaned thoroughly with the sample itself to remove any residue of previous sample. The cell was evacuated to a pressure of  $10^{-3}$  mbar. Approximately 4  $\mu$ l of water sample was then injected into the cell through the silicon septum, creating a sample vapour pressure of approximately 12 mbar inside the cell. The resultant optical transmission signal along with the pressure and temperature of the cell were measured and recorded. The [HDO] was determined for each sample after processing the obtained signal and by curve fitting the spectrum as described in Section 5.2. An average of 64 measurements was used for determining the [HDO]. Figure 5.20 shows the plot of such measurements for seven different samples, labelled S1 to S7. The sample labelled S1 is the standard distilled water, for which the measured value of [HDO] is  $300.6 \pm 1.74$  ppm. The measured average value along with the standard deviation for other samples is also shown in this figure. The [HDO] in all the samples were found to be higher than that of normal water indicating leakage of heavy water ( $D_2O$ ) from the heat transport system of the nuclear reactor.

In order to validate the system for actual deployment in a nuclear reactor, the correlation between the measured [HDO] with the measurements obtained using other established techniques is necessary. As discussed earlier, the alternate technique used to detect heavy water leak in a nuclear reactor is based on tritium monitoring. For isotope ratio measurement of hydrogen, traditionally IRMS is used. Hence, the performance validation of system developed in this thesis is based on

the correlation of the obtained results with the data obtained using the techniques described in next subsections.

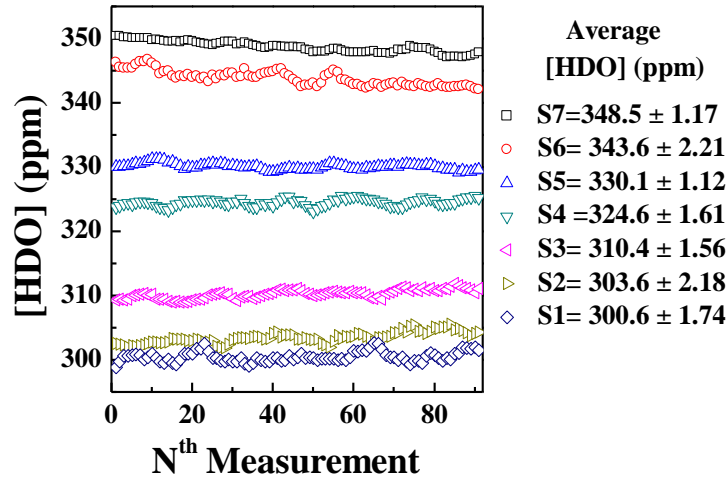


**Figure 5.20** A plot showing continuous measurement of [HDO] (100 samples) in samples labelled S1 to S7. The measured average value of [HDO] in ppm and standard deviation for each sample is shown in the figure.

### 5.8.1. Correlation with Tritium Activity using LSC

Tritium monitoring is the most sensitive method available and hence is being used in PHWRs worldwide for monitoring leaks in the heat transport system. A high level of tritium is formed due to neutron activation of deuterium in the coolant and moderator systems. Any leak in these systems is expected to result in the rise in deuterium and tritium concentrations in the surrounding light water system (e. g. secondary coolant) and in the surrounding environment. Since both the systems contain high purity heavy water, the changes in deuterium concentration and tritium concentration in the surrounding light water samples are linearly correlated. The proportionality constant between these two isotopes depends on the activity of coolant and moderator. Thus, the tritium

monitoring system is an indirect method, which is being used to estimate the losses of heavy water occurring to the surroundings.

In this thesis, the tritium concentration ( $T_\beta$ ) for all the samples was measured by an LSC. The tritium concentration in the samples is compared with the change in the deuterium concentration ( $\delta D$ ) in the samples. Here,  $\delta D$  (in mils  $\equiv$  per 1000) is obtained by comparing the [HDO] of a standard sample, using the following equation:

$$\delta D = \frac{HDO_{\text{sample}} - HDO_{\text{standard}}}{HDO_{\text{standard}}} * 1000 \quad (5.23)$$

The plot of measured  $\delta D$  using the developed system versus normalized tritium concentration measured with LSC is shown in Figure 5.21. Each sample was measured three times, and the average value was obtained. Since for the present case of Dhruva research reactor, the coolant and moderator systems are not isolated, the tritium activity was expected to be the same for both the systems. Thus, [HDO] and the  $T_\beta$  were expected to follow the same proportionality for all samples. The measured  $\delta D$  shows a linear variation with tritium concentration. The obtained correlation coefficient between  $T_\beta$  and  $\delta D$  is 0.982. This plot shows that the sensitivity of the developed system for heavy water leak monitoring is comparable to that of an LSC monitoring tritium.

Due to routine leaks in the heat transport system, there is a measurable level of  $T_\beta$  and  $\delta D$  in the reactor system. Additional leaks in the reactor system are indicated by an accompanied rise in both of them. Such leaks manifests wear and tear in the system which may develop into severe leaks if remain unattended. For the safety of the reactor and people working there, it is important to locate the leaks at the earliest. Detecting a leak location in PHWRs is a tedious and time-consuming task. Since, heavy water is used both as coolant and moderator in two isolated systems; the leaky system

can be distinguished based on the difference in tritium concentration. The difference in tritium concentrations in the coolant and moderator channels is due to difference in their volume and residence time inside the reactor core. Therefore, if the ratio of tritium to heavy water in the sample is known, it can be used to identify the system from which heavy water is leaking [126]. Thus, [HDO] measurement system along with the tritium monitors could be useful not only in determining heavy water losses but also in the diagnosis of a faulty leaking system.

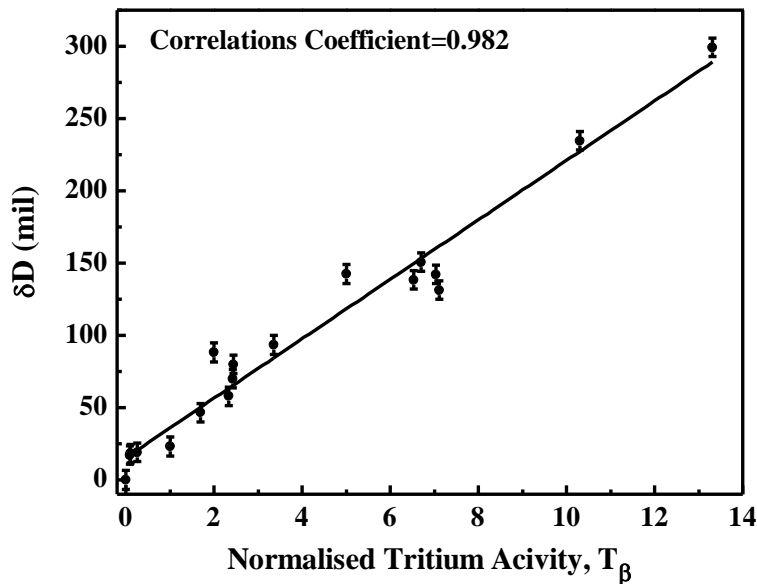


**Figure 5.21** Comparison of measured change in deuterium concentration  $\delta D$  using developed OA-ICOS system with normalised tritium concentration measured using LSC.

### 5.8.2. Correlation with D/H ratio using IRMS

IRMS is one the most sensitive techniques to measure the isotopic ratios of H, C and O which finds application in environmental science [23] (See Appendix I for more information on isotopic ratio measurement Methods). However, it is not suitable for leak monitoring system in PHWR due

to its size, cost, sample preparation, and handling considerations. Moreover, it cannot be applied for online monitoring. In this study, we have compared the results of various measurements carried out using the developed system with IRMS. This was done to cross-check the calibration of [HDO] measurement and to establish that the accuracy of our measurement is comparable to that of IRMS. The D/H ratio of all the samples obtained from Dhruva reactor was also measured with IRMS. Figure 5.22 shows the plot of correlation between [HDO] by the developed OA-ICOS and D/H ratio measurement by IRMS. The [HDO] concentration is twice the D/H ratio since only one of the H atoms is replaced by D in H<sub>2</sub>O molecule. The correlation coefficient of OA-ICOS measurements and IRMS measurement is 0.9766. The measurement sensitivity of our system is  $\pm 1.5$  ppm (for 160 sec averaging) for [HDO] in water, which is better than  $\pm 1$  ppm sensitivity in D/H ratio by the IRSM instrument.

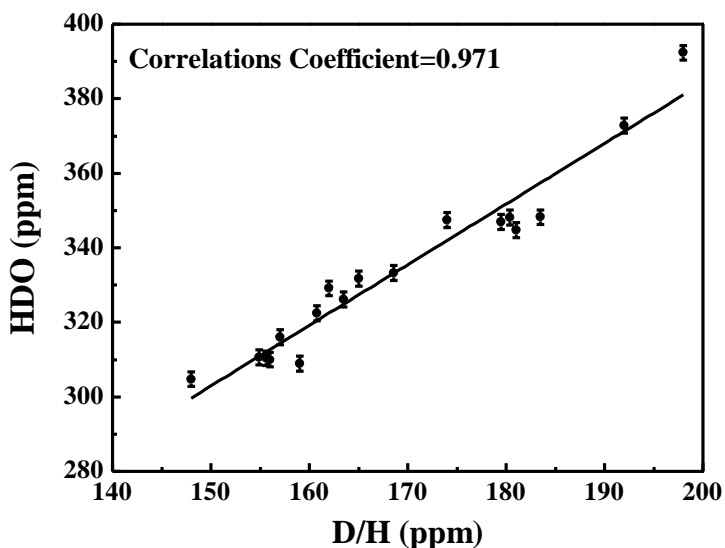


**Figure 5.22** Correlation between [HDO] by OA-ICOS and D/H ratio measurement by IRMS.

### 5.8.3. Discussions

Various samples collected at the DHRUVA reactor were analysed by three techniques viz. OA-ICOS system developed in this thesis, LSC based tritium monitors and IRMS. The measurements done using the developed system show very good correlation with the measurements done using the other two techniques. The sensitivity of developed OA-ICOS system is 1.5 ppm which is better than that of the IRMS system used in this study. A good correlation between analysis by OA-ICOS system and LSC indicates that the sensitivity of the developed system is as good as LSC. Thus, it can be concluded that the system developed in this thesis can be deployed for heavy water leak detection in PHWR with sensitivities comparable to the conventional techniques. The advantages of the present system over conventional techniques would be possibility of online real time monitoring, gamma interference free monitoring and portability.

The use of a similar system has been reported by a scientific group for heavy water leak monitoring in fuel channel closure plug in Wolsong-4 PHWR [104, 105, 110, 111]. However, the data fitting and absolute concentration determination was not performed by them. In their publications, there was no information on how the results of their measurements are correlated with other techniques being used in nuclear reactors. They have presented results of leakages only from the fuel closure plug. In this thesis, we have given the results over wider concentration range, and shown that with the presented method of signal processing and curve fitting linear calibration curves can be obtained over the entire range of measurements for 20-2280 ppm. The cross-correlations between the measurements of [HDO] by the developed system with the data obtained using the existing established techniques are presented. The technique is validated by taking sample at different places in the nuclear reactor.

## 5.9. MEASUREMENT RESULTS OF [HDO] IN AIR

The [HDO] in the laboratory air was measured using the developed system. At the time of measurement, the temperature of the laboratory was  $25.5 \pm 0.1^\circ\text{C}$  with  $50 \pm 5\%$  relative humidity. This corresponds to the fraction of water vapour in air is about 1.43 to 1.75 %. The isotopic composition of water vapour near the sea surface and in coastal areas (like Mumbai) is deficient in D/H ratio by 70 to 180 mils [127]. Hence the [HDO] in the laboratory air is expected to be 4.12 to 4.67 ppmv of air. For such small concentration measurements with sufficient SNR, the pressure inside the cell needs to be optimized. This optimization was carried out by estimating the height to width ratio of cavity absorption signal as shown in Figure 5.23. For this purpose, the maximum height to width ratio of HDO absorption peak was obtained at 100 mbar. In addition, for these measurements, the cell length was increased to 14.5 cm for improving the sensitivity.

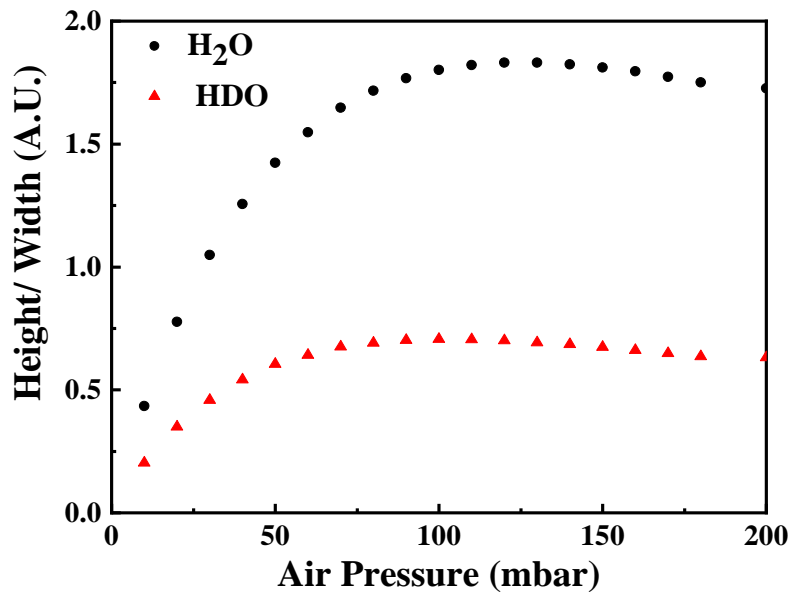


**Figure 5.23** Optimization of pressure for [HDO] measurement in air. Plot shows that maximum height to width ratio for air pressure around 110 mbar for HDO absorption peak.

For the measurements of HDO in air, the laboratory air was sampled continuously using flow through system. The pressure inside the cell was maintained at 100 mbar by controlling the inlet and outlet valves. Figure 5.24 (a) shows the observed absorption spectrum for [HDO] measurement in air. The absolute concentrations of both  $\text{H}_2^{16}\text{O}$  and HDO were obtained using area under the single pass absorption peaks. For estimation of the error in measurement, a large number of absorption signals were acquired and processed. The measured average  $\text{H}_2^{16}\text{O}$  concentration was obtained as  $1.54 \pm 0.07\%$  which is within the specified range. The measured [HDO] as obtained from individual spectra was  $4.27 \pm 0.38$  ppm, which is also within the range. The sensitivity of  $\sim 0.5$  ppm of [HDO] in air was achieved with 20 averaging.

In the above measurements, the sensitivity was mainly limited by the intensity of noise due to optical fringes in the cavity and other optical components. The effect of these can be minimized by dithering the cavity length. The effect of dithering is to average out the mode structure. The cavity length dithering is provided by piezo electric actuators. The absorption spectrum thus obtained is shown in Figure 5.24 (b). As can be seen, a considerable improvement in the SNR is observed due to averaging out cavity mode structures. The minimum detectable concentration of 45 ppbv was achieved with 16 averaging.

The sensitivity of HDO/ $\text{H}_2\text{O}$  ratio measurement and the absolute [HDO] in air was determined by performing the measurement for a longer period of time. Figure 5.25 shows the time series plot of ratio [HDO]/[ $\text{H}_2\text{O}$ ] and [HDO] in air for determining their measurement sensitivity in air. The standard deviation of plots shows that the sensitivity of ratio [HDO]/[ $\text{H}_2\text{O}$ ] measurement is 6.17 ppm and that of [HDO] in air is 113 ppbv.

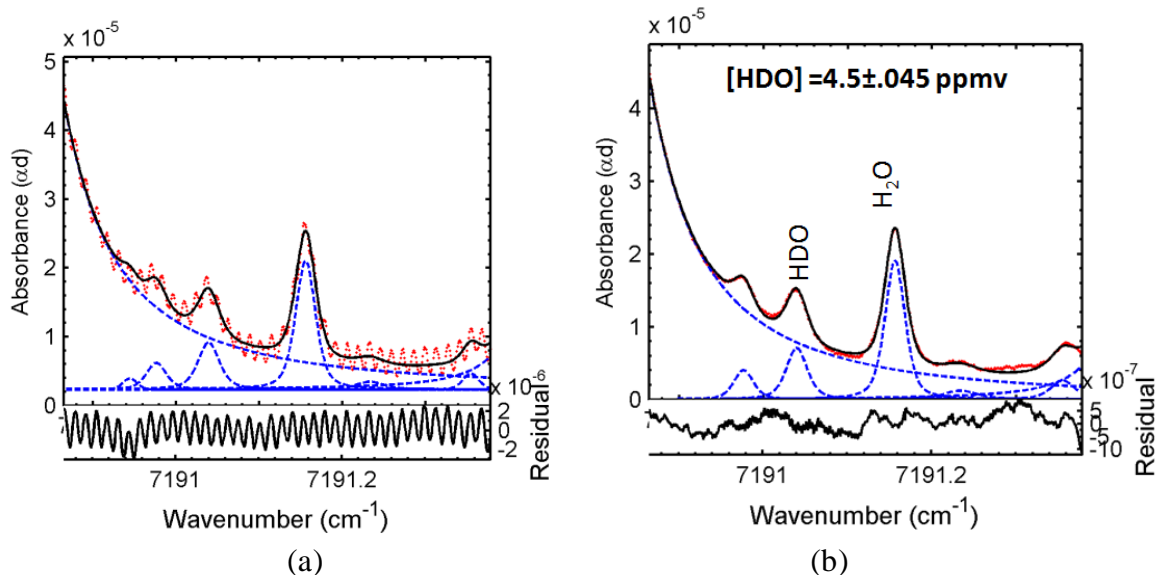


**Figure 5.24** Measurement of [HDO] in laboratory air: (a) Observed spectrum without cavity length dithering shows significant noise due to fringes; (b) Shows reduction in fringes in the observed spectrum with cavity length dithering.

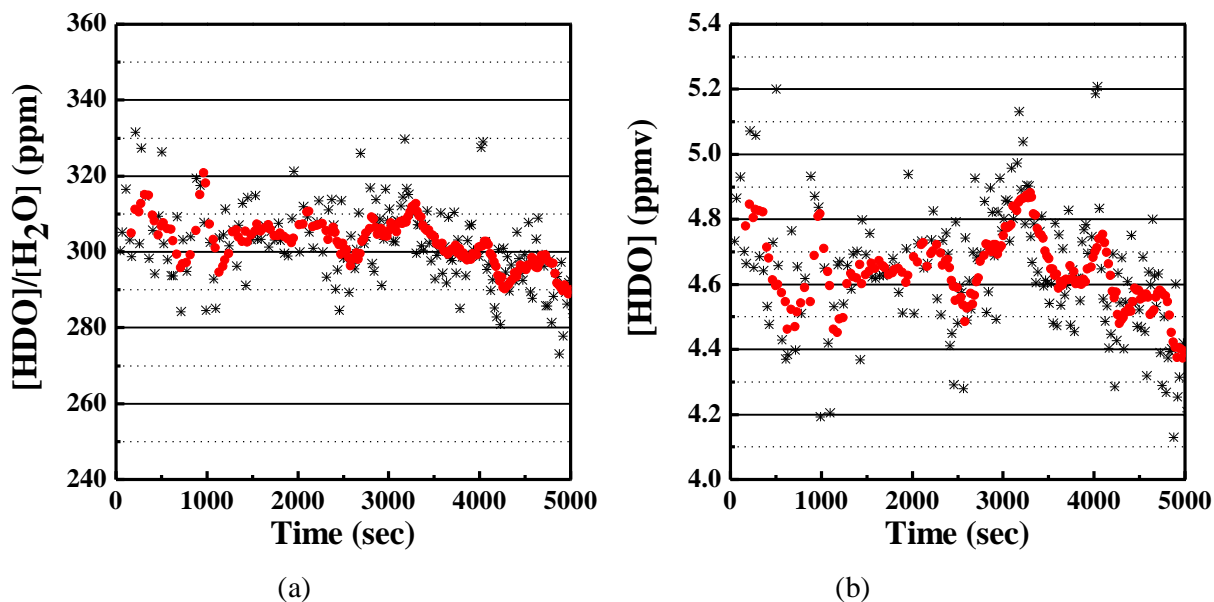


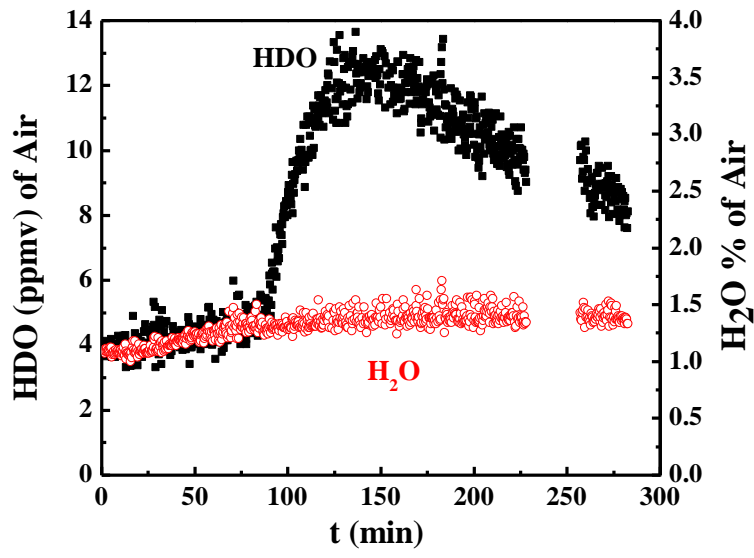
**Figure 5.25** Time series plot of (a) ratio  $[\text{HDO}]/[\text{H}_2\text{O}]$  and  $[\text{HDO}]$  in air for determining their sensitivity in air. The standard deviation of plots shows the sensitivity of ratio  $[\text{HDO}]/[\text{H}_2\text{O}]$  measurement is 6.17 ppm and that of  $[\text{HDO}]$  in air is 113 ppbv.

### **5.9.1. Measurements of HDO in Laboratory Air for Experimentally Simulated Leak Condition**

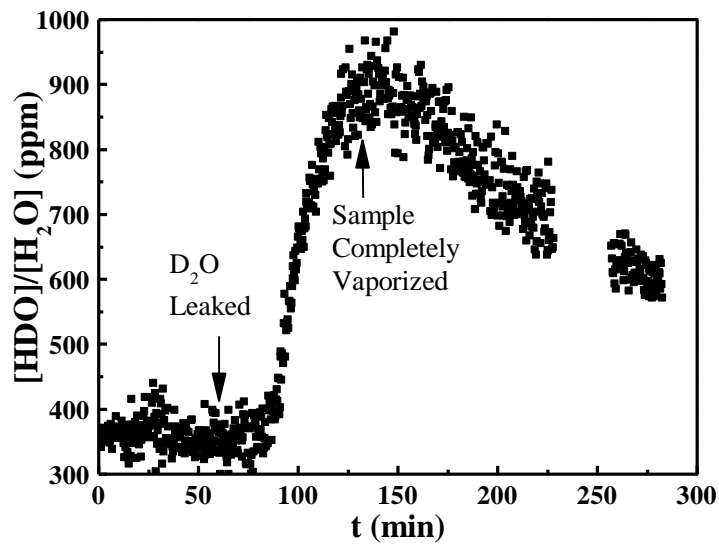
A leak condition for D<sub>2</sub>O was simulated experimentally in the laboratory; by placing 100 µl of D<sub>2</sub>O on a tissue paper at a distance of 15 cm from the inlet port. The plot of measured HDO and H<sub>2</sub>O concentrations in the laboratory air is shown in Figure 5.26 (a). Figure 5.26(b) shows the ratio of HDO to H<sub>2</sub>O concentrations. The flow of sample to the cell inlet and its circulation in the room was dependent on air circulation in the laboratory due to the air conditioning unit.

As can be seen from the plot in Figure 5.26 (b), the [HDO] initially increases due to vaporisation of D<sub>2</sub>O. Once all the heavy water is vaporised, the [HDO] decreases due to circulation of fresh air from the air conditioning unit in the room. The plot shows that 113 ppbv change in [HDO] can be detected with 16 averaging. It can be concluded that small leakages of heavy water in PHWR can be detected efficiently using the developed system as long as the wind is not blowing in the opposite direction.

Furthermore, for quantification of amount of leaked heavy water, 50 to 600 micro litres of D<sub>2</sub>O were spilled at a distance of three meters from the cell. Figure 5.27 shows that the maximum change in [HDO] in the laboratory is proportional to the amount of heavy water. For these experiments flow conditions were maintained constant. This shows that quantification of heavy water leakages in reactor can be performed with the developed instrument.



(a)



(b)

**Figure 5.26** Measurement of [HDO] in artificially created leak like situation in the laboratory. (a) Variation of concentration of HDO and H<sub>2</sub>O in air; (b) Variation of HDO content with respect to water content.

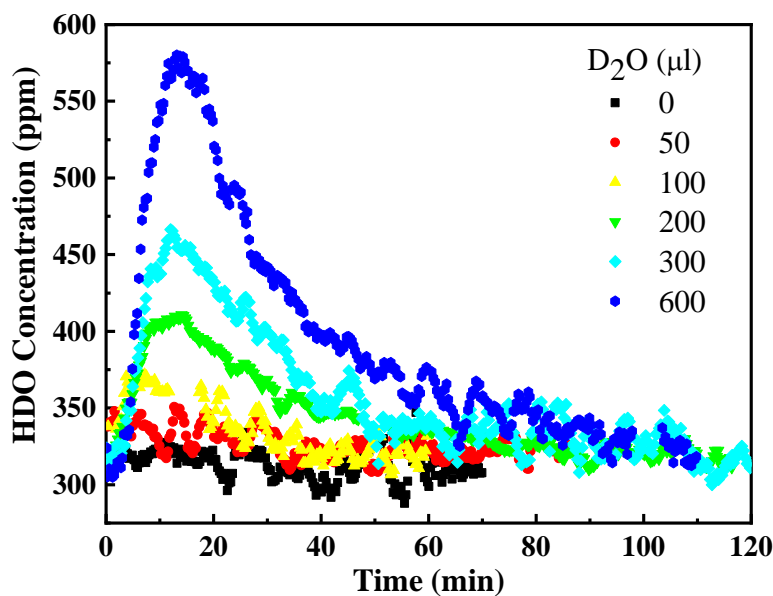


**Figure 5.27** The variation of [HDO] in air, for spillage of 50 to 600 micro litres of heavy water at distance of about 3 m from the absorption cell.

## 5.10. SUMMARY

In this Chapter, the characterization and performance evaluation of the designed and developed HDO detection system has been presented. In Section 5.1, the relation between the cavity output and the absorbance per pass has been derived. The cavity gain and path length enhancement for OA-ICOS system have been derived and it has been shown that both are non-linear function of the absorbance. A spectrum fitting algorithm has been devised to take into account the cavity gain non linearity and overlapping peaks. The concentration of HDO and H<sub>2</sub><sup>16</sup>O molecules has been computed from the area under the respective absorption peaks using known spectral constants at measured pressure and temperature. The factors effecting the concentration measurement including isotopic fractionation, temperature, mirror reflectivity, and the discrepancies in compiled

databases have been discussed in this chapter. The effect of all these factors was studied and incorporated in the data fitting process.

The performance evaluation and characterization of developed system has been presented. Firstly, the mirrors reflectivity has been measured to be 99.92% which results in an effective path length 168.75 m for the cell length of 13.5 cm. Subsequently, the measured [HDO] has been calibrated with respect to the standard samples ranging from 20 ppm to 2280 ppm and a linear calibration curve has been obtained. The averaging has been used for the improvement of the measurement sensitivity. The limit on averaging has been determined to be 64 by plotting its Allan variance. It has been realized that the major limiting factor in achieving sensitivity is the baseline fluctuation due to cavity mode noise which have been removed by cavity length dithering. The precision of the system has been evaluated by measuring the [HDO] for several days. From these measurements, it has established that the precision of the measurement is  $\pm 4.4$  ppm, which is equivalent to  $\pm 1.2$  % error. The validation of the results has been performed by comparing them with well-established techniques such as tritium activity measurements using LSC and D/H ratio measurement by IRMS. The correlation coefficient of the [HDO] is 0.982 and 0.971 for LSC and IRMS respectively. The developed system has also been used to measure [HDO] in the laboratory air. The fraction of measured [HDO] is  $4.5 \pm 0.045$  ppmv, which is within the expected range. The sensitivity of absolute [HDO] in air has been evaluated to be  $\pm 113$  ppbv, while the sensitivity of [HDO] to [H<sub>2</sub>O] ratio is  $\pm 6.17$  ppm

## CHAPTER 6

### CONCLUSIONS AND FUTURE SCOPE

---

The detection of heavy water leak is very crucial for the safety of nuclear reactors and personal. For this purpose, an experimental system based on OA-ICOS technique has been designed and developed. The application of this system for the measurement of heavy water concentration in water samples and in air samples has been demonstrated through [HDO] measurements. The measured data was validated by comparison with the data obtained with established techniques such as LSC and IRMS. The highlights and achievements of the work carried out in this thesis are as follows:

- An effective path length of 168.75 and 181.25 meters has been achieved for the cell lengths of 13.5 cm (for water samples) and 14.5 cm (for air samples) respectively, using the end mirror of 99.92 % reflectivity.
- The concept of cavity gain variation with per pass absorbance in the cell has been introduced and it is shown to be an important factor for obtaining linear calibration curve for wide concentration range.
- The factors affecting the measurement accuracy such as temperature, isotope fractionation, and reflectivity of mirrors have been studied in detail.
- A signal processing algorithm has been developed which has the following features:
  - Takes care of various factors that affect the measurement accuracy.

- Each peak is individually fitted to Voigt peak profile to account for overlapping peaks and Lorentzian wing of strong absorption.
- The method and the fitting algorithm have been validated by measurements using samples with known [HDO] ranging from 20 ppm to 2280 ppm.
- The estimated [HDO] obtained using the developed algorithm does not show any effect of gain non-linearity and a linear calibration curve has been obtained over the entire range of concentrations.
- Optimum integration time for averaging is evaluated to be 1280 sec (i.e. = 21 minutes) using Allan variance plot. This corresponds to averaging over 64 individual measurements. While reasonably sufficient sensitivity  $\pm 1.5$  ppm can be obtained by integrating for 160 seconds.
- The sensitivity of [HDO] measurement in water samples has been observed to be:
  - $\pm 10$  ppm without cavity length dithering.
  - $\pm 1.5$  ppm with cavity length dithering and 160 sec averaging.
  - $\pm 1.2$  ppm with cavity length dithering and 1280 sec averaging.
- The precision of the [HDO] measurement due to long term instabilities for water samples has been evaluated to be  $\pm 3.2$  ppm, which is equivalent to  $\pm 1$  % error for natural water sample.
- Very good correlation with established techniques such as LSC and IRMS has been obtained:
  - The correlation coefficient between measured D/H ratio using mass spectrometer (IRMS) and [HDO] is 0.971 while the sensitivity of both measurements is comparable.

- The correlation coefficient between tritium activity (by LSC) and [HDO] is 0.982. Since the measurements show good correlation and comparable sensitivity with LSC, the developed system can be successfully employed in PHWRs for heavy water leak monitoring.
- The minimum detectable [HDO] of 45 ppbv and the sensitivity of 113 ppbv of HDO fraction in air is achieved, which is sufficient for the detection of minor leakages in PHWRs.

**The contribution of this thesis to the field is as follows:**

In this thesis, design and development of trace gas detection system based on OA-ICOS technique is presented. The system was developed from the first principle for the application in PHWRs for monitoring heavy water leaks. Such systems are not commercially available and the technique is not well established. The challenges faced and the difficulties involved in implementation of such a system have been addressed in this thesis. The method of analysis has been presented in detail and an algorithm is established to derive the concentrations from the acquired signals. The factors effecting isotopic concentration of water have been studied theoretically as well as experimentally. The experimental results are found to be in agreement with the presented theory. A detailed study on quantization of laser spectroscopic based trace HDO detection system for application of to heavy water leak monitoring has been presented for first time.

**Applications and future scope of the work:**

Although, the results are focused on measurement of [HDO], concentration of other isotopologues ( $\text{H}_2^{18}\text{O}$ ,  $\text{H}_2^{17}\text{O}$ ) can also be calculated from the observed spectra. The data processing and curve fitting methodology presented is general and can be used for concentration measurement of other

gases or absorption peaks as well. The demonstrated system has sufficient sensitivity for [HDO] measurement in air for the application in PHWR heavy water leak detection system. The system can also be used in the initial stages of heavy water processing plants.

Although the system is demonstrated for heavy water leak monitoring, similar system can be used for monitoring other trace gases. There are many such applications in nuclear field such as detection of SF<sub>6</sub> in accelerators, HF and UF<sub>6</sub> in uranium enrichment facilities, detection of H<sub>2</sub>S in heavy water production units. In addition, such instrument can find application in breath monitoring for diagnostics, NO<sub>x</sub> and SO<sub>x</sub> monitoring for pollution control, etc.

# **APPENDIX I : AVAILABLE TECHNIQUES FOR HEAVY WATER LEAK MONITORING AND ISOTOPIC RATIO MEASUREMENTS**

## **I.1 Heavy Water Leak Monitoring**

In the pressurized heavy water reactor (PHWR), heavy water leakages may occur to the light water system or to the atmosphere. A few techniques are currently being used for monitoring such heavy water leaks. These techniques are either based on physical sensing or on monitoring the radioactivity due to activation of coolant and moderator by neutron interaction. Details of some of the techniques are presented below:

### **I.1.1 Dew Point Monitor**

Dew point monitors are used to detect the pressure tube failures in PHWRs. The inter space between the coolant tube (also called pressure tube, PT) and calandria tube (CT) is filled with carbon dioxide. The CO<sub>2</sub> serves as a thermal isolation between CT and PT. This CO<sub>2</sub> is recirculated to monitor pressure tube leak by monitoring dew point of the carbon dioxide. The dew point of this circulating high purity CO<sub>2</sub> is maintained at -20° C. A rise in the dew point to -5° C indicates leak in one or more of the coolant tubes. The annulus gas tubes from individual channels are grouped into several strings. The larger groups are further divided in smaller sub-groups. The process of elimination identifies the sub group containing the leaky tube, isolating one group at a time [11].

The use of CO<sub>2</sub> as annulus gas for leak monitoring has some limitations. The main problem is diffusion of Deuterium, which is dissociated from heavy water due to radiation, from PT to the

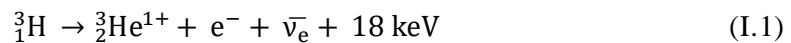
annulus gas. This Deuterium reacts with CO<sub>2</sub> producing D<sub>2</sub>O and CO. Heavy water formed due to this reaction increase the dew point of annulus gas. Hence, the sensitivity of dew point meters for detection of heavy water leakage is compromised.

### **I.1.2 Beetle Detectors**

Beetle is a moisture collecting and detecting instrument. Beetles detectors consist of two electrodes positioned in collection pots below the susceptible joints of heavy water systems. When pots fill with heavy water, the electrodes will be shorted and an alarm is generated. The beetles have advantage of being reliable and they are easy to maintain. However, they cannot detect minor leaks due to instantaneous evaporation of heavy water, on account of high temperature and pressure of coolant inside the pressure tubes.

### **I.1.3 Tritium Activity Monitors**

In the heavy water systems, Tritium is generated from neutron activation of the Deuterium ( ${}^2_1\text{D} + n \rightarrow {}^3_1\text{T}$ ). Thus, small amount of leakages in heavy water systems causes release of tritium to the reactor environment. Tritium is a beta emitter; it decays to Helium-3 ( ${}^3\text{He}$ ) as per the following equation;



The 18 keV energy released in the process is shared by the emitted particles and the average energy of the emitted beta particle is 5.7 keV. The half-life of tritium is 12.3 years. Knowing the Tritium concentration in air or light water allows an estimation of heavy water. The measurement of tritium

needs elaborates rigorous and time-consuming procedures, since an extremely low level of activity is measured. Thus, enrichment of tritium as well as conversion into suitable form is required before measurement is necessary. In addition, presence of  $^{41}\text{Ar}$  (Argon-41) and fission gas interfere with the activity measurement. Some of the tritium activity measurement methods are described below.

#### I.1.3.1 Scintillation Detectors

##### a) Liquid Scintillation Counter (LSC)

The heavy water leak monitoring to the atmosphere and to the light water cooling systems is usually based on tritium beta activity monitoring by LSC [128]. For atmospheric leaks, spot samples at various locations are collected manually using bubblers, cold strips and adsorption in a desiccant. For light water cooling system, grab samples are obtained manually. The samples are analysed for tritium activity by LSC. The sample is mixed with a solvent and liquid scintillator (known as scintillation cocktail). This cocktail is placed in a transparent vial i.e. loaded into LSC. The  $\beta$  particle transfers its energy to scintillating molecules, which produces a burst of photons that are detected by a photomultiplier tube (PMT). The intensity of pulse is proportional to the energy of emitted  $\beta$  particle. The activity of sample is obtained by counting number of resultant photons burst in particular energy range. Thus, the LSC can discriminate against interfering radioactive noble gases. For atmospheric samples, the sensitivity achieved with direct condensation system is around  $0.001 \mu\text{Ci}/\text{m}^3$  whereas with bubbler system it is  $0.1 \mu\text{Ci}/\text{m}^3$ . The LSC gives high sensitivity; however, it is not suitable for routine continuous monitoring as it involves delay due to sample collection, preparation and counting [128].

## b) Plastic Scintillation

Plastic scintillators are used for continuous monitoring of tritium in process water or secondary cooling systems [129]. The detector consists of about 6 numbers of 6  $\mu\text{m}$  thick porous films of plastic scintillator material packed into a cell, having total surface area of  $3000\text{ cm}^2$ . The flow cell is optically coupled to two photomultiplier tubes on the opposite faces for the measurement in coincidence mode. The sample should be filtered with granular type of activated charcoal and filter papers to avoid reduction in sensitivity due to deposition of particles. A bubbler system is used to remove the interference due to chemiluminescence from the dissolved radioactive gases. The sensitivity of this system for tritiated water is  $3.7\text{ kBq/L}$  ( $0.1\text{ }\mu\text{Ci/L}$ ). However, the detector has limited lifespan.

### I.1.3.2 Gas Filled Ionization Detector

The gas filled detectors consists of a volume of gas filled between two cylindrical electrodes, with a voltage applied between them. Ionizing radiation produces ion pairs in the gas. Positive ions are attracted towards the outer wall (cathode) while negative ions and electrons are attracted towards inner wire (anode).

Ionization chambers operate in linear region at lower voltage and the ionization produced is internally amplified and collected as current. The current in the ionization chamber is proportional to the activity and independent of energy of  $\beta$  particle. Flow-through type ionization chambers are widely used for continuous monitoring of tritium in air. The sensitivity limitation for ionization chambers is due to the sensitivity of electrometer amplifier and volume of the chamber. The background gamma radiation and other radioactive noble gases also interfere in tritium

measurement. Hence, various designs for compensation were made such as Dual signal subtractive methods without tritium removal and Dual-chamber subtractive method. Sensitivity of these instruments is about  $1 \mu\text{Ci}/\text{m}^3$  to  $100 \text{pCi}/\text{m}^3$  with a 60 second time constant. These systems are large and complex [130].

The proportional counters operate at higher voltage compared to ionization chambers. The acceleration due to higher field results in production of secondary electrons. Thus, each ion pair produces an avalanche and current is proportional to energy of ionizing particle. For Tritium measurement, the central proportional counter is surrounded by a guard ring of Geiger Muller counters (G.M. counters). They are separated by a double gridded wall for providing with field free volume. The gas flows through both the central chamber and the guard ring chamber. Since G.M. counter are insensitive to tritium, the coincidence circuit permits a measure of the concentration of the contaminant gas. The anticoincidence circuit discriminates tritium from higher energy betas and gammas. The instrument is fairly sensitive, has sensitivity of about  $0.01 \mu\text{Ci}/\text{m}^3$  in 100 s. Gamma background can also be electronically discriminated, eliminating the need for compensation detectors [128].

The major disadvantage of gas filled detectors is the need and cost of a counting gas which is either methane or very pure natural gas. Another disadvantage is the size. Presence of interfering gaseous radionuclides like noble gases in the reactor environment further reduces the sensitivity of measurement of tritium in air in continuous online monitoring.

#### **I.1.4 O-19 Monitor**

The online O-19 monitors are used for detecting coolant leakage due to heat exchanger tube failure in PHWRs [131]. The instrument performs heavy water leak detection by continuously monitoring any traces of  $^{19}\text{O}$  activity in the secondary process water coolant stream at the heat exchanger outlet.  $^{19}\text{O}$  has a half-life of 26.92 seconds and it transforms to  $^{19}\text{F}$  by  $\beta$  decay while emitting gamma photons of energy 197 keV and 1.357 MeV, as shown below:



$^{19}\text{O}$  monitor consists of sodium iodide scintillator mounted on a photomultiplier tube. To achieve better discrimination against plant background radiation, it measures the higher energy (1.357 MeV)  $\gamma$ -photons for heavy water leak detection. The use these detectors is limited to heat exchangers due to the interference caused by gamma radiation of other radio nuclides in reactor environment.

## **I.2 Isotope (D/H) Ratio Mass Spectrometry (IRMS) Technique**

The accurate measurement of isotope abundance ratio is an important tool in wide variety of research applications. Specifically isotopic ratio measurement of water finds applications in the fields like forensic science, paleoclimatology, hydrology and heavy water production, heavy water leak monitoring in the nuclear reactors, etc., [18, 23, 48, 85, 132, 133]. The detection of trace level of isotopically substituted water molecules has always been challenging due to the requirements of instrumentation with high sophistication and high sensitivity. IRMS is commonly used for precise measurement of isotopic ratio, a brief introduction to it is given below.

There are five main sections of an IRMS instrument: a sample introduction system, an electron ionization source, a magnetic sector analyser, a Faraday-collector detector array, and a computer-controlled data acquisition system. In IRMS instrument, the sample is first ionized, then the ions are accelerated by a potential in kilo-volt range. The resulting stream of ions is separated based on  $m/z$  ratio in a magnetic sector. The beams with lighter ions bend at a smaller radius than beams with heavier ions. The separated ion beams current of each ion beam is then measured using “Faraday cups” or multiplier detectors. The conventional IRMS technique has advantages such as high throughput and high precision for gaseous samples.

For many years, isotope analysis of water has been performed by IRMS exclusively. However, due to sticky and condensable nature of water molecules, it cannot be directly introduced into the mass spectrometer. Liquid water needs to be converted to hydrogen for analysis of  $\delta D$  by reduction with hot ( $\sim 800^\circ C$ ) metals (i.e., uranium, zinc, or chromium). In continuous flow mode, high temperature pyrolysis ( $>1050^\circ C$ ) is used. This conversion is the limiting factor in achieving high accuracy [18]. The main reasons for use of IRMS for isotopic analysis of water so many years are the high-precision and accurate isotope measurements provided by it. However, it is expensive, have high operational costs, and require a relatively large space in climate-controlled laboratories. Field operation with direct in situ analysis of water samples is not possible.

## APPENDIX II: PROPERTIES OF OPTICAL CAVITY

The high finesse optical cavities are constituted by two high reflectivity mirrors; they are also known as optical resonators. Their use in LAS is based on increase in effective absorption path length by trapping light between two mirrors, as the trapped photons perform large number of round trips in probed medium. The properties of such cavities have been extensively studied based on both geometric optics as well as wave analysis of electromagnetic radiation. The important results pertaining to their use in spectroscopic techniques are summarized in following sections.

### II.1 Cavity Modes

Electric field of a monochromatic wave is defined by Helmholtz Equation [134, 135]:

$$\nabla^2 E - \frac{1}{c^2} \frac{\partial^2 E}{\partial t^2} = 0 \quad (\text{II.1})$$

With solution of form:

$$E(x, y, z, t) = \psi(x, y, z)e^{i\omega t} \quad (\text{II.2})$$

where  $\psi$  is time-independent part and represent intensity distribution of the beam, for a paraxial wave travelling in z direction, it is represented by:

$$\psi = f(x, y, z)e^{-i\kappa z} \quad (\text{II.3})$$

where  $\lambda$  is wavelength of propagating wave,  $\kappa=2\pi/\lambda$  is propagation constant. Thus, the Helmholtz equation takes the form:

$$\frac{\partial^2 f}{\partial x^2} + \frac{\partial^2 f}{\partial y^2} - 2i\kappa \frac{\partial f}{\partial z} = 0 \quad (\text{II.4})$$

A trial solution for wave propagation bounded by two mirrors is given by:

$$f(x, y, z) = \exp\left[-i\left(P_z + \frac{\kappa}{2q_z} r^2\right)\right] \quad (\text{II.5})$$

where  $r^2 = x^2 + y^2$ .  $P_z$  represents a phase shift factor and  $q_z$  is known as the beam parameter. The expression of  $P_z$  and  $q_z$  is obtained by satisfying the boundary conditions for optical cavity.

### II.1.1 Fundamental Mode

Fundamental (or 0<sup>th</sup> order) solution for a cavity formed by two infinite mirrors facing each other placed perpendicular to  $z$  –axis is of form:

$$f(r, z) = G(z)e^{-r^2\left(\frac{1}{\omega_z^2} + \frac{i\kappa}{2\Re_z}\right)} \quad (\text{II.6})$$

Thus 
$$E(r, z, t) = \frac{\omega_z}{\omega_{z0}} e^{i\omega t} e^{-i\{\kappa z - \phi\}} e^{-r^2\left(\frac{1}{\omega_z^2} + \frac{i\kappa}{2\Re_z}\right)} \quad (\text{II.7})$$

where 
$$\phi = \tan^{-1} \frac{\lambda z}{\pi \omega_z^2} \quad (\text{II.8})$$

This represents a Gaussian wave, with a complex beam parameter, is defined as:

$$\frac{1}{q_z} = \frac{1}{\Re_z} - i \frac{\lambda}{\pi \omega_z^2} \quad (\text{II.9})$$

where,  $\omega_z$  is beam radius and  $\Re_z$  is radius of curvature of the beam at location  $z$ . For an optical cavity these quantities are given by the following equations:

$$\omega_z^2 = \omega_{z0}^2 \sqrt{1 + \left(\frac{z - z_0}{z_R}\right)^2} \quad (\text{II.10})$$

and 
$$\mathfrak{R}_z = (z - z_0) \left[ 1 + \left( \frac{z_R}{z - z_0} \right)^2 \right] \quad (\text{II.11})$$

with 
$$z_R = \frac{\pi \omega_{z_0}^2}{\lambda} \quad (\text{II.12})$$

The beam radius has smallest value at beam waist, at  $z=z_0$  where the radius of beam is equal to  $\omega_{z_0}$ . For a stable mode in the cavity, the Gaussian beam should satisfy the boundary conditions; i.e. radius of curvature of the beam at mirrors should be equal to the radius of curvature of mirrors and field distribution should repeat itself after every round trip for stable beam propagation. For a cavity with two spherical mirrors having radius of curvature  $\mathfrak{R}_{z_1}$  and  $\mathfrak{R}_{z_2}$  with a spacing 'd' between the mirrors, by substituting these conditions in equations (II.10) to (II.12) one obtains, an expression of beam waist,  $\omega_{z_0}$ :

$$\omega_{z_0}^2 = \frac{\lambda d}{\pi} \sqrt{\frac{(1 - g_1 g_2) g_1 g_2}{(g_1 + g_2 - 2g_1 g_2)^2}} \quad (\text{II.13})$$

where 
$$g_1 = 1 - \frac{d}{\mathfrak{R}_1}, \quad g_2 = 1 - \frac{d}{\mathfrak{R}_2} \quad (\text{II.14})$$

If we denote  $\omega_{z_{1,2}}$  as beam radius of two mirrors with ROC  $\mathfrak{R}_{z_{1,2}}$  located at  $z_{1,2}$  then,

$$\omega_{z_{1,2}}^2 = \frac{\lambda d}{\pi} \sqrt{\frac{g_{2,1}}{g_{1,2}(1 - g_1 g_2)}} \quad (\text{II.15})$$

$$z_1 - z_0 = \frac{d g_2}{g_1 + g_2} \quad \text{and} \quad z_2 = z_1 + d \quad (\text{II.16})$$

For the above analysis to be valid  $\omega_{z_0}$  and  $\omega_{z_{1,2}}$ , should be positive real numbers. Thus, for the existence of stable Gaussian mode we must have:

$$0 \leq g_1 g_2 \leq 1 \quad (\text{II.17})$$

This condition is referred to as stability condition.

### II.1.2 Higher Order Modes

In addition to, above fundamental solution, there exists an infinite set of solutions which satisfy the equation (II.4). For these modes, transverse field distribution of the resonator modes is given by Eigen functions of the differential equation (II.4). For finite mirrors with circular aperture the trail solution is of form:

$$f_{pl}(r, z) = \left( \frac{r\sqrt{2}}{\omega_z} \right)^l L_p \left( \frac{2r^2}{\omega_z^2} \right) \exp \left[ -i \left( P_z + \frac{\kappa r^2}{2q_z} + l\phi \right) \right] \quad (\text{II.18})$$

where  $L_p^l$  is generalized Lagurre Polynomial,  $\phi$  is phase factor for the cylindrically symmetric modes,  $p$  is number of radial nodes and  $l$  is number of angular nodes. These solutions are known as the transverse modes (or spatial modes) of the cavity resulting in self-reproducing field distributions of the output beam. Figure II.1 shows the plot of  $f_{pl}$  for few lower modes. The beam parameters  $\omega_z$  and  $\mathfrak{R}_z$  are the same for all cylindrical modes.

The phase factor for the transverse modes is defined as:

$$\phi(p, l, z) = (2p + l + 1) \tan^{-1} \left( \frac{\lambda z}{\pi \omega_{z0}^2} \right) \quad (\text{II.19})$$

Although these equations represent a set of infinite solutions, the appearance of higher order modes is limited by the physical dimensions of the system.

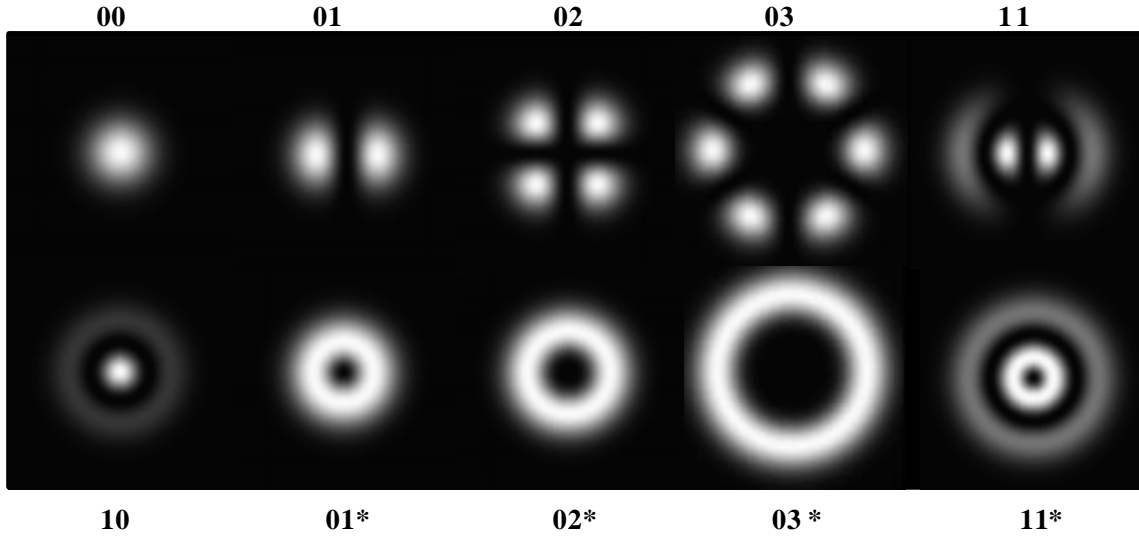


**Figure II.1** Plot of Laguerre-Gaussian modes of an optical cavity with spherical end mirrors having circular aperture [136].

## II.2 Spectral Properties of a Cavity

The laser beam inside the resonators travels to and fro; hence it forms the axial standing wave pattern. The resonances occur when the phase shift after one round trip is multiple of  $2\pi$ . For symmetric cavities it translates to a phase shift as multiple of  $\pi$  at each mirror. Using equations (II.11) and (II.19) this condition can be written as:

$$\kappa d - 2(2p + l + 1)\tan^{-1}\left(\frac{\lambda d}{2\pi\omega_{z0}^2}\right) = \pi(q + 1) \quad (\text{II.20})$$

where  $q$  is number of nodes in axial standing wave pattern. These are called cavity's longitudinal modes. The frequency spacing between two consecutive longitudinal modes is also known as free spectral range (FSR) of the cavity and is given by:

$$\text{FSR} = \frac{c}{2d} \quad (\text{II.21})$$

The frequency of transverse modes is shifted from the frequency of longitudinal modes by a small amount. For a cylindrically symmetric cavity, the resonant cavity modes are designated by  $TEM_{plq}$  having resonant frequencies:

$$\nu_{plq} = \frac{c}{2d} \left( q + \frac{\phi_{pl}}{2\pi} \right) \quad (\text{II.22})$$

When a laser beam is coupled to a cavity, the transmitted laser intensity depends on modes to which the power is coupled. If the wavelength of laser is scanned various modes appears as comb in the transmitted intensity. When a Gaussian beam is mode-matched to the  $TEM_{00q}$  mode of the cavity with coupling efficiency = 1 (in ideal case). Under this assumption, the resonator behaves as a Fabri-Parot etalon consisting of two mirrors with high reflectivity,  $R_m$  and transmission,  $T_m = 1 - R_m$ . The portion of the light transmitted into the cavity bounces back and forth. While a small portion of trapped intensity is lost on every reflection at the mirror, the total field transmitted of an empty cavity  $E_{out}$  is given by phasor sum of transmitted field on each reflection at the rear mirror. The transmission intensity of cavity is an Airy function.

$$T_{00q} = \frac{I_{out}}{I_{in}} = \frac{1}{1 + \left( \frac{2F}{\pi} \right)^2 \sin^2 \left( \frac{\phi_q}{2} \right)} \quad (\text{II.26})$$

here  $\phi_q (=2qd/\lambda)$  is the round trip phase shift. A constructive interference occurs if the transmitted beams are in phase, and this corresponds to the resonance frequencies of the resonator. When the laser wavelength is scanned then transmission spectrum would consist of series of peaks separated by longitudinal mode separation, also known as free spectral range (FSR) of the cavity as shown in Figure II.2.

The quantity F is finesse of cavity and is given as:

$$F = \frac{\pi\sqrt{R_m}}{1 - R_m} = \frac{\text{FSR}}{\Delta\nu_{\text{cavity}}} \quad (\text{II.27})$$

where,  $\Delta\nu_{\text{cavity}}$  is FWHM of transmitted peak. The decay time of the photons trapped inside the cavity is calculated from the following equation:

$$\tau_{\text{RD}} = \frac{1}{2\pi\Delta\nu_{\text{cavity}}} = \frac{d}{c} \frac{\sqrt{R_m}}{1 - R_m} \quad (\text{II.28})$$

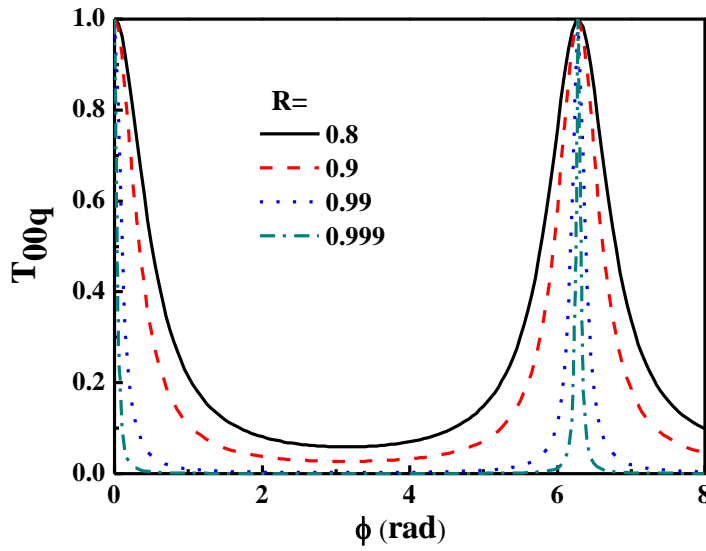


**Figure II.2** Transmission spectrum of optical cavity when a laser beam is coupled to its  $\text{TEM}_{00}$  mode.

For a non-ideal case, where mode matching to  $\text{TEM}_{00}$  mode is not perfect or when laser beam is coupled off-axis to the cavity, then higher order modes are also excited. The transmission spectrum would now contain resonance frequencies corresponding to all those modes that have been excited. The transmission spectrum for each mode is given as:

$$T_{plq} = \frac{\varepsilon_{plq}}{1 + \left(\frac{2F}{\pi}\right)^2 \sin^2\left(\frac{\phi_{plq}}{2}\right)} \quad (\text{II.29})$$

These spatial  $TEM_{plq}$  appears as a frequency comb with a small shift in the wavelength from the longitudinal mode  $TEM_{00q}$ . For a special condition, when ratio of ‘transverse mode spacing’ to ‘the longitudinal spacing’ is a rational number, cavity spectrum consists of a series of resonances spaced by  $FSR/N_r$ . This happens when the beam retraces its path after  $N_r$  round trips following an elliptical spot pattern. This condition is known as re-entrant condition. The re-entrant condition is satisfied for certain spacing between the mirrors. The separation  $d$  for re-entrant beam (as calculated under paraxial approximation) is given as:

$$d = \Re \left[ 1 - \cos\left(\frac{2\pi M_r}{N_r}\right) \right] \quad (\text{II.30})$$

where  $N_r$  is number of passes through the cell after which beam becomes re-entrant,  $M_r$  is number of rotations on each mirror after  $N_r$  trips and  $\Re$  is the radius of the curvature of the mirrors used [52]. The re-entrant condition depends only on the ratio of separation between the mirrors to their radius of curvature and is independent of entrance angle and co-ordinates of the incident beam.

### II.3 Coupling Laser Beam to an Optical Cavity

The coupling of external laser source to optical cavity requires both spatial and spectral mode matching as described below:

#### II.3.1 Spatial Mode Matching

Consider a beam with spatial distribution  $E_{inc}(x,y,z)$ , incident on an optical cavity with circular aperture. The coefficient corresponding to spatial mode  $TEM_{plq}$  is given by the overlap integral:

$$\epsilon_{lpq} = \frac{|\int E_{inc}(x,y,z)E_{lp}(x,y,z) dA|^2}{\int |E_{inc}|^2 dA \int |E_{lp}|^2 dA} \quad (II.23)$$

the spatial integration  $dA$ , is carried out over the cavity mode volume [137]. To effectively couple the laser power to the resonator, this overlap integral should have maximum value.  $\epsilon_{lpq}=1$  corresponds to the condition when all the incident power is coupled to  $TEM_{plq}$  mode of the resonator. This happens when spatial distribution of the incident beam is identical to the spatial mode distribution of the cavity. The process of transforming spatial distribution of incident beam to maximize coupling efficiency is called mode matching and is accomplished by use of optical elements.

To satisfy mode matching condition, the incident beam must adapt to the physical characteristics of cavity viz. its length and radii of curvature of mirrors. This implies that the radius of curvature of the incident beam wave front,  $\mathfrak{R}_z$ , must coincide with the curvature of the spherical mirror at the reflection. Let us consider a setup shown in Figure II.3. Then using ABCD matrix transformation the mode matching condition is derived from the following equation:

$$q_{zM2} = \begin{bmatrix} 1 & d \\ 0 & 1 \end{bmatrix} \begin{bmatrix} \frac{2}{2n} & 0 \\ -\frac{1}{\mathfrak{R}_1} & 1 \end{bmatrix} \begin{bmatrix} 1 & d1 \\ 0 & 1 \end{bmatrix} q_z' \quad (II.24)$$

$$q_z' = \begin{bmatrix} 1 & d2 \\ 0 & 1 \end{bmatrix} \begin{bmatrix} A & B \\ C & D \end{bmatrix}_{optics} \begin{bmatrix} 1 & d3 \\ 0 & 1 \end{bmatrix} q_{z0} \quad (II.25)$$

Here  $\begin{bmatrix} A & B \\ C & D \end{bmatrix}_{optics}$  represents ABCD matrix of the mode matching optics, which can either be a single lens or a telescopic combination of two lenses [138], and  $q_{z0}$  is a beam parameter of the beam emitted by the laser,  $\mathfrak{R}_1$  is radius of curvature of mirror M1 and  $n$  is its refractive index.

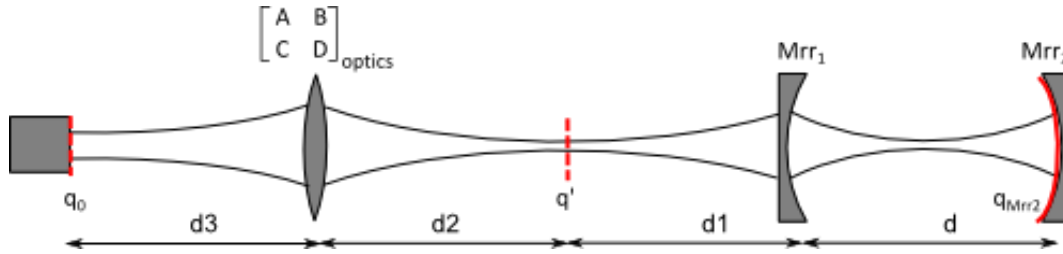


**Figure II.3** Optical setup for mode matching.

### II.3.2 Exciting Cavity Modes (Impedance Matching)

When a laser beam is coupled to a cavity, only the wavelengths resonating with the cavity modes will be coupled and transmitted, while all other wavelengths are reflected back. The total transmitted intensity through an optical cavity thus depends on spectral profile of incident light with respect to the spectral properties of the cavity. The spectrum of total transmitted intensity is a convolution of laser beam spectra with spectral profile of the cavity [139, 140].

When FSR of a cavity is greater than the laser linewidth, then for effective coupling of laser power, its wavelength should be equal to the resonance frequency of the cavity. The process of matching two wavelengths is called impedance matching. This involves scanning either cavity length or laser wavelength and locking the laser wavelength to the cavity's peak transmission. However, when FSR of the cavity is much less than the laser linewidth, then cavity transmission is independent of the laser wavelength and cavity acts as a white cell. In an intermediate case, when FSR is of the order of laser linewidth then cavity transmission shows fluctuations about the mean transmitted power, which appears as fringes in cavity transmission.

### APPENDIX III: LEAST SQUARE CURVE FITTING

Least square curve fitting is a process of finding a best fitting analytical expression  $y=f(x,a)$  to a set of data points  $(x_i,y_i)$  while minimizing the sum of squares of the offsets (residual) of data points from the theoretical curve [141]. The residual for set of  $n$  data points is mathematically expressed as:

$$R^2 = \sum_{i=1}^n r_i^2 = \sum_{i=1}^n (y_i - f(x_i, a))^2 \quad (\text{III.1})$$

where  $a$  represents set of  $m$  fitting parameters  $(a_1, a_2, a_3, \dots, a_m)$ . The minimum residual is found by setting the partial derivative to zero:

$$\frac{\partial(R^2)}{\partial a_j} = 0, \quad \forall j = 1, \dots, m. \quad (\text{III.2})$$

The problem of least square fitting thus boils down finding the minima of the residual function.

#### III.1 Linear Least Square Fitting

In case when the fitting function  $f$  is a polynomial order  $m-1$ , the least square fitting falls under the category of linear least square curve fitting. Here the equation (III.2) results in a set of linear equations, which can be represent by following matrix:

$$\begin{bmatrix} n & \sum_{i=1}^n x_i & \dots & \sum_{i=1}^n x_i^m \\ \sum_{i=1}^n x_i & \sum_{i=1}^n x_i^2 & \dots & \sum_{i=1}^n x_i^{m+1} \\ \vdots & \vdots & \ddots & \vdots \\ \sum_{i=1}^n x_i^m & \sum_{i=1}^n x_i^{m+1} & \dots & \sum_{i=1}^n x_i^{2m} \end{bmatrix} \begin{bmatrix} a_0 \\ a_1 \\ \vdots \\ a_k \end{bmatrix} = \begin{bmatrix} \sum_{i=1}^n y_i \\ \sum_{i=1}^n x_i y_i \\ \vdots \\ \sum_{i=1}^n x_i^m y_i \end{bmatrix} \quad (\text{III.3})$$

The solution of this matrix gives best fitting polynomial to the set of data points.

## III.2 Non-Linear Least Square Fitting

For any general function, for which the derivatives of  $R^2$  is not a linear functions of the fitting parameters  $a_j$  and the equation (III.2) does not have a closed solution. These functions come under the category of nonlinear least square curve fitting. In the non-linear least square fitting methods, the initial values of the parameters must be chosen. Then the parameters are optimized using an iterative process. In many cases the starting value of parameters must close enough to required solution else the software may converge to local minima rather than global minimum which results in the optimum solution.

### III.2.1 Derivative Methods

There are few algorithms based on updating the parameters ( $a_j$ ) in incremental steps ( $\delta_j$ ) toward the global minima:

$$a_{j,k+1} = a_{j,k} + \delta_j \quad (\text{III.4})$$

The most commonly used algorithms are: Gradient Descent (GD) method, Gauss-Newton (GN) method and Levenberg–Marquardt algorithm (LMA). These algorithms differ from each other by the method of calculating the value of  $\delta$ . The  $\delta$  values are calculated from the Jacobian matrix defined as:

$$J_{ij} = \frac{\partial f(x_i, a)}{\partial a_j} \quad (\text{III.5})$$

The expression for calculating the incremental step for parameters optimization for few well known methods is given in Table III.1. In the GD method the parameters are updated in steepest descent direction. The parameters quickly approach the solution from a distance, however the

convergence becomes very slow close to the solution. In the GN method the residual is minimised by assuming that the residual function is locally quadratic, and then finding the minimum of the quadratic. The Levenberg–Marquardt algorithm is the combination of GD and GN methods. The behaviour of LMA is similar to GD method when the parameters are far from the optimum value, and it behaves like the GN method when the parameters are close to the optimum value. All the above methods require calculation of gradient which is computationally expensive.

Table III.1 The incremental step for parameters optimization in the least square fitting algorithm.

Method Name	Calculation of Incremental Step, $\delta$
Gradient Descent Method (GD)	$-J^T r$
Gauss Newton's Method (GN)	$-(J^T J)^{-1} J^T r$
Levenberg–Marquardt Algorithm (LMA)	$-(J^T J + \lambda I)^{-1} J^T r$ ( $\lambda$ is Marquardt parameter which is adjusted after each iteration.)

### III.2.2 Heuristic Methods

The heuristic methods are based on direct search of the optimum solution, without evaluating the gradient functions. The search is based on evaluation of a verity of parameters . Although the heuristic algorithms are not guaranteed to always work but often work well in practice. The Neldar-Mead algorithm is one such search method which is often used [142]. In this method a simplex (m dimensional Polyhedrons, for m parameters) with m+1 vertices is created, while each vertex corresponding to particular set parameters in the function. In every iteration, the parameters of the vertex with highest objective function are adjusted such that the highest vertex always decreases.

In this method the residuals initially decrease rapidly. Although the convergence is slow near the optimum solution.

### III.3 Software for Acquiring and Processing Data

A user-friendly software was written to acquire and process the data. The least square fitting algorithm based on Nelder-Mead search method was used to analyse the acquired spectrum. A brief outline of the program used is as follows.

- a) Initialize the instruments: Digital storage oscilloscope, pressure sensor, temperature sensor.
- b) Acquire the signals: Cavity transmission, laser intensity, laser scanning voltage in averaging mode from oscilloscope and value of pressure and temperature from respective sensors.
- c) Evaluate the single pass absorption spectrum from the acquired signals (using equations 4.7 and 5.3).
- d) Calculate the pressure and Doppler broadened peak width ( $\Gamma_L$  and  $\Gamma_G$ ) from acquired pressure and temperature values, for all the peak using parameters from HITRAN database. Since  $\Gamma_L$  depends on fractional humidity ( $H_2O$ ) content of the sample (an unknown quantity), the  $\Gamma_L$  values are evaluated using fractions obtained from previous fit results. This method is valid since sudden change in humidity level is unlikely.
- e) Call least square fitting algorithm based on Nelder-Mead search method to find fitting parameter. These parameters are shift in peak positions (shift) and additional Gaussian broadening parameter ( $\Delta$ ). The parameter shift takes care of wavelength shifts of the diode laser and the parameter  $\Delta$  accounts for other broadening mechanisms mainly due to

instrumental broadening. A sub routine evaluates  $R^2$  function (function to be minimised) in following manner:

- a. Evaluate the normalized Voigt peak shapes for each peak using the width ( $\Gamma_G$ ,  $\Gamma_L$ , and  $\Delta$ ) and position parameters (Peak position from HITRAN database + shift).
- b. Calculate the height of each peak such that linear combination of peak profiles scaled by height gives the approximate fitting function. Evaluate the  $R^2$  value.
- f) Calculate the spectrum and profile of each peak after convergence from the optimized spectrum parameters that are heights and widths of all peaks.
- g) Evaluate the area under each fitted peak and calculate concentrations using peak parameters from HITRAN database.
- h) Display the fitted spectrum and time series plot of [HDO] with and without averaging.
- i) Go back to step (ii) and repeat the process till user exits the program.

## APPENDIX IV: SPECTROSCOPIC DATA

**IV.1 Spectroscopic Peak Parameters from HITRAN Database for the Peaks Considered in Fitting Algorithm [43, 44].**

Isotopologue	Transition Wave Number (cm <sup>-1</sup> )	Line Intensity, Multiplied by Isotopologue Abundance, at T = 296 K	Einstein A-Coefficient in s <sup>-1</sup>	Air-Broadened Lorentzian HWHM at P = 1 atm and T = 296 K	Self-Broadened HWHM at 1 atm Pressure and 296 K	Lower-State Energy	Temperature Exponent for the Air-Broadened HWHM	Pressure Shift Induced by Air, Referred to P=1 atm	Vibrational Quantum Numbers (Upper State) ← (Lower State) of a Transition	Rotational Quantum Numbers for the (Upper State) ← (Lower State)
H <sub>2</sub> <sup>16</sup> O	7190.7388	3.94E-22	1.140	0.0960	0.529	275.497	0.69	-0.00678	(101)←(000)	4 <sub>14</sub> ←4 <sub>13</sub>
H <sub>2</sub> <sup>16</sup> O	7190.7473	4.43E-26	0.032	0.0660	0.281	1813.223	0.47	-0.00608	(200)←(000)	10 <sub>65</sub> ←11 <sub>38</sub>
H <sub>2</sub> <sup>16</sup> O	7190.7809	3.15E-24	10.890	0.0776	0.346	1907.616	0.71	-0.01186	(111)←(010)	3 <sub>31</sub> ←3 <sub>30</sub>
H <sub>2</sub> <sup>16</sup> O	7190.8999	3.75E-26	0.058	0.0972	0.456	1742.306	0.72	-0.00916	(210)←(010)	3 <sub>12</sub> ←2 <sub>21</sub>
HDO	7190.9444	1.53E-26	0.386	0.0835	0.333	653.089	0.57	-0.00882	(002)←(000)	8 <sub>27</sub> ←8 <sub>26</sub>
H <sub>2</sub> <sup>17</sup> O	7190.9774	4.11E-25	1.990	0.0860	0.467	445.794	0.70	-0.00696	(101)←(000)	5 <sub>24</sub> ←5 <sub>23</sub>
HDO	<b>7191.0392</b>	<b>6.90E-25</b>	<b>3.785</b>	<b>0.0920</b>	<b>0.412</b>	<b>156.382</b>	<b>0.69</b>	<b>-0.01136</b>	<b>(002)←(000)</b>	<b>3<sub>13</sub>←4<sub>14</sub></b>
H <sub>2</sub> <sup>16</sup> O	<b>7191.1568</b>	<b>1.48E-24</b>	<b>15.340</b>	<b>0.0758</b>	<b>0.307</b>	<b>1907.450</b>	<b>0.71</b>	<b>-0.01080</b>	<b>(111)←(010)</b>	<b>3<sub>30</sub>←3<sub>31</sub></b>
H <sub>2</sub> <sup>16</sup> O	7191.2320	7.35E-26	0.027	0.0682	0.281	1690.664	0.47	0.00640	(120)←(000)	11 <sub>56</sub> ←11 <sub>29</sub>
H <sub>2</sub> <sup>18</sup> O	7191.3550	2.42E-25	4.862	0.0754	0.385	921.896	0.61	-0.00760	(101)←(000)	7 <sub>43</sub> ←7 <sub>44</sub>
H <sub>2</sub> <sup>18</sup> O	7191.4523	6.86E-26	0.442	0.0911	0.445	658.610	0.63	-0.01266	(002)←(000)	6 <sub>06</sub> ←6 <sub>33</sub>
H <sub>2</sub> <sup>16</sup> O	7191.5574	6.37E-25	3.269	0.0998	1693.65	0.72	0.4600	-0.00912	(111)←(010)	2 <sub>12</sub> ←2 <sub>11</sub>

#### IV.2 Spectroscopic Peak Parameters from GEISA-2015 Database for the Peaks Considered in Fitting Algorithm [46].

Isotopologue	Wavenumber (cm <sup>-1</sup> )	Intensity (cm <sup>-1</sup> / Molec.cm <sup>-2</sup> at 296 K)	Air Broadening Pressure Halfwidth (cm <sup>-1</sup> atm <sup>-1</sup> at 296 K)	Energy of the Lower Level of the Transition (cm <sup>-1</sup> )	Coefficient for Temperature Dependence Of Halfwidth	Self Broadening Pressure Halfwidth (cm <sup>-1</sup> ctm <sup>-1</sup> at 296 K)	Air Pressure Shift of the Peak Transition (cm <sup>-1</sup> atm <sup>-1</sup> At 296 K)	Vibrational Transition	Rotational Transition
H <sub>2</sub> <sup>16</sup> O	7190.7387	3.941E-22	0.0960	275.4971	0.69	0.5290	-0.00678	(101)←(000)	4 <sub>14</sub> ←4 <sub>13</sub>
H <sub>2</sub> <sup>16</sup> O	7190.7464	4.625E-26	0.0660	1813.224	0.47	0.2811	-0.00608	(200)←(000)	10 <sub>65</sub> ←11 <sub>38</sub>
H <sub>2</sub> <sup>16</sup> O	7190.7808	4.639E-24	0.0776	1907.616	0.71	0.3460	-0.01186	(111)←(010)	3 <sub>31</sub> ←3 <sub>30</sub>
H <sub>2</sub> <sup>16</sup> O	7190.8989	3.745E-26	0.0972	1742.306	0.72	0.4563	-0.00916	(210)←(010)	3 <sub>12</sub> ←2 <sub>21</sub>
HDO	7190.9443	1.847E-26	0.0835	653.0887	0.57	0.3330	0	(002)←(000)	8 <sub>27</sub> ←8 <sub>26</sub>
H <sub>2</sub> <sup>17</sup> O	7190.9771	4.275E-25	0.0860	445.7934	0.7	0.4670	-0.00696	(101)←(000)	5 <sub>24</sub> ←5 <sub>23</sub>
<b>HDO</b>	<b>7191.0396</b>	<b>8.145E-25</b>	<b>0.0920</b>	<b>156.3823</b>	<b>0.69</b>	<b>0.4122</b>	<b>0</b>	<b>(002)←(000)</b>	<b>3<sub>13</sub>←4<sub>14</sub></b>
H <sub>2</sub> <sup>16</sup> O	<b>7191.1562</b>	<b>1.517E-24</b>	<b>0.0758</b>	<b>1907.452</b>	<b>0.71</b>	<b>0.3070</b>	<b>-0.0108</b>	<b>(111)←(010)</b>	<b>3<sub>30</sub>←3<sub>31</sub></b>
H <sub>2</sub> <sup>16</sup> O	7191.2319	7.35E-26	0.0682	1690.664	0.47	0.2811	0.00640	(120)←(000)	11 <sub>56</sub> ←11 <sub>29</sub>
H <sub>2</sub> <sup>18</sup> O	7191.3555	2.503E-25	0.0754	921.8957	0.61	0.3850	-0.0076	(101)←(000)	7 <sub>43</sub> ←7 <sub>44</sub>
H <sub>2</sub> <sup>18</sup> O	7191.4521	8.542E-26	0.0911	658.61	0.63	0.4450	-0.01266	(002)←(000)	6 <sub>06</sub> ←6 <sub>33</sub>
H <sub>2</sub> <sup>16</sup> O	7191.5566	6.679E-25	0.0998	1693.65	0.72	0.4600	-0.00912	(111)←(010)	2 <sub>12</sub> ←2 <sub>11</sub>

## References

- [1] W. M. Geiger and M. W. Raynor, *Trace analysis of specialty and electronic gases*: John Wiley & Sons, 2013.
- [2] X. Liu, S. Cheng, H. Liu, S. Hu, D. Zhang, and H. Ning, "A survey on gas sensing technology," *Sensors*, vol. 12, pp. 9635-9665, 2012.
- [3] N. Loftfield, H. Flessa, J. Augustin, and F. Beese, "Automated gas chromatographic system for rapid analysis of the atmospheric trace gases methane, carbon dioxide, and nitrous oxide," *Journal of Environmental Quality*, vol. 26, pp. 560-564, 1997.
- [4] Z. Muccio and G. P. Jackson, "Isotoperatio mass spectrometry," *Analyst*, vol. 134, pp. 213-222, 2009.
- [5] R. K. Boyd, C. Basic, and R. A. Bethem, *Trace quantitative analysis by mass spectrometry*: John Wiley & Sons, 2011.
- [6] S. S. Bajaj and A. R. Gore, "The Indian PHWR," *Nuclear Engineering and Design*, vol. 236, pp. 701-722, 2006.
- [7] T. Park and K. Aydogdu, "Effect of design improvements in heavy water management systems to reduce heavy water losses and tritium releases at Wolsong 2,3 and 4," International Atomic Energy Agency (IAEA) 1011-4289, 1994.
- [8] M. V. Ramana, D. S. Antonette, and K. N. R. Amulya, "Economics of nuclear power from heavy water reactors," *Economic and Political Weekly*, vol. 40, pp. 1763-1773, 2005.
- [9] AERB, *AERB Safety Guide- Radiation protection aspects in design for pressurised heavy water reactor based nuclear power plants*, 2005.
- [10] D. Delacroix, J. P. Guerre, P. Leblanc, and C. Hickman, *Radionuclide and radiation protection data handbook 2002*, 2nd ed.: Nuclear Technology Publishing, 2002.
- [11] NPCIL, "Status report 105 - Indian 700 MWe PHWR (IPHWR-700)," Nuclear Power Corporation of India Limited (NPCIL)2011.
- [12] A. I. Miller, J. Luxat, E. G. Price, and P. J. Fehrenbach, "Heavy water reactors," in *Nuclear Engineering Handbook, second edition*, ed: CRC Press, 2016, pp. 163-220.
- [13] T.-K. Park and S.-H. Jung, "Detection of gaseous heavy water leakage points in CANDU 6 pressurized heavy water reactors," *International Nuclear Information System* vol. 30, 1996.
- [14] B. B. Zhai, "Systems and methods for detecting a leaking fuel channel in a nuclear reactor," ed: Google Patents, 2017.
- [15] S. R. Mitra, S. D. Kohale, B. K. Parida, G. D. Gathe, C. K. Pati, B. K. Mudgal, *et al.*, *Enhancement of efficacy of process water monitors in detecting heavy water leak in steam generator blow down lines*. India: Prime Time Education, 2006.

- [16] B. N. Dileep, P. Sundar Rajan, K. B. Jashi, D. Veerendra, B. M. Sadasiv, L. Chand, *et al.*, "Counting of samples labeled with tritium using binary liquid scintillation solution," *Radiation Protection and Environment*, vol. 24, pp. 152-155, 2001.
- [17] R. F. Curl and F. K. Tittel, "Tunable infrared laser spectroscopy," *Annual Reports on the Progress of Chemistry C*, vol. 98, pp. 219-272, 2002.
- [18] E. Kerstel and L. Gainfrani, "Advances in laser-based isotope ratio measurements: selected applications," *Applied Physics B*, vol. 92, pp. 439-449, 2008.
- [19] M. W. Sigrist, R. Bartlome, D. Marinov, J. M. Rey, D. Vogler, and H. Wächter, "Trace gas monitoring with infrared laser-based detection schemes," *Applied Physics B*, vol. 90, pp. 289-300, 2008.
- [20] M. Lackner, "Tunable diode laser absorption spectroscopy (TDLAS) in the process industries—a review," *Reviews in Chemical Engineering*, vol. 23, pp. 65-147, 2007.
- [21] A. O'Keefe, J. J. Scherer, and J. B. Paul, "CW Integrated cavity output spectroscopy " *Chemical Physics Letters* vol. 307, pp. 343 - 349, 1999.
- [22] G. Gagliardi and H.-P. Loock, *Cavity-enhanced spectroscopy and sensing*: Springer, 2014.
- [23] L. Lee, H. Park, T.-S. Kim, M. Kim, and D.-Y. Jeong, "Development of a portable heavy-water leak sensor based on laser absorption spectroscopy," *Annals of Nuclear Energy*, vol. 87, pp. 350-355, 2016.
- [24] H. Park, T.-S. Kim, L. Lee, S.-U. Lee, K.-H. Ko, D.-Y. Jeong, *et al.*, "A laser leak detector for leakage monitoring of fuel channel closure plugs in pressurized heavy water reactors," *Nuclear Engineering and Design*, vol. 265, pp. 880-885, 2013.
- [25] E. Bakker and M. Telting-Diaz, "Electrochemical sensors," *Analytical Chemistry*, vol. 74, pp. 2781-2800, 2002.
- [26] H. Y. Aboul-Enein, R.-I. Stefan, J. F. van Staden, X. R. Zhang, A. M. Garcia-Campana, and W. R. G. Baeyens, "Recent developments and applications of chemiluminescence sensors," *Critical Reviews in Analytical Chemistry*, vol. 30, pp. 271-289, 2000.
- [27] T.-V. Dinh, I.-Y. Choi, Y.-S. Son, and J.-C. Kim, "A review on non-dispersive infrared gas sensors: Improvement of sensor detection limit and interference correction," *Sensors and Actuators B: Chemical*, vol. 231, pp. 529-538, 2016.
- [28] D. L. Andrews and A. A. Demidov, *An introduction to laser spectroscopy*: Springer Science & Business Media, 2012.
- [29] U. Platt and J. Stutz, *Differential optical absorption spectroscopy: Principles and applications*: Springer, 2008.
- [30] U. Wandinger, *Introduction to lidar*: Springer, 2005.
- [31] B. C. Smith, *Fundamentals of fourier transform infrared spectroscopy*, 2 ed.: CPC Press.
- [32] D. A. Cremers and A. K. Knight, *Laser induced breakdown spectroscopy*: Wiley Online Library, 2000.

- [33] D. W. Hahn and N. Omenetto, "Laser-induced breakdown spectroscopy (LIBS), part II: review of instrumental and methodological approaches to material analysis and applications to different fields," *Applied Spectroscopy*, vol. 66, pp. 347-419, 2012.
- [34] R. Allan, "Photoacoustic spectroscopy. New tool for investigation of solids," *Analytical Chemistry*, vol. 47, pp. 592A–604a, 1975.
- [35] W. Meier-Augenstein, "Applied gas chromatography coupled to isotope ratio mass spectrometry," *Journal of Chromatography A*, vol. 842, pp. 351-371, 1999.
- [36] J. Hodgkinson and R. P. Tatam, "Optical gas sensing: A review," *Measurement Science and Technology*, vol. 24, p. 012004, 2012.
- [37] G. Korotcenkov, *Chemical sensors: Comprehensive sensor technologies volume 5: Electrochemical and optical sensors* vol. 5: Momentum Press, 2011.
- [38] G. Herzberg, *Molecular spectra and molecular structure* vol. 1: Read Books Ltd, 2013.
- [39] R. Engelbrecht, "A compact NIR fiber-optic diode laser spectrometer for CO and CO<sub>2</sub>:: analysis of observed 2f wavelength modulation spectroscopy line shapes," *Spectrochimica Acta Part A: Molecular and Biomolecular Spectroscopy*, vol. 60, pp. 3291-3298, 2004/12/01/ 2004.
- [40] D. F. Swinehart, "The Beer-Lambert law," *Journal of Chemical Education*, vol. 39, 1962.
- [41] L. L. Grgdley, B. T. Marshall, and D. A. Chu, "LINEPAK: Algorithms for modeling spectral transmittance and radiance.," *Journal of Quantitative Spectroscopy and Radiative Transfer*, vol. 52, pp. 563-580, 1994.
- [42] E. E. Whiting, "An empirical approximation to the Voigt profile," *Journal of Quantitative Spectroscopy and Radiative Transfer*, vol. 8, pp. 1379-1384, 1968.
- [43] L. S. Rothman, I. E. Gordon, A. Barbe, D. C. Benner, P. F. Bernath, M. Birk, *et al.*, "The HITRAN 2008 molecular spectroscopic database," *Journal of Quantitative Spectroscopy and Radiative Transfer*, vol. 110, pp. 533-572, 2009.
- [44] *HITRAN Database*. Available: <http://www.hitran.org/docs/iso-meta/>
- [45] I. E. Gordon, L. S. Rothman, C. Hill, R. V. Kochanov, Y. Tan, P. F. Bernath, *et al.*, "The HITRAN2016 molecular spectroscopic database," *Journal of Quantitative Spectroscopy and Radiative Transfer*, vol. 203, pp. 3-69, 2017.
- [46] N. Jacquinet-Husson, R. Armante, N. A. Scott, A. Chédin, L. Crépeau, C. Boutammine, *et al.*, "The 2015 edition of the GEISA spectroscopic database," *Journal of Molecular Spectroscopy*, vol. 327, pp. 31-72, 2016.
- [47] *GEISA Database*. Available: <http://ara.lmd.polytechnique.fr>
- [48] E. J. Moyer, D. S. Sayres, G. S. Engel, J. M. S. Clair, F. N. Keutsch, N. T. Allen, *et al.*, "Design considerations in high-sensitivity off-axis integrated cavity output spectroscopy," *Applied Physics B*, vol. 92, pp. 467-474, 2008.

- [49] P. Werle, R. Miicke, and F. Slemr, "The limits of signal averaging in atmospheric trace-gas monitoring by tunable diode-laser absorption spectroscopy (TDLAS)," *Applied Physics B*, vol. 57, pp. 131-139, 1993.
- [50] J. Altmann, R. Baumgart, and C. Weitkamp, "Two-mirror multipass absorption cell," *Applied Optics* vol. 20, pp. 995-999, 1981.
- [51] G. S. Engel and E. J. Moyer, "Precise multipass Herriott cell design: Derivation of controlling design equations," *Optics Letters*, vol. 32, pp. 704-706, Mar 2007.
- [52] D. Herriott, H. Kogelnik, and R. Kompfner, "Off-axis paths in spherical mirror interferometers," *Applied Optics*, vol. 3, pp. 523-526, 1964.
- [53] I. Ramsay and J. Degnan, "A ray analysis of optical resonators formed by two spherical mirrors," *Applied Optics*, vol. 9, pp. 385-398, 1970.
- [54] J. G. Xin, A. Duncan, and D. R. Hall, "Analysis of hyperboloidal ray envelopes in Herriott cells and their use in laser resonators," *Applied Optics*, vol. 28, pp. 4576-4584, Nov 1989.
- [55] D. R. Herriott and H. J. Schulte, "Folded optical delay lines," *Applied Optics*, vol. 4, pp. 883-889, 1965.
- [56] P. L. Kebabian, "Off-axis cavity absorption cell," 1994.
- [57] J. B. McManus, P. L. Kebabian, and M. Zahniser, "Astigmatic mirror multipass absorption cells for long-path-length spectroscopy," *Applied Optics*, vol. 34, pp. 3336-3348, 1995.
- [58] D. Das and A. C. Wilson, "Very long optical path-length from a compact multi-pass cell," *Applied Physics B*, vol. 103, pp. 749-754, 2011.
- [59] L.-y. Hao, S. Qiang, G.-r. Wu, L. Qi, D. Feng, Q.-s. Zhu, *et al.*, "Cylindrical mirror multipass Lissajous system for laser photoacoustic spectroscopy," *Review of Scientific Instruments*, vol. 73, pp. 2079-2085, 2002.
- [60] J. A. Silver, "Simple dense-pattern optical multipass cells," *Applied Optics*, vol. 44, pp. 6545-6556, 2005.
- [61] W. Demtröder, *Laser spectroscopy: Basic concepts and instrumentation*: Springer Science & Business Media, 2013.
- [62] D. S. Bomse, A. C. Stanton, and J. A. Silver, "Frequency modulation and wavelength modulation spectroscopies: comparison of experimental methods using a lead-salt diode laser," *Applied Optics*, vol. 31, pp. 718-731, 20 February 1992 1992.
- [63] V. M. Baev, T. Latz, and P. E. Toschek, "Laser intracavity absorption spectroscopy," *Applied Physics B*, vol. 69, pp. 171-202, 1999.
- [64] G. Berden, R. Peeters, and G. Meijer, "Cavity ring-down spectroscopy: Experimental schemes and applications," *International Reviews in Physical Chemistry*, vol. 19, pp. 565-607, 2000.
- [65] D. Romanini, A. Kachanov, N. Sadeghi, and F. Stoeckel, "CW cavity ring down spectroscopy," *Chemical Physics Letters*, vol. 264, pp. 316-322, 1997.

- [66] A. O'Keefe, "Integrated cavity output analysis of ultra-weak absorption," *Chemical Physics Letters* vol. 293, pp. 331-336, 4 September 1998 1998.
- [67] A. O'Keefe and D. A. Deacon, "Cavity ring-down optical spectrometer for absorption measurements using pulsed laser sources," *Review of Scientific Instruments*, vol. 59, pp. 2544-2551, 1988.
- [68] D. Z. Anderson, J. C. Frisch, and C. S. Masser, "Mirror reflectometer based on optical cavity decay time," *Applied Optics*, vol. 23, p. 1238, 1984.
- [69] P. L. Kebabian, S. C. Herndon, and A. Freedman, "Detection of nitrogen dioxide by cavity attenuated phase shift spectroscopy," *Analytical Chemistry*, vol. 77, pp. 724-728, 2005.
- [70] R. Engeln, G. Berden, R. Peeters, and G. Meijer, "Cavity enhanced absorption and cavity enhanced magnetic rotation spectroscopy," *Review of Scientific Instruments*, vol. 69, pp. 3763-3769, 1998.
- [71] J. B. Paul, L. Lapson, and J. G. Anderson, "Ultrasensitive absorption spectroscopy with a high-finesse optical cavity and off-axis alignment," *Applied Optics*, vol. 40, pp. 4904-4910, 2001.
- [72] V. L. Kasyutich, C. E. Canosa-Mas, C. Pfrang, S. Vaughan, and R. P. Wayne, "Off-axis continuous-wave cavity-enhanced absorption spectroscopy of narrow-band and broadband absorbers using red diode lasers," *Applied Physics B*, vol. 77, pp. 755-761, 2002.
- [73] G. S. Engel, W. S. Drisdell, F. N. Keutsch, E. J. Moyer, and J. G. Anderson, "Ultrasensitive near-infrared integrated cavity output spectroscopy technique for detection of CO at 1.57  $\mu\text{m}$ : new sensitivity limits for absorption measurements in passive optical cavities," *Applied Optics*, vol. 45, pp. 9221-9229, 2006.
- [74] T. G. Spence, C. C. Harb, B. A. Paldus, R. N. Zare, B. Willke, and R. L. Byer, "A laser-locked cavity ring-down spectrometer employing an analog detection scheme," *Review of Scientific Instruments*, vol. 71, pp. 347-353, 2000.
- [75] O. Axner, P. Ehlers, A. Foltynowicz, I. Silander, and J. Wang, "NICE-OHMS —frequency modulation cavity-enhanced spectroscopy—principles and performance," in *Cavity-Enhanced Spectroscopy and Sensing*, ed: Springer, 2014, pp. 211-251.
- [76] V. L. Kasyutich, P. A. Martin, and R. J. Holdsworth, "Phase-shift off-axis cavity-enhanced absorption detector of nitrogen dioxide," *Measurement Science and Technology*, vol. 17, p. 923, 2006.
- [77] V. Motto-Ros, M. Durand, and J. Morville, "Extensive characterization of the optical feedback cavity enhanced absorption spectroscopy (OF-CEAS) technique: ringdown-time calibration of the absorption scale," *Applied Physics B*, vol. 91, pp. 203-211, 2008.
- [78] A. Zybin, Y. A. Kuritsyn, V. R. Mironenko, and K. Niemax, "Cavity enhanced wavelength modulation spectrometry for application in chemical analysis," *Applied Physics B*, vol. 78, pp. 103-109, 2004.

- [79] S. M. Ball, J. M. Langridge, and R. L. Jones, "Broadband cavity enhanced absorption spectroscopy using light emitting diodes," *Chemical Physics Letters*, vol. 398, pp. 68-74, 2004.
- [80] M. Levenson, B. Paldus, T. Spence, C. Harb, J. Harris Jr, and R. Zare, "Optical heterodyne detection in cavity ring-down spectroscopy," *Chemical Physics Letters*, vol. 290, pp. 335-340, 1998.
- [81] C. S. Edwards, G. P. Barwood, S. A. Bell, P. Gill, and M. Stevens, "A tunable diode laser absorption spectrometer for moisture measurements in the low parts in 10<sup>9</sup> range," *Measurement Science and Technology*, vol. 12, p. 1214, 2001.
- [82] D. C. Hovde, J. T. Hodges, G. E. Scace, and J. A. Silver, "Wavelength-modulation laser hygrometer for ultrasensitive detection of water vapor in semiconductor gases," *Applied Optics*, vol. 40, pp. 829-839, 2001.
- [83] G. Durry, A. Hauchecorne, J. Ovarlez, H. Ovarlez, I. Pouchet, V. Zeninari, *et al.*, "In situ measurement of H<sub>2</sub>O and CH<sub>4</sub> with telecommunication laser diodes in the lower stratosphere: Dehydration and indication of a tropical air intrusion at mid-latitudes," *Journal of Atmospheric Chemistry*, vol. 43, pp. 175-194, November 01 2002.
- [84] P. L. Kebabian, C. E. Kolb, and A. Freedman, "Spectroscopic water vapor sensor for rapid response measurements of humidity in the troposphere," *Journal of Geophysical Research: Atmospheres*, vol. 107, pp. AAC 2-1-AAC 2-14, 2002.
- [85] E. R. T. Kerstel, R. Q. Iannone, M. Chenevier, S. Kassi, H. J. Jost, and D. Romanini, "A water isotope spectrometer based on optical feedback cavity-enhanced absorption for in situ airborne applications," *Applied Physics B*, vol. 85, pp. 397-406, 2006.
- [86] J. M. Langridge, S. M. Ball, A. J. L. Shillings, and R. L. Jones, "A broadband absorption spectrometer using light emitting diodes for ultrasensitive, in situ trace gas detection," *Review of Scientific Instruments*, vol. 79, p. 123110, 2008.
- [87] E. R. Crosson, "A cavity ring-down analyzer for measuring atmospheric levels of methane, carbon dioxide, and water vapor," *Applied Physics B*, vol. 92, pp. 403-408, 2008.
- [88] W. J. Smith, *Modern optical engineering*: Tata McGraw-Hill Education, 2008.
- [89] F. Etayo, L. Gonzalez-Vega, and N. del Rio, "A new approach to characterizing the relative position of two ellipses depending on one parameter " *Computer Aided Geometric Design* vol. 23, pp. 324 - 350, 2006.
- [90] G. B. Hughes and M. Chraibi, "Calculating ellipse overlap areas," *Computing and Visualization in Science*, vol. 15, pp. 291-301, 2012.
- [91] G. P. Miller and C. B. Winstead, "Cavity ringdown laser absorption spectroscopy," in *Encyclopedia of Analytical Chemistry*, 2006.
- [92] "Light absorption by water molecules and inorganic substances dissolved in sea water," in *Light Absorption in Sea Water*, ed New York, NY: Springer New York, 2007, pp. 11-81.

- [93] P. R. Bunker and P. Jensen, *Molecular symmetry and spectroscopy*, 2nd Ed: NRC Research Press, 2006.
- [94] C. N. Banwell and E. M. McCash, *Fundamentals of molecular spectroscopy* vol. 851: McGraw-Hill New York, 1994.
- [95] G. Aruldas, *Molecular structure and spectroscopy*: PHI Learning Pvt. Ltd., 2007.
- [96] *Gas cell simulator*. Available: <http://www.spectralcalc.com/info/about.php>
- [97] C. E. Wieman and L. Hollberg, "Using diode lasers for atomic physics," *Review of Scientific Instruments*, vol. 62, pp. 1-20, 1991.
- [98] V. L. Kasyutich, C. S. E. Bale, C. E. Canosa-Mas, C. Pfrang, S. Vaughan, and R. P. Wayne, "Cavity-enhanced absorption: Detection of nitrogen dioxide and iodine monoxide using a violet laser diode," *Applied Physics B*, vol. 76, pp. 691–697, 2003.
- [99] R. Daniele, I. Ventrillard, G. Méjean, J. Morville, and E. Kerstel, "Introduction to cavity enhanced absorption spectroscopy," in *Cavity Enhanced Spectroscopy and Sensing*, G. Gagliardi and H.-P. Loock, Eds., ed London, UK: Springer, 2014.
- [100] G. Hancock and V. L. Kasyutich, "UV cavity enhanced absorption spectroscopy of the hydroxyl radical," *Applied Physics B*, vol. 79, pp. 383-388, 2004.
- [101] P. Maddaloni, G. Gagliardi, P. Malara, and P. D. Natale, "Off-axis integrated-cavity-output spectroscopy for trace-gas concentration measurements: Modeling and performance," *Journal of the Optical Society of America B*, vol. 23, pp. 1938 - 1945, September 2006.
- [102] L. Gianfrani, "Cavity-enhanced absorption spectroscopy of molecular oxygen," *Journal of the Optical Society of America B*, vol. 16, pp. 2247-2253, 1999.
- [103] S. Welzel, G. Lombardi, P. B. Davies, R. Engeln, D. C. Schram, and J. Röpcke, "Trace gas measurements using optically resonant cavities and quantum cascade lasers operating at room temperature," *Journal of Applied Physics*, vol. 104, p. 093115, 2008.
- [104] Y. A. Bakirkin, A. A. Kosterev, C. Roller, R. F. Curl, and F. K. Tittel, "Mid-infrared quantum cascade laser based off-axis integrated cavity output spectroscopy for biogenic nitric oxide detection," *Applied Optics*, vol. 43, pp. 2257-2266, 2004.
- [105] B. Ouyang and R. Jones, "Understanding the sensitivity of cavity-enhanced absorption spectroscopy: pathlength enhancement versus noise suppression," *Applied Physics B*, vol. 109, pp. 581-591, 2012.
- [106] S. E. Fiedler, A. Hese, and U. Heitmann, "Influence of the cavity parameters on the output intensity in incoherent broadband cavity-enhanced absorption spectroscopy," *Review of Scientific Instruments*, vol. 78, p. 073104, 2007.
- [107] V. L. Kasyutich and M. W. Sigrist, "Optimisation of laser linewidth and cavity alignment in off-axis cavity-enhanced absorption spectroscopy," *Infrared Physics & Technology*, vol. 71, pp. 179-186, 2015.

- [108] K. R. Parameswaran, D. I. Rosen, M. G. Allen, A. M. Ganz, and T. H. Risby, "Off-axis integrated cavity output spectroscopy with a mid-infrared interband cascade laser for real-time breath ethane measurements," *Applied Optics*, vol. 48, pp. B73-B79, 2009.
- [109] W. Chen, A. A. Kosterev, F. K. Tittel, X. Gao, and W. Zhao, "H<sub>2</sub>S trace concentration measurements using off-axis integrated cavity output spectroscopy in the near-infrared," *Applied Physics B*, vol. 90, pp. 311-315, 2008.
- [110] X. Lou, Y. Dong, D. Wu, J. Wei, and Z. Lu, "Integrated cavity output spectroscopy by using a sub-centimeter short optical cavity combined with a free-running Fabry–Perot diode laser," *Applied Physics B*, vol. 121, pp. 171-178, 2015.
- [111] R. Centeno, J. Mandon, S. M. Cristescu, and F. J. M. Harren, "Sensitivity enhancement in off-axis integrated cavity output spectroscopy," *Optics Express*, vol. 22, pp. 27985-27991, 2014.
- [112] C. Lengignon, X. Cui, W. Zhao, W. U. Tao, E. Fertein, and W. Chen, "RAM-free wavelength modulated off-axis integrated cavity output spectroscopy to OH radical monitoring," in *Propagation Through and Characterization of Distributed Volume Turbulence*, 2014, p. JTU4A. 36.
- [113] W. Chen, T. Wu, W. Zhao, G. Wysocki, X. Cui, C. Lengignon, *et al.*, "Atmospheric and environmental sensing by photonic absorption spectroscopy," in *SPIE OPTO*, 2013, pp. 86310Y-86310Y-11.
- [114] T. S. Kim, H. Park, K. Ko, G. Lim, Y. H. Cha, J. Han, *et al.*, "Laser-based sensor for a coolant leak detection in a nuclear reactor," *Applied Physics B*, vol. 100, pp. 437-442, 2010.
- [115] L. Lee, H. Park, T. S. Kim, K. H. Ko, and D. Y. Jeong, "A new sensor for detection of coolant leakage in nuclear power plants using off-axis integrated cavity output spectroscopy," *Nuclear Instruments and Methods in Physics Research Section A: Accelerators, Spectrometers, Detectors and Associated Equipment*, vol. 678, pp. 8-12, 2012.
- [116] M. Kakiuchi, "Distribution of isotopic water molecules, H<sub>2</sub>O, HDO, and D<sub>2</sub>O, in vapor and liquid phases in pure water and aqueous solution systems," *Geochimica et Cosmochimica Acta*, vol. 64, pp. 1485-1492, 2000.
- [117] R. R. Gamache, S. Kennedy, R. Hawkins, and L. S. Rothman, "Total internal partition sums for molecules in the terrestrial atmosphere," *Journal of Molecular Structure*, vol. 517-518, pp. 407-425, 29 March 1999 2000.
- [118] E. R. T. Kerstel, R. V. Trigt, N. Dam, J. Reuss, and H. A. J. Meijer, "Simultaneous determination of the <sup>2</sup>H/<sup>1</sup>H, <sup>17</sup>O/<sup>16</sup>O, and <sup>18</sup>O/<sup>16</sup>O isotope abundance ratios in water by means of laser spectrometry," *Analytical Chemistry*, vol. 71, pp. 5297-5303, 1999.
- [119] W. Zhao, X. Gao, W. Chen, W. Zhang, T. Huang, T. Wu, *et al.*, "Wavelength modulated off-axis integrated cavity output spectroscopy in the near infrared," *Applied Physics B*, vol. 86, pp. 353-359, 2007.

- [120] J. M. Supplee, E. A. Whittaker, and W. Lenth, "Theoretical description of frequency modulation and wavelength modulation spectroscopy," *Applied Optics*, vol. 33, pp. 6294-6302, 1994.
- [121] T. Zhang, J. Kang, D. Meng, H. Wang, Z. Mu, M. Zhou, *et al.*, "Mathematical methods and algorithms for improving near-infrared tunable diode-laser absorption spectroscopy," *Sensors*, vol. 18, 2018.
- [122] A. Hartmann, R. Strzoda, R. Schrobenauser, and R. Weigel, "Arithmetical elimination of superimposed interferencemodulation in laser spectroscopic gas concentration measurements," *Procedia Engineering*, vol. 47, pp. 1350-1353, 2012/01/01/ 2012.
- [123] H. C. Sun and E. A. Whittaker, "Novel étalon fringe rejection technique for laser absorption spectroscopy," *Applied Optics*, vol. 31, pp. 4998-5002, 1992/08/20 1992.
- [124] A. Savitzky and M. J. E. Golay, "Smoothing and differentiation of data by simplified least squares procedures," *Analytical Chemistry*, vol. 36, pp. 1627-1639, 1964/07/01 1964.
- [125] H. H. Madden, "Comments on the Savitzky-Golay convolution method for least-squares-fit smoothing and differentiation of digital data," *Analytical Chemistry*, vol. 50, pp. 1383-1386, 1978/08/01 1978.
- [126] J. Shin, "A method of locating leakage of heavy water in CANDU reactors using ratio of tritium to heavy water," presented at the ISOE Asian ALARA Symposium, Aomori, Japan, 2009.
- [127] F. Fernandoy, H. Meyer, H. Oerter, F. Wilhelms, W. Graf, and J. Schwander, "Temporal and spatial variation of stable-isotope ratios and accumulation rates in the hinterland of Neumayer station, East Antarctica," *Journal of Glaciology*, vol. 56, pp. 673-687, 2010.
- [128] M. Rathnakaran and A. Singh, "Tritium monitoring: present status," Bhabha Atomic Research Centre 1993.
- [129] M. Rathnakaran, R. M. Ravetkar, R. K. Samant, and M. C. Abani, "A real-time tritium-in-water monitor for measurement of heavy water leak to the secondary coolant," 2000.
- [130] R. A. Jalbert, "Monitoring tritium in air containing other radioactive gases," Los Alamos National Lab. 1982.
- [131] A. Manna, V. Madhavi, S. Sawant, P. Puneekar, M. Korgaonkar, N. Patel, *et al.*, "Oxygen-19 monitor for heavy water leak detection in Dhruva reactor," in *Proceedings of the International Conference on Radiological Safety in Workplace, Nuclear Facilities and Environment: Book of abstracts*, 2016.
- [132] D. S. Sayres, E. J. Moyer, T. F. Hanisco, J. M. S. Clair, F. N. Keutsch, A. O'Brien, *et al.*, "A new cavity based absorption instrument for detection of water isotopologues in the upper troposphere and lower stratosphere," *Review of Scientific Instruments*, vol. 80, p. 044102, 2009.
- [133] T. J. Griffis, "Tracing the flow of carbon dioxide and water vapor between the biosphere and atmosphere: A review of optical isotope techniques and their application," *Agricultural and Forest Meterology*, vol. 174-175, pp. 85-109, 2013.

- [134] H. Kogelnik and T. Li, "Laser beams and resonators," *Applied Optics*, vol. 5, pp. 1550-1567, 1966.
- [135] W. K. Dr., *Solid-state laser engineering* vol. 1: Springer New York, 2006.
- [136] G. F. Marshall and G. E. Stutz, *Handbook of optical and laser scanning*: CRC Press, 2004.
- [137] N. Uehara, E. K. Gustafson, M. M. Fejer, and R. L. Byer, "Modeling of efficient mode-matching and thermal-lensing effect on a laser-beam coupling into a mode-cleaner cavity," in *Photonics West'97*, 1997, pp. 57-68.
- [138] C. E. Webb and J. D. C. Jones, *Handbook of laser technology and applications: Laser design and laser systems* vol. 2: CRC Press, 2004.
- [139] J. Morville, D. Romanini, M. Chenevier, and A. Kachanov, "Effects of laser phase noise on the injection of a high-finesse cavity," *Applied Optics*, vol. 41, pp. 6980-6990, 2002.
- [140] A. P. Yalin, "Laser lineshape effects on cavity-enhanced absorption spectroscopy signals," *Applied Physics B*, vol. 78, pp. 477-483, 2004.
- [141] W. H. Press, S. A. Teukolsky, W. T. Vetterling, and B. P. Flannery, *Numerical recipes 3rd edition: The art of scientific computing*: Cambridge university press, 2007.
- [142] J. A. Nelder and R. Mead, "A simplex method for function minimization," *The Computer Journal*, vol. 7, pp. 308-313, 1965.